

DISS. ETH No. 17985

**CMS Pixel Module Qualification**  
**and**  
**Monte-Carlo Study of**  
 $H \rightarrow \tau^+ \tau^- \rightarrow \ell^+ \ell^- \cancel{E}_T$

A dissertation submitted to

ETH ZURICH

for the degree of

DOCTOR OF SCIENCES

presented by

PETER TRÜB

dipl. phys. ETH

born July 23, 1979

citizen of Zurich

accepted on the recommendation of

Prof. Dr. U. Langenegger

Prof. Dr. F. Pauss

2008



# Abstract

The first part of this work reports on the development of test and calibration algorithms for the qualification of the barrel modules of the CMS pixel detector. Several algorithms to test the hardware functionality and performance have been developed and implemented into an object-oriented software framework. Examples are the pixel readout test, the bump bonding test or the noise measurement. The qualification procedure also includes calibration routines. For instance the gain of each pixel or the temperature sensors of the readout chips have to be calibrated. Furthermore, an algorithm to unify the thresholds of all pixels was developed. According to specific quality criteria, each module is graded into one of three categories. Out of 981 tested modules, 806 were qualified for the usage in the detector.

The second part of this work deals with a Monte-Carlo study of the Higgs decay channel  $H \rightarrow \tau^+\tau^- \rightarrow \ell^+\ell^- \cancel{E}_T$  with a jet balancing the large transverse momentum of the Higgs boson. In contrast to many other studies, the analysis concentrates not on the vector boson fusion but on the gluon fusion production mechanism. The backgrounds are mainly suppressed by requiring a large invariant mass of the Higgs boson and the balancing jet. The discovery potential is limited by the resolution of the reconstructed missing transverse energy. To improve the resolution, a method to calibrate the missing transverse energy with the help of  $Z^0/\gamma^* \rightarrow \ell^+\ell^-$  events was developed. Combining all lepton channels, a signal significance of  $2.4\sigma$  significance is expected for a Higgs boson of 120 GeV mass and an integrated luminosity of  $30 \text{ fb}^{-1}$ .

## Zusammenfassung

Der erste Teil dieser Arbeit beschreibt die Test- und Kalibrationsalgorithmen, welche für die Qualifikation der Module des CMS Pixeldetektors entwickelt wurden. Mehrere Algorithmen zur Überprüfung der fehlerfreien Funktionsweise wurden erstellt und in einem objektorientierten Softwarepaket implementiert. So werden zum Beispiel die korrekte Auslese aller Pixel oder die elektrische Verbindung der Sensorpixel zum Auslesechip geprüft. Des weitern umfasst das Qualifizierungsverfahren der Module Kalibrationsalgorithmen, welche beispielsweise die Analogverstärkung jedes Pixels oder die Temperatursensoren auf allen Auslesechips eichen. Auf Grund der Testresultate wird jedes Detektormodul in eine von drei Qualitätskategorien eingeteilt. Von 981 getesteten Modulen wurden 806 für den Einbau in den Detektor freigegeben.

Der zweite Teil dieser Arbeit präsentiert eine Monte-Carlo Studie des Higgszerfalls  $H \rightarrow \tau^+\tau^- \rightarrow \ell^+\ell^- \cancel{E}_T$  mit einem Teilchenjet, welcher den hohen Transversalimpuls des Higgsteilchens ausgleicht. Im Gegensatz zu den meisten existierenden Studien konzentriert sich diese Analyse auf die Suche nach Higgs-Teilchen, welche durch Gluonfusion entstehen. Untergrundereignisse werden unterdrückt, indem eine grosse invariante Masse zwischen dem Higgs-Boson und dem ausgleichenden Jet verlangt wird. Das Potenzial für eine Entdeckung des Higgs-Teilchens wird vor allem durch die Messgenauigkeit der fehlenden transversalen Energie limitiert. Um die Messgenauigkeit zu verbessern, wurde eine Methode entwickelt, mit der die fehlende transversale Energie mit Hilfe von  $Z^0/\gamma^* \rightarrow \ell^+\ell^-$  Zerfällen kalibriert werden kann. Durch Kombination aller Leptonzerfallskanäle ergibt sich für ein Higgs-Teilchen der Masse 120 GeV und eine integrierte Luminosität von  $30 \text{ fb}^{-1}$  eine Signifikanz von  $2.4 \sigma$ .

# Contents

<b>1</b>	<b>Introduction</b>	<b>1</b>
<b>2</b>	<b>LHC and CMS</b>	<b>3</b>
2.1	The Large Hadron Collider . . . . .	3
2.2	The CMS Experiment . . . . .	4
2.2.1	The Solenoid . . . . .	6
2.2.2	The Silicon Tracker . . . . .	6
2.2.3	The Electromagnetic Calorimeter . . . . .	7
2.2.4	The Hadronic Calorimeter . . . . .	8
2.2.5	The Muon Chambers . . . . .	8
2.2.6	The Trigger System . . . . .	9
<b>3</b>	<b>The CMS Pixel Detector</b>	<b>12</b>
3.1	Introduction . . . . .	12
3.2	Detector Layout . . . . .	12
3.3	The Pixel Barrel Modules . . . . .	13
3.3.1	The Sensor . . . . .	16
3.3.2	The High Density Interconnect . . . . .	16
3.3.2.1	The Token Bit Manager . . . . .	17
3.3.2.2	The Analogue Readout . . . . .	17
3.3.3	The Readout Chip . . . . .	17
<b>4</b>	<b>Module Qualification</b>	<b>21</b>
4.1	Introduction . . . . .	21
4.1.1	The Test Setup . . . . .	22
4.1.2	The Software Framework . . . . .	22

4.1.3	Threshold Measurements . . . . .	24
4.2	Functionality Tests . . . . .	25
4.2.1	TBM Test . . . . .	25
4.2.2	Pixel Readout Test . . . . .	26
4.2.3	Address Decoding . . . . .	26
4.2.4	Trim Bits Test . . . . .	28
4.3	Performance Tests . . . . .	28
4.3.1	Noise Measurements . . . . .	28
4.3.2	Bump Bonding Test . . . . .	32
4.3.3	Sensor IV-curve . . . . .	35
4.4	Calibration Tests . . . . .	36
4.4.1	Trimming . . . . .	36
4.4.1.1	The Trim Algorithm . . . . .	36
4.4.1.2	Test Results . . . . .	39
4.4.1.3	Trimming for Very Low Thresholds . . . . .	40
4.4.1.4	Parametrised Trimming . . . . .	40
4.4.2	Pulse Height Calibration . . . . .	41
4.4.3	Temperature Calibration . . . . .	43
4.4.4	Vcal Calibration . . . . .	45
4.5	Summary . . . . .	50
<b>5</b>	<b>Higgs Physics</b>	<b>54</b>
5.1	The Higgs Mechanism . . . . .	54
5.2	Standard Model . . . . .	55
5.2.1	Properties of the Higgs Boson . . . . .	55
5.2.1.1	The Higgs Mass . . . . .	55
5.2.1.2	Production Mechanisms . . . . .	55
5.2.1.3	Decay Channels . . . . .	56
5.2.2	Higgs Search Strategies at the LHC . . . . .	57
5.3	Supersymmetry . . . . .	57
5.3.1	The Higgs Sector in the MSSM . . . . .	57
5.3.2	The Hierarchy Problem . . . . .	58
5.3.3	Properties of the Higgs Boson . . . . .	58

<b>6</b>	<b>Search for <math>H \rightarrow \tau^+\tau^- \rightarrow \ell^+\ell^- \cancel{E}_T</math></b>	<b>60</b>
6.1	Introduction . . . . .	60
6.2	Backgrounds . . . . .	60
6.3	Simulation . . . . .	61
6.4	Event Reconstruction . . . . .	62
6.4.1	Muons . . . . .	62
6.4.2	Electrons . . . . .	63
6.4.3	Jets . . . . .	64
6.4.4	b-Jets . . . . .	65
6.4.5	The Collinear Approximation . . . . .	66
6.4.6	Missing Transverse Energy . . . . .	68
6.5	Event Selection . . . . .	73
6.5.1	Online Selection . . . . .	73
6.5.2	Offline Selection . . . . .	73
6.5.2.1	Lepton Selection . . . . .	73
6.5.2.2	Preselection Cuts . . . . .	75
6.5.2.3	Mass Resolution Cuts . . . . .	77
6.5.2.4	Significance Cuts . . . . .	77
6.5.2.5	Cut Optimisation . . . . .	79
6.6	Fitting . . . . .	79
6.6.1	The Signal Distribution . . . . .	79
6.6.2	The $Z^0/\gamma^* \rightarrow \tau^+\tau^-$ Background . . . . .	80
6.6.2.1	Measuring the Invariant Mass Shape of $Z^0/\gamma^* \rightarrow \tau^+\tau^-$ from $Z^0/\gamma^* \rightarrow \ell^+\ell^-$ Data . . . . .	80
6.6.2.2	Fitting of the $Z^0/\gamma^* \rightarrow \tau^+\tau^-$ Background . . . . .	81
6.6.3	The $Z^0/\gamma^* \rightarrow \ell^+\ell^-$ Background . . . . .	82
6.6.4	The $t\bar{t}$ and $W^+W^-$ Backgrounds . . . . .	82
6.6.5	The Combined Fit . . . . .	85
6.7	Significance Estimation . . . . .	87
6.7.1	Event Counting . . . . .	87
6.7.2	Likelihood-Ratio Estimation . . . . .	87
6.8	Systematics . . . . .	89
6.9	Open Issues . . . . .	93

---

<b>7</b>	<b>Conclusions</b>	<b>94</b>
<b>A</b>	<b>Event Selection Figures</b>	<b>96</b>
A.1	Cut Variable Distributions . . . . .	97
A.2	Cut Optimisation . . . . .	100
	<b>Acronyms</b>	<b>104</b>
	<b>Bibliography</b>	<b>110</b>
	<b>Acknowledgement</b>	<b>111</b>
	<b>Curriculum Vitae</b>	<b>112</b>
	<b>Publications and Talks</b>	<b>113</b>



The fear of the LORD is the  
beginning of wisdom.

---

*Psalms 111, 10*

# Chapter 1

## Introduction

The current particle physics data is very well described by the Standard Model ([SM](#)) which interprets the  $Z^0$ ,  $W$ , and  $\gamma$  particles as the gauge bosons of the electroweak symmetry group  $SU(2)_L \otimes U(1)_Y$ . To accommodate for the large masses of the  $Z^0$  and  $W$  bosons and the vanishing mass of the photon, the electroweak symmetry has to be broken down to  $U(1)_{em}$ . Within the [SM](#) the symmetry is spontaneously broken by the non vanishing vacuum expectation value of the scalar Higgs field. The discovery of the quanta of this field, the Higgs particles, and the determination of their mass would be the ultimate success of the [SM](#).

Searches during the first phase of the Large Electron-Positron Collider ([LEP](#)) could place a lower bound on the Higgs mass of 78 GeV [[1](#)]. During the second phase, the searches were extended up to higher masses. Shortly before the shutdown in the year 2000, the ALEPH experiment reported an excess of events at a mass of 115 GeV [[2](#)], but the excess could not be confirmed by the other experiments. The [LEP](#) era ended with a combined upper limit of 114.4 GeV [[3](#)]. The next attempt to detect the Higgs boson was and is carried out at the Tevatron collider in Chicago. In summer 2008, Tevatron has excluded a [SM](#) Higgs particle at 170 GeV [[4](#)], while it has reached a sensitivity of about 3 times the [SM](#) prediction in the lower mass range of 120 GeV to 135 GeV.

With the completion of the Large Hadron Collider ([LHC](#)) this year, the search for the Higgs particle has lasted more than 28 years [[5](#)]. This proton-proton collider is supposed to have the capability to discover a [SM](#) Higgs boson with a mass up to 1 TeV. One of the two general purpose detectors at the [LHC](#) is the Compact Muon Solenoid ([CMS](#)). A large area silicon pixel detector with tenths of millions of channels

## 1. INTRODUCTION

---

will be used as a vertex detector. This detector, whose barrel part was designed and constructed at the Paul Scherrer Institute ([PSI](#)) was successfully delivered and integrated into [CMS](#) in July 2008. A first generation pixel detector was already used in the DELPHI experiment at [LEP](#). Together with the pixel detectors of the other [LHC](#) experiments, the [CMS](#) pixel detector will be the first application of a second generation pixel detector in a high energy collider experiment.

The outline of this work is as follows. Chapter [2](#) gives an overview of [LHC](#) and [CMS](#). Chapter [3](#) describes the aspects of the [CMS](#) pixel detector necessary to understand the pixel module tests described in Chapter [4](#). The second part of this work presents a Monte-Carlo study of the Higgs boson search in the channel  $H \rightarrow \tau^+\tau^- \rightarrow \ell^+\ell^-\cancel{E}_T$ . An introduction to the Higgs physics at the [LHC](#) is given in Chapter [5](#), the details of the analysis are discussed in Chapter [6](#). By default Planck units with  $\hbar = c = 1$  will be used throughout the work.

As for the earth, out of it  
cometh bread: and under it is  
turned up as it were fire.

---

*Job 28, 5*

## Chapter 2

# LHC and CMS

### 2.1 The Large Hadron Collider

Le Conseil Européen pour la Recherche Nucléaire ([CERN](#)) is currently building the [LHC](#) [6], a circular proton-proton collider with a circumference of about 27 km. Each proton beam has an energy of 7 Tera Electron Volts ([TeV](#)), which yields a centre of mass energy of 14 TeV. Since the proton is a composite particle, only a fraction of this energy is available for the hard interaction. Therefore, the [LHC](#) is considered to be able to discover particles with masses up to some TeV. The two main motivations to build the [LHC](#) are the searches for the Higgs boson and for new physics beyond the [SM](#). The production cross section for a light Higgs boson is of the order of 30 pb at the [LHC](#). To collect enough statistics for a discovery, an integrated luminosity of several inverse femtobarns is needed. With a planned instantaneous luminosity of  $2 \cdot 10^{33} \text{ cm}^{-2}\text{s}^{-1}$  during the first years (low luminosity) and an expected data taking time of about 50 days per year, on the order of  $10 \text{ fb}^{-1}$  will be delivered per year.

The physics at the [LHC](#) will be exploited by four big experiments, see Figure 2.1. Two of them are the general purpose detectors ATLAS (A Toroidal LHC Apparatus) [7] and [CMS](#) [8]. The third experiment, LHCb [9], is dedicated to b-physics and the fourth, ALICE (A Large Ion Collider Experiment) [10] to the study of heavy ion collisions. An additional experiment called TOTEM will measure the total  $pp$  cross section and study elastic scattering at small angles.

At the interaction points of the four experiments, the particle bunches collide with a frequency of 40 MHz, each bunch containing about  $1.15 \cdot 10^{11}$  particles. The large

number of particles per bunch increases the number of interesting events, but also poses the problem of multiple interactions. For the low (high) luminosity, there will be on average 5 (25) inelastic interactions per bunch crossing. This complicates the analysis since the particles of the investigated reaction have to be distinguished from the particles of the additional minimum bias events.

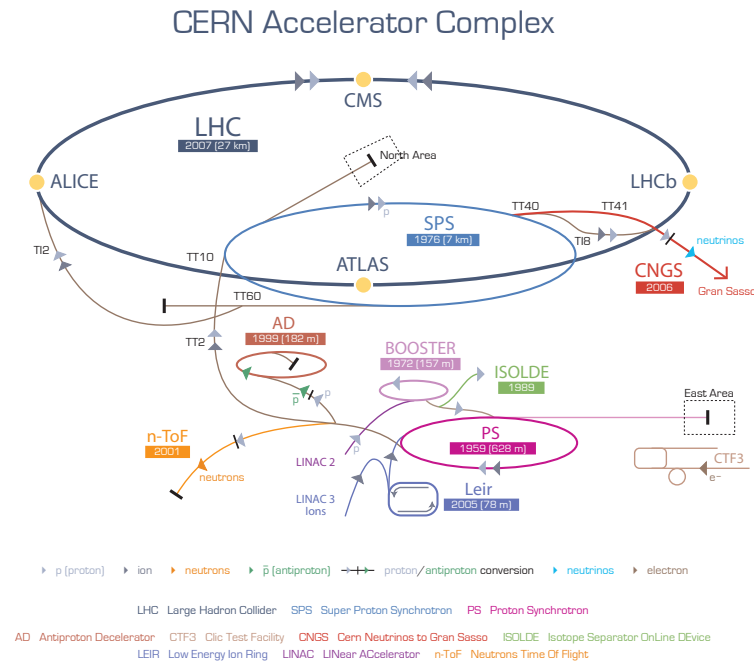


Figure 2.1: The CERN accelerator complex with the locations of the four main experiments ATLAS, CMS, LHCb and ALICE.

## 2.2 The CMS Experiment

CMS is one of the two general purpose experiments at the LHC and is located at Point 5 in Cessy (France). The main physics programs of the CMS experiment are the Higgs boson search and the quest for Supersymmetry. The strategy of the CMS experiment to address these tasks are reflected in the following detector requirements [11]:

1. Good muon identification and momentum resolution over a wide range of mo-

menta in the region  $|\eta| < 2.5$ , good dimuon mass resolution and the ability to determine unambiguously the charge of muons with  $p_T < 1$  TeV.

2. Good charged particle momentum resolution and reconstruction efficiency in the inner tracker. Efficient triggering and offline tagging of  $\tau$ 's and  $b$ -jets, requiring pixel detectors close to the interaction region.
3. Good electromagnetic energy resolution, good diphoton and dielectron mass resolution, wide geometric coverage, measurement of the direction of photons and localisation of the primary interaction vertex,  $\pi^0$  rejection and efficient photon and lepton isolation at high luminosities.
4. Good  $\cancel{E}_T$  (missing transverse energy) and dijet mass resolution, requiring a hadron calorimeter with a large hermetic geometric coverage and with fine lateral segmentation.

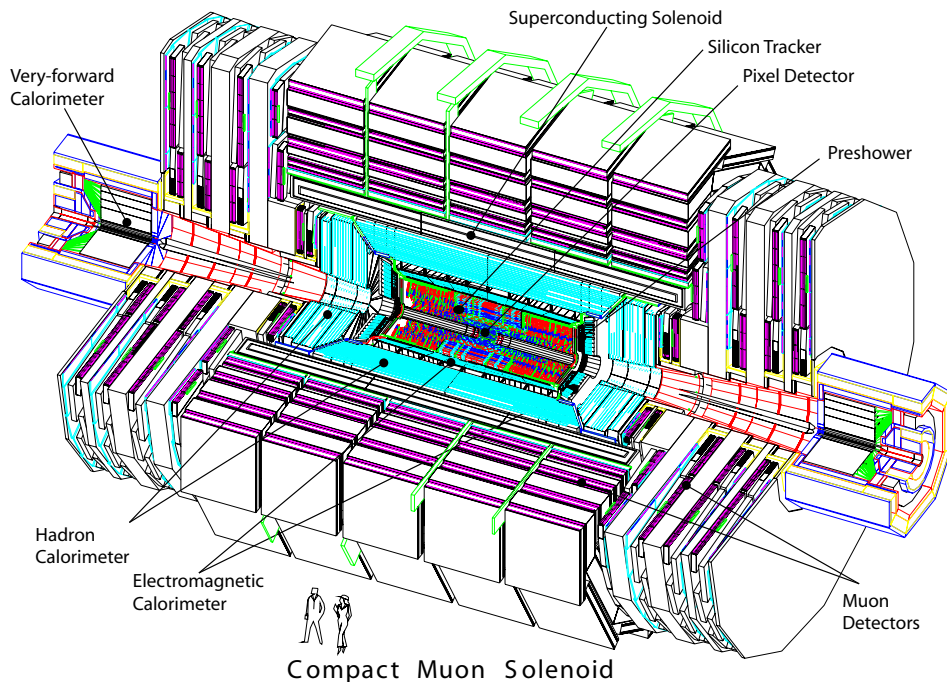


Figure 2.2: A cut-away view of the CMS detector. The different detector components are shortly described in the text.

These requirements led to the detector design shown in Figure 2.2. The beam pipe is surrounded by the silicon tracker which consists of 3 pixel and 10 strip layers in the barrel plus 2 pixel and 12 strip disks at each end of the detector. Going outward, the electromagnetic and the hadronic calorimeter follow. All these parts are located within a superconducting solenoid which provides a 4 T magnetic field parallel to the beam axis. The muon detectors and the return yoke complete the experiment. All subdetectors consist of a barrel and two forward parts to achieve an almost hermetic coverage.

The CMS coordinate system originates from the nominal interaction point, with the  $z$ -axis pointing along the beam axis. The  $x$ -axis points radially inward toward the centre of the LHC, the  $y$ -axis vertically upward. The azimuthal angle  $\phi$  is measured from the  $x$ -axis in the  $x$ - $y$  plane. The pseudorapidity is defined as  $\eta = -\ln(\tan(\theta/2))$ , with the polar angle  $\theta$  measured from the  $z$ -axis.

### 2.2.1 The Solenoid

The choice to use a solenoid magnet with a uniform magnetic field along the beam axis greatly determined the design of the whole detector. Since the momentum resolution of the tracker scales as  $B^{-1}$ , the magnetic field strength was maximised by using superconductor technology, which allows for a field of 4 Tesla. The flux is returned through a yoke consisting of five wheels and two endcaps with integrated muon stations. As a consequence of the strong field, charged particles with transverse momentum smaller than approximately 1.6 GeV will loop inside the tracker. These particles will be swept away from the barrel calorimeters and will deposit their energy in the endcaps, thereby introducing an error in the measurement of the missing transverse energy.

### 2.2.2 The Silicon Tracker

The design of the Silicon Tracker is determined by the expected charged particle flux as a function of the distance to the interaction region. At a distance of 4 cm a flux up to 100 MHz/cm<sup>2</sup> is expected. To cope with the huge number of charged particles the innermost part of the detector is built as a silicon pixel detector. Further away ( $r > 20$  cm) the pixel detector is complemented by a silicon strip detector. The flux at these distances is already low enough, so that even for heavy ion collisions the occupancy of the strips is expected to be below 20%. In the barrel the three pixel

and ten strip layers allow for the measurement of up to thirteen points per track. The endcap consists of two pixel and twelve strip disks, covering a pseudorapidity range up to  $|\eta| = 2.4$ . The performance of the tracker is illustrated in Figure 2.3, which shows the transverse momentum resolution as a function of pseudorapidity. In the central region the resolution is about one percent.

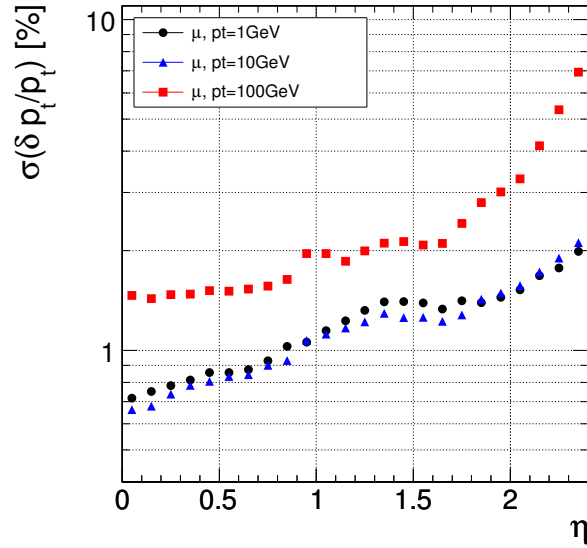


Figure 2.3: Transverse momentum resolution for muons with transverse momenta of 1, 10, 100 GeV as a function of pseudorapidity [11].

### 2.2.3 The Electromagnetic Calorimeter

The aim of the Electromagnetic Calorimeter (**ECAL**) is to measure precisely the energy as well as the direction of electrons, photons and jets. The chosen system consists of 75848 lead tungstate crystals ( $\text{PbWO}_4$ ). Its high density ( $8.2 \text{ g/cm}^3$ ) leads to a short radiation length and narrow showers, which allow for a compact design and a fine granularity. As seen from the nominal interaction point, the barrel crystal cover  $1^\circ$  in  $\Delta\phi$  and  $\Delta\theta$ . Together with the endcaps, it covers the range  $|\eta| < 3.0$ . The **ECAL** thickness in units of radiation lengths is larger than 25. The energy of an electron with  $E > 20 \text{ GeV}$  can be determined with a resolution below one percent (see Figure 2.4).

### 2.2.4 The Hadronic Calorimeter

Analogous to the [ECAL](#) the purpose of the Hadronic Calorimeter ([HCAL](#)) is to measure the direction and energy of strongly interacting particles and jets. The [HCAL](#) has a sandwich structure of brass absorbers and plastic scintillators. These materials have small interaction lengths while minimising multiple interactions for traversing muons. As the [ECAL](#), the barrel and endcap parts of the [HCAL](#) cover the range  $|\eta| < 3.0$ , but with larger granularity. The [HCAL](#) is completed by additional scintillators inside the muon barrel layer and steel/quartz fibres in the very forward region  $3.0 < |\eta| < 5.0$ . Depending on the pseudorapidity, its thickness is 10–15 interaction lengths. This results in an energy resolution, which is about 17% for 50 GeV pions (see [Figure 2.4](#)).

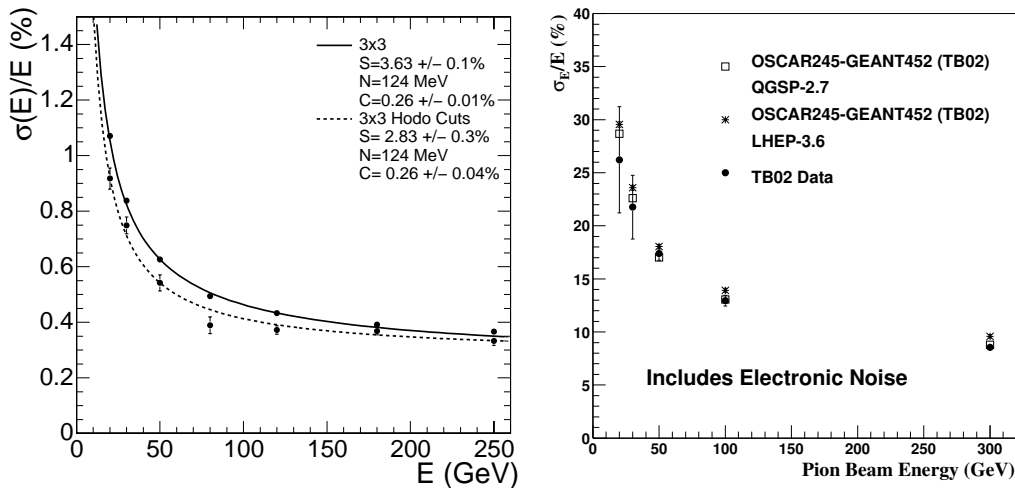


Figure 2.4: Energy resolutions of the ECAL (left plot) and the HCAL (right plot) as measured in test beams. In case of the ECAL, the test particles were electrons, in case of the HCAL charged pions. The figures were taken from the CMS Technical Design Report, Volume I [11].

### 2.2.5 The Muon Chambers

As the name of the experiment suggests, the detection of muons plays an important role in [CMS](#). The reason for this is the fact that many events of interest have muons in their final state, which can be easily triggered on. The [CMS](#) muon system uses several



techniques to identify and measure muons: drift tubes (DT), cathode strip chambers (CSC), and resistive plate chambers (RPC). The drift tubes are used in the barrel region, where the muon rate and the magnetic field strength are low. In the endcaps the cathode strip chambers with faster response time and finer segmentation are used. Finally, the resistive plate chambers provide a fast signal for the trigger systems. The muon system covers the region  $|\eta| < 2.4$ . While the muon system is essential for the muon identification, the accuracy of the transverse momentum measurement relies on the inner silicon tracker as long as the transverse momentum is below 200 GeV, see Figure 2.5.

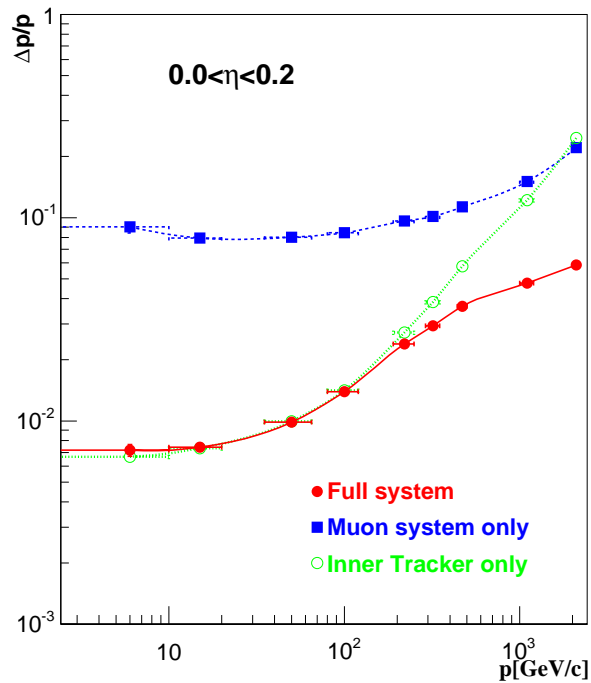


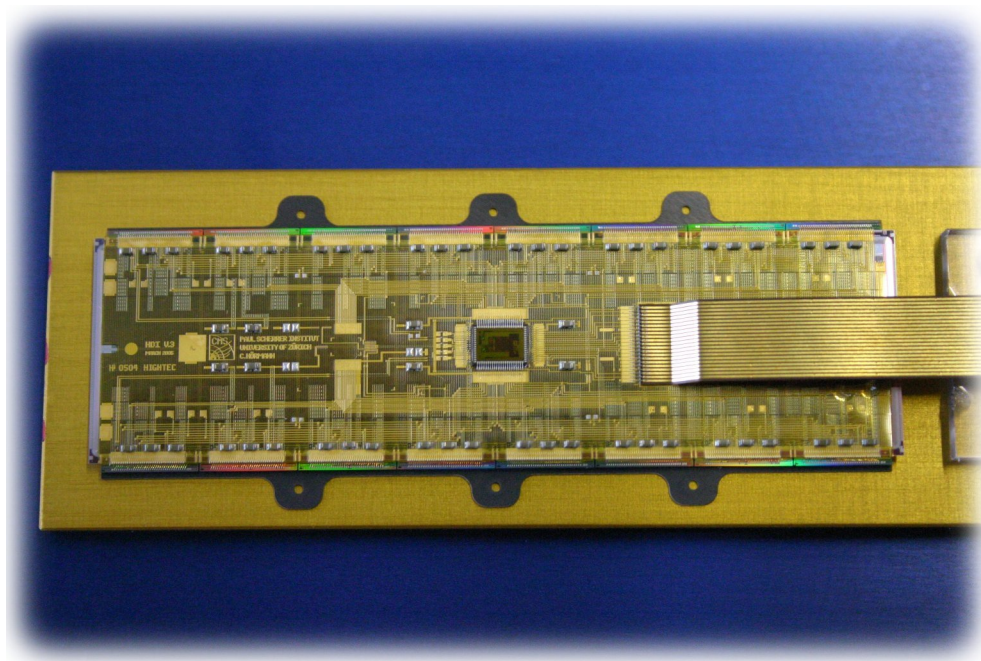
Figure 2.5: Momentum resolution for muons in the central detector. The additional hits in the muon systems get important only for momenta above 200 GeV [11].

### 2.2.6 The Trigger System

The CMS trigger system decides in two steps, which events will be written to tape. The first trigger level, called Level-1 trigger, reduces the event rate from 40 MHz to 100 kHz. This decision takes place within  $3.2 \mu\text{s}$  and depends only on the information of

the calorimeters and the muon detectors. The second trigger level is called High Level Trigger ([HLT](#)). Its decision depends on the data of all subdetectors. In contrast to the Level-1 trigger, which is implemented in hardware, the [HLT](#) is purely implemented in software. It further reduces the event rate by three orders of magnitudes down to 150 Hz. Both trigger levels consist of several trigger paths, with the final decision being a logical OR of all the paths. A large fraction of the final bandwidth is assigned to the isolated electron and muon trigger paths. The trigger efficiencies of the isolated, single lepton triggers can be inferred from the Figures [6.1](#) and [6.2](#).

# Qualification of the Modules for the CMS Barrel Pixel Detector



If heaven above can be  
measured, and the foundations  
of the earth searched out  
beneath . . .

---

*Jeremiah 31, 37*

## Chapter 3

# The CMS Pixel Detector

### 3.1 Introduction

The CMS tracking system consists of two subdetectors: the silicon strip and the silicon pixel detector, the latter being the innermost subsystem of the CMS detector. Its purpose is to provide high resolution track hits as close as possible to the interaction point. The large charged track density close to the beam requires the usage of a pixel system, which can provide three dimensional hit information while keeping the pixel occupancy low. The precise measurement of the tracks close to the interaction region is essential to determine their impact parameters. This quantity is the basis for the tagging of  $b$ - and  $\tau$ -jets as well as the finding of secondary vertices. The pixel detector owes its importance to the use of these techniques in many physics analyses. This chapter introduces the system aspects, which are relevant for the understanding of the module qualifications as described in chapter 4.

### 3.2 Detector Layout

The CMS pixel detector design is based on the following general principles: *precise hit reconstruction* to allow for a precise vertexing, *radiation hardness of all components* to overcome the radiation damage during several years of operation, *minimal material budget* to minimise multiple scattering of the particles, *low noise electronics* to reduce the number of fake hits, *minimal hit losses*, and *affordable costs*.

The overall detector layout is shown in Figure 3.1. The barrel part is 53 cm long

and consists of three layers at radii 4.4 cm, 7.3 cm, and 10.2 cm. Two forward discs will be placed on each side at  $z = \pm 34.5$  cm and  $z = \pm 46.5$  cm with an acceptance up to  $|\eta| = 2.4$ . The whole detector is built in a modular way and contains the huge number of  $66 \cdot 10^6$  channels. To allow for insertion and removal of the pixel detector after the installation of the beam pipe, the pixel detector is built in two halves, which can be smoothly joined together. Figure 3.2 shows a picture of one half of the assembled detector.

The forward modules are slightly rotated to allow for charge sharing between the pixels. If the electric field in the sensor is not parallel to the magnetic field, the moving ionisation charge in the silicon sensor is subject to the Lorentz force, which distributes the charge among several pixels. Knowing the direction of the Lorentz force allows for an improved hit resolution.

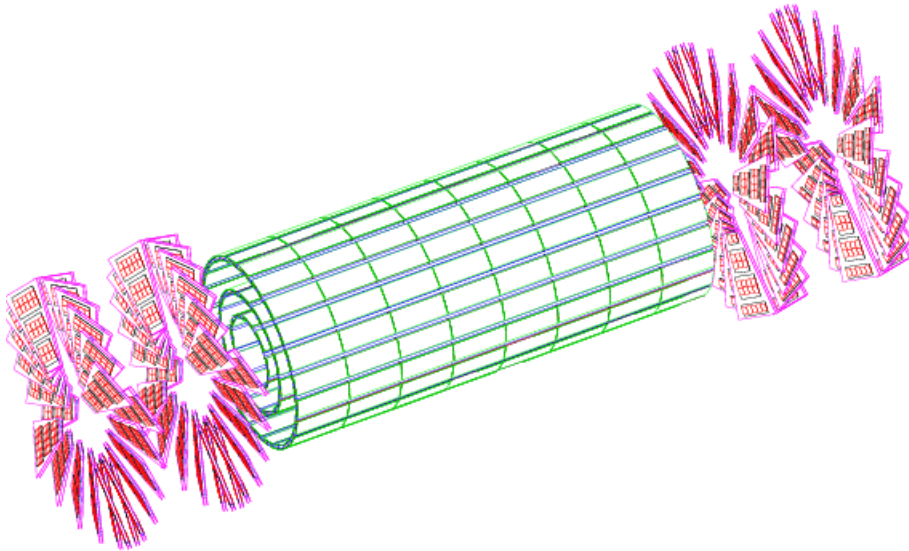


Figure 3.1: Layout of the CMS pixel detector with three barrel layers (drawn in green) and four forward disks (drawn in red).

### 3.3 The Pixel Barrel Modules

There are three types of pixel barrel modules. A standard full module has a size of  $66.6 \text{ mm} \times 26 \text{ mm}$ , weighs 3.5 g, and comprises 66560 pixels. To put the two half shells

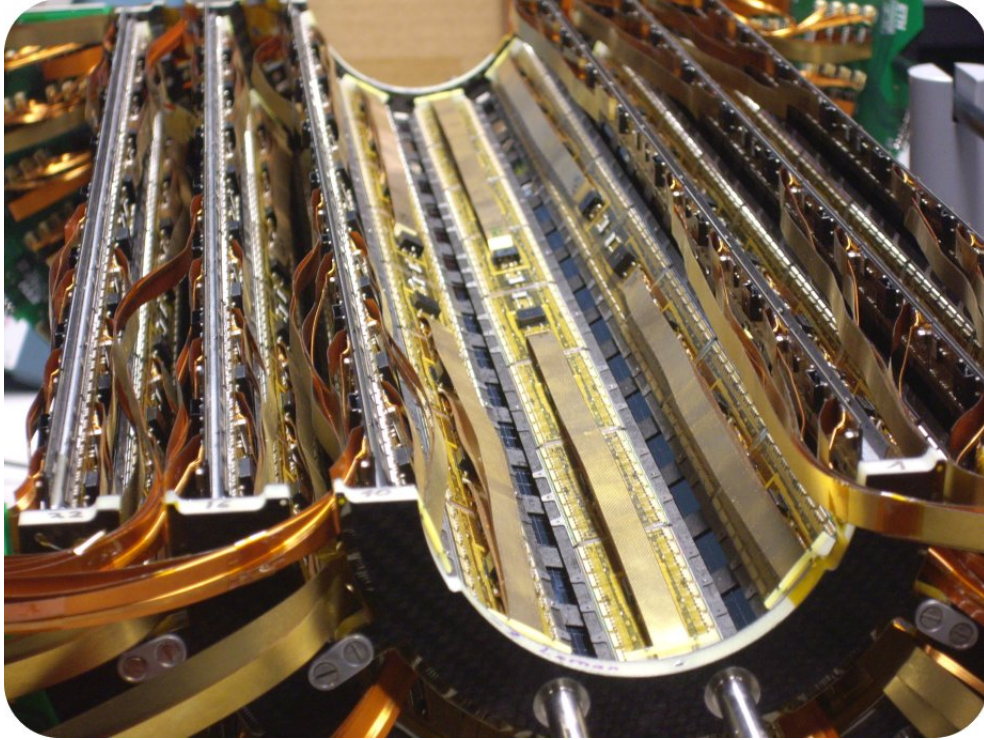


Figure 3.2: Picture of one half of the assembled detector.

of the detector together without a gap, two kind of half modules are necessary. They come in a left- and righthanded version, both containing half of the channels of a full module. Table 3.1 gives the number of full and half modules on the three different detector layers. The modules will be operated in groups containing up to 12 modules. Such a group of modules is called Control Network.

All barrel modules are built out of the following components (see Figure 3.3): The silicon sensor is electrically connected to 16 (8 for half modules) readout chips (ROC). The connection between sensor and ROCs is made of indium bumps [12], which connect each sensor pixel with a pixel unit cell (PUC) on the ROC. On top of the sensor a High Density Interconnect (HDI) serves as an interface to the front end electronics. The connection is established over two cables: The power cable for the necessary supply voltages and the signal cable for the control signals and the analogue readout. The chip on the HDI, which organises the readout of all the ROCs, is called Token Bit Manager (TBM). The connection of the HDI to the ROCs is done with the help of wire

Table 3.1: Number of modules, readout chips (ROCs) and pixels on the three detector layers.

Radius [mm]	# Full modules	# Half modules	# ROCs	# pixels [ $10^6$ ]
41 – 46	128	32	2304	9.6
70 – 76	224	32	3840	16
99 – 104	320	32	5376	22.4
Total	672	96	11520	48

bonds. At the very bottom, the base stripes provide the necessary mechanical rigidity and are used to mount the module onto the support and cooling structure. The main properties of a full barrel module are summarised in Table 3.2.

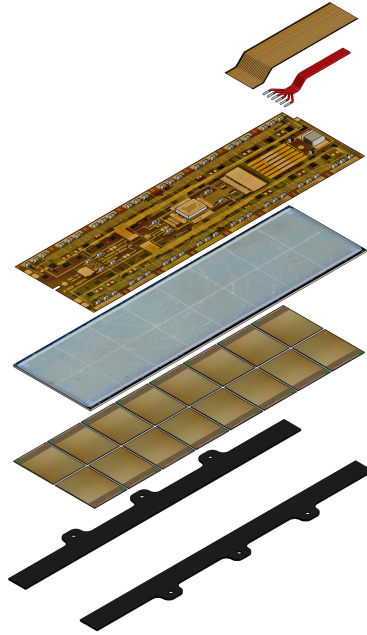


Figure 3.3: Exploded view of a pixel barrel module. The components, from top to bottom, are: The signal cable, the power cable, the HDI, the silicon sensor, the 16 ROCs and the base stripes.

Table 3.2: Properties of the full CMS barrel pixel modules.

Size	66.6 mm $\times$ 26 mm
Weight	3.5 g
# ROCs	16
# Pixels per ROC	52 $\cdot$ 80 = 4160
# Pixels	66560
Pixel size	100 $\mu\text{m}$ $\times$ 150 $\mu\text{m}$ ( $r\phi \times z$ )
Sensor thickness	285 $\mu\text{m}$

### 3.3.1 The Sensor

Due to elastic scattering with electrons, charged particles lose part of their energy when traversing some material. In a depleted semiconductor, some electrons will be excited into the conduction band and an electron-hole pair is formed. For silicon, the necessary energy to create an electron-hole pair is 3.6 eV. By applying an electrical field to the semiconductor, these charge carriers start to move along the electrical fieldlines. This current itself induces a signal in the collecting electrode, which is detectable by the readout electronics.

For the CMS pixel detector, silicon was chosen as the sensor material with  $n^+$ -pixels on a n-type substrate [13]. To achieve a good spatial resolution in both the  $r\phi$  and the  $z$ -direction, an almost squared pixel size of 100  $\mu\text{m}$   $\times$  150  $\mu\text{m}$  ( $r\phi \times z$ ) was implemented. The sensor thickness is 285  $\mu\text{m}$ , which results in an ionisation charge of roughly 23 ke $^-$  for a minimum ionising particle traversing the sensor at a right angle. To fully deplete the unirradiated sensor, a bias voltage of roughly 150 V has to be applied, whereas for the irradiated sensor up to 600 V will be necessary.

### 3.3.2 The High Density Interconnect

The HDI distributes the different signals (like clock or trigger) and voltages to all ROCs. Since the module includes analogue as well as digital parts, three voltages are required: Analogue and digital voltage plus the high voltage for the sensor. These voltages are supplied via the power cable (the lower cable in Figure 3.3). The communication of the HDI with the front end electronics is handled over a multi-channel Kapton cable.



### 3.3.2.1 The Token Bit Manager

A chip placed on the HDI, called TBM [14], has to organise the readout of all ROCs. After having received a trigger, it sends a token to all ROCs, which tells them to send their hits to the TBM. The TBM itself adds a hit counter and some status bits to the data stream. The whole information of a readout is sent as analogue signal to the optical links. Since there will be up to two analogue data links per module, the TBM internally consists of two identical entities, sometimes called TBM A and B. Each of them can control as many as 24 ROCs.

### 3.3.2.2 The Analogue Readout

The modules are read out in a zero suppression mode, i.e. for each hit its position and pulse heights are sent to the front end electronics. An example of such a readout is shown in Figure 3.4. The first eight clock cycles form the TBM header, followed by the readout of all ROCs and terminated by the TBM trailer. The TBM header starts with three ultra black levels (UBL). An UBL is simply a very low level, which marks the lower bound of the analogue signal. The three UBLs are followed by a black level, which defines the zero level of the differential analogue signal. The four remaining clock cycles encode an 8-bit event number. The minimal readout of each ROC starts with an UBL, a black level and a level called “last DAC”. This level displays the value to which the last Digital to Analogue Converter (DAC) was set, or the value of the temperature sensor. Each hit adds a block of six clock cycles to the analogue readout, encoding for the double-column and row index of the hit pixel, as well as for the pulse height. The readout is terminated by the TBM trailer, containing two UBLs, two black levels, plus four clock cycles with the TBM status information.

### 3.3.3 The Readout Chip

The purpose of the PSI46 ROC is to read out the ionisation charge of the sensor pixels at the LHC bunch crossing frequency of 40 MHz and to store the information during the latency of the Level-1 trigger [15]. The ROC is divided into two parts: the active area with one PUC per sensor pixel to read out the collected charge, and the periphery with the control interfaces and data buffers to store the hit information. The active area is organised in 26 double-columns and 80 rows and is therefore able to read out

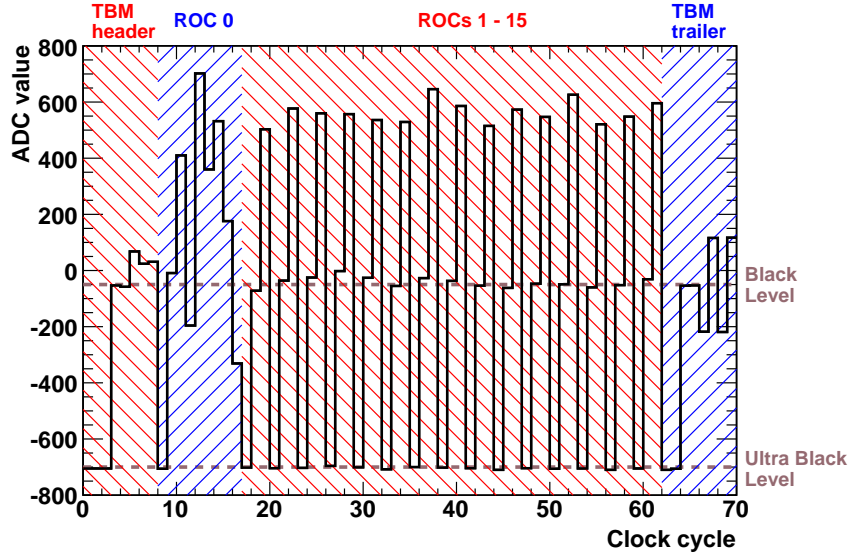


Figure 3.4: Analogue readout of a pixel module with one hit in ROC 0.

4160 pixels. Each sensor pixel is connected to the corresponding **PUC** through an indium bump bond. If a sensor pixel is traversed by a charged particle, the collected ionisation charge induces a voltage signal in the **PUC**. If the amplified signal exceeds a tunable threshold, the periphery of the corresponding double-column periphery is notified. The double-column periphery itself starts the readout mechanism, which stores the position of the hit pixel as well as the pulse height and the bunch crossing in buffers. If the module receives a trigger signal for the corresponding bunch crossing, this hit information is added to the analogue signal.

The behaviour of the **ROC** is controlled by 26 **DACs** and 3 registers. The functionality of those, which are relevant for the following, is described below (cf. Figure 3.5). A full list of all **DACs** and register and their optimisation can be found in [16]. The testing of the readout mechanism is much simplified by the possibility to directly inject a calibration voltage to the preamplifiers, which allows to qualify a module without an external source. The electrical calibration signal is only sent to those pixels, which have a certain switch (labelled “enable” in Figure 3.5) closed. The amplitude of the injected signal is controlled by the *Vcal* **DAC**, its timing by the *CalDel* **DAC**. With the help of the control register (CtrlReg), one of two ranges for the signal amplitude can

be selected (called “low” and “high” range). A signal amplitude in the high range is about seven times higher than in the low range for the same DAC value. The signal from the sensor or the internal calibration mechanism first passes the preamplifier and the shaper. If the comparator finds that the amplitude exceeds some reference voltage, a hit is generated. The reference voltage can be adjusted for each ROC by the *VthrComp* DAC. An individual pixel correction to this global threshold can be applied by setting the four trim bits, which will lower the threshold depending on the value of the *Vtrim* DAC. The comparator of a pixel can be disabled by setting a mask bit. If the signal amplitude exceeds the reference voltage, the pulse height is sampled after a certain time delay, set by the *VhldDel* DAC. If the pixel is enabled (i.e. the “send” switch is closed) the double-column periphery is informed that a hit has occurred.

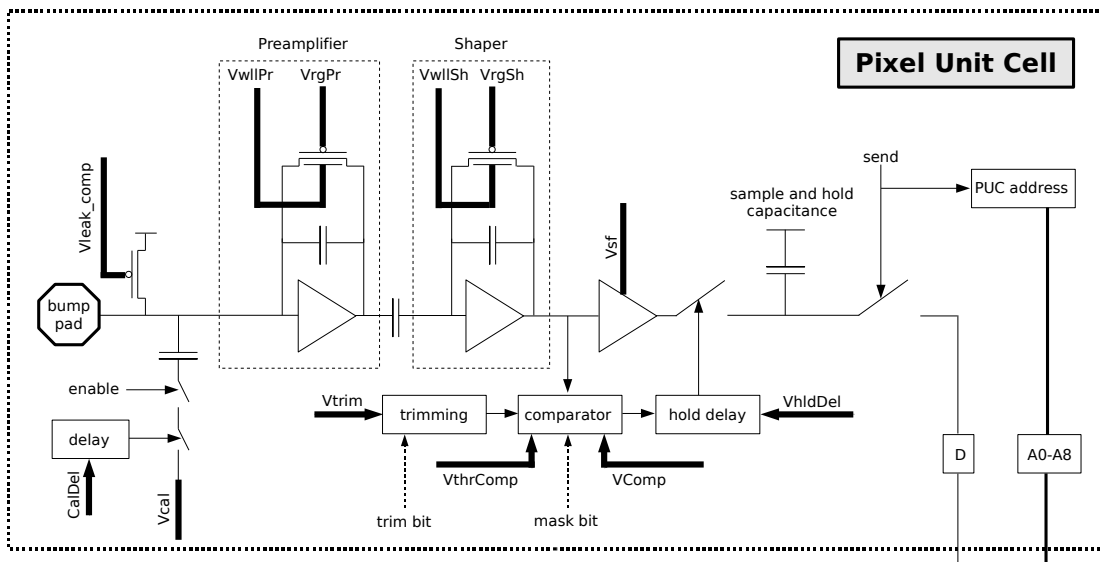


Figure 3.5: Overview of the PUC functionality [16]. The functionality of the relevant parts is described in the text.

To successfully generate and read out a hit in a pixel, the following sequence of actions has to be taken:

1. Enable the double-column of the corresponding pixel
2. Enable the calibration injection to the pixel

3. Enable the readout of the pixel
4. Send a calibration signal to the module
5. Send a trigger signal to the module

In the following the term “to read out a pixel” always refers to this procedure.

Prove all things; hold fast that  
which is good.

---

*1 Thessalonians 5, 21*

## Chapter 4

# Module Qualification

### 4.1 Introduction

After the pixel barrel modules have been fully assembled, they undergo a detailed qualification procedure. To reliably test several hundreds of modules, it was necessary to develop a stable test suite covering all kinds of module operation aspects. The algorithms presented in the following are the results of this effort, which was mainly made during the years 2005 – 2007.

The implemented algorithms can be divided into three groups: functionality tests, which check the correct hardware functionality, performance tests, and the calibration algorithms to extract necessary calibration constants for the successful operation of the modules. The first group contains tests like the pixel readout test and the trim bits test, which check that hits in all pixels can be read out and that the threshold of each pixel can be tuned with the help of the trim bits. The second group includes for example the bump bonding test to validate the connections between sensor pixels and the PUCs. Examples of the third group are the calibration of the temperature sensor or the internal calibration signal of each ROC. The complete qualification procedure takes about six hours for a full module and contains module tests at the temperatures  $T = -10^{\circ}\text{C}$  and  $T = +17^{\circ}\text{C}$  as well as 10 thermal cycles between these two temperatures.

Till end of March 2008 in total 981 modules were fully assembled and tested, out of which 768 had to be selected for usage. Depending on the test results, the modules are assigned to one of three grading categories. The best modules of grade A are going to be used on the two innermost detector layers. Modules of lesser quality but

without severe defects are graded as B, they will be mounted on the third layer. Grade C modules are not going to be used due to their bad performance. Details on the qualification criteria can be found in [17].

If not mentioned otherwise, results are shown for those 806 modules which successfully passed all tests and were classified into the categories A and B. Out of these modules 704 are full modules, 52 are righthanded half modules and 50 are lefthanded half modules. By default the results shown are those of the last test at  $T = -10^{\circ}\text{C}$ .

### 4.1.1 The Test Setup

The test setup consists of the following pieces

- A desktop PC with a Scientific Linux 4 operating system
- Four electronics test-boards, especially designed to test the barrel pixel modules
- Four module adaptor boards to connect the modules to the test-board
- A cool box with space for four modules to keep the modules at constant temperature and humidity
- A Keithley high-voltage supply

The test-board provides the module with the necessary supply voltages and electrical signals (like clock, trigger, ...). To analyse the readout of the module, it includes two 12-bit Analogue to Digital Converters (ADC), which sample the analogue signal in the interval  $[-2048, +2047]$ , with 1 ADC unit corresponding to 0.128 mV. The central control unit of the test-board is formed by a Field-Programmable Gate Array (FPGA) with an implemented processor.

### 4.1.2 The Software Framework

The algorithms have been implemented in a C++ software package called *psi46expert* which runs on a standard PC. For data storage and analysis the ROOT framework [18] was used. Figure 4.1 shows an Unified Modelling Language (UML) diagram of the most important classes. The attributes and operations shown are only typical examples of the complete lists of variables and methods. Likewise the two test classes “Trim”

and “IVCurve” serve as examples for the large number of implemented test classes. Furthermore, classes like those for the graphical user interface, the command line, the logging functionality, . . . are omitted for simplicity.

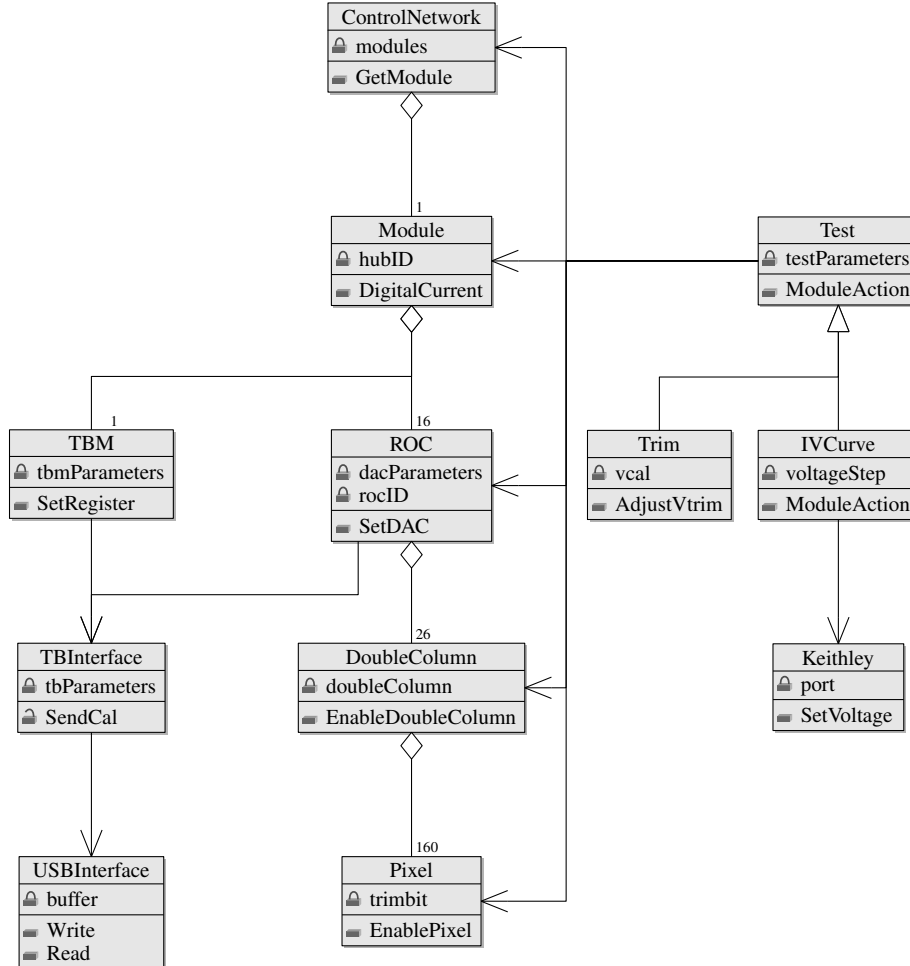


Figure 4.1: UML diagram of the most important classes of the *psi46expert* test software.

The core of the test classes consists of the six classes *ControlNetwork*, *Module*, *ROC*, *TBM*, *DoubleColumn*, and *Pixel*, representing the corresponding hardware entities. They reproduce their functionality like setting a DAC or enabling a pixel. These commands are sent to the test-board represented by the class *TBInterface*. The *DoubleColumn* and *Pixel* classes do not directly communicate with the test-board. All their commands require the specification of the ROC-ID, therefore they are processed via

the *ROC* class. The *TBInterface* class itself makes use of the class *USBInterface* to send its commands to the (physical) test-board.

The *Test* class provides common code to the derived test classes like *Trim* or *IVCurve*. An example for this common code is the function *ModuleAction* which loops over all *ROCs* on a module and executes the test algorithm for this *ROC*. If this behaviour is not suitable for a derived class, as it is for *IVCurve*, the derived class can replace it with its own code. The *IVCurve* uses the class *Keithley* to communicate with the high-voltage supply.

The presence of a processor inside the *FPGA* on the test-board allows to run parts of the test algorithms directly on the test-board. This speeds up the tests by reducing the data transfer between PC and test-board, which is carried out over an USB connection. Especially interactive algorithms, where the test flow depends on the results of previous measurements, as it is the case for the threshold measurement, profit a lot. Table 4.1 shows a comparison of the duration of some test algorithms with and without running parts of the code directly in the *FPGA*. With the help of the *FPGA* processor the full test time could be shortened by a factor of three to four.

Table 4.1: Test duration of different algorithms with and without running parts of the code directly in the *FPGA*.

Test duration per ROC [s]	PC based code	FPGA based code
Trim Bits Test	145	26
Bump Bonding Test	80	20
Noise Measurements	210	89
Trimming	450	156
Pulse Height Calibration	245	20

### 4.1.3 Threshold Measurements

The threshold of a pixel can be measured in different ways. One possibility is to keep the threshold defined by the *VthrComp* *DAC* fixed and to find the *Vcal* value, at which a pixel starts to respond. This kind of threshold will be called “*Vcal*-threshold”. The second possibility is to inject a signal with a fixed amplitude defined by the *Vcal* *DAC*



and to find the  $V_{thrComp}$  value, at which this signal is above threshold. This threshold is referred to as “ $V_{thrComp}$ -threshold”.

Usually this measurement is done by reading out the hits in a fixed bunch crossing. This type of threshold is called in-time threshold. If a pixel has e.g. an in-time  $V_{cal}$  threshold of 60, this does not necessarily mean, that the pixel does not respond for  $V_{cal}$  values lower than 60. It only means that in the given bunch crossing no hits with lower  $V_{cal}$  values are registered. It is well possible, that by reading out the following bunch crossing, signals with lower amplitudes can be observed. This is due to the fact, that lower signals have a longer rise time. If a timing independent threshold is required, the thresholds in different bunch crossings have to be measured. The minimum of all these thresholds is called the absolute threshold. If not mentioned otherwise, a threshold determination usually refers to an in-time  $V_{cal}$ -threshold.

The concrete measurement of a threshold proceeds in the following way. In a first step the considered DAC is varied in steps of 4 DAC units starting from one end of the DAC range. For each value the pixel is read out once. As soon as the response of the pixel changes, the scan stops and the current DAC value is returned. In a second step the threshold curve starting from this rough estimate of the threshold is measured with several readouts per pixels in steps of 1 DAC unit. If the readout efficiency crosses the 50% level, the corresponding DAC value is returned. Due to the step size of 1 DAC value and the limited number of readouts, the precision of this measurement is 1.3 DAC values for 5 readouts per point. Since this threshold measurement has to be executed almost one million times per module during all tests, a more precise measurement by fitting the threshold curve is only done for the noise measurement.

## 4.2 Functionality Tests

### 4.2.1 TBM Test

This test checks some very basic functionalities of the TBM. For both TBMs the communication is probed by reading out the event number. Another test concerns the readout mode of the TBM. The TBM can be read out in a single mode, in which the readout of all ROCs is sent to one analogue channel. This is the default test mode and will be used for the modules in the third layer of the detector. In the dual mode, one half of the ROCs is read out via the first analogue channel, the other half via the

second channel. This will be the readout mode of the modules in the first two barrel layers. The **TBM** test makes sure, that the module can be successfully operated in both modes by checking the length (i.e. the number of **ROCs**) of an empty readout.

All modules graded as A or B show no problems during the **TBM** test. This faultless result is also due to the fact, that modules with defective **TBMs** can be repaired. In such a case the defective **TBM** is not removed, but a new **TBM** is glued on top of it and bonded to the **HDI**.

### 4.2.2 Pixel Readout Test

In the first part of this test, the functionality of the mask bit is checked. By enabling the mask bit of a pixel, the comparator in the **PUC** is disabled (cf. Figure 3.5), thereby suppressing all hits in this pixel. This functionality is very important, since a noisy pixel can prevent a whole double-column from working properly by filling up the buffers in the double-column periphery. Therefore modules with such defects are not used for the final detector. The mask mechanism is checked by enabling the mask bit and trying to read out the pixel. If a hit is generated, the mask bit is defective. During the whole production 4 modules with this kind of defect were found.

In the second part of the test, it is verified that sending a calibration pulse to the enabled pixel, results in the corresponding hit information in the analogue signal. For this, the pixel is read out 10 times with *Vcal* set to a value of 200 in the low range. If the hit does not show up in the analogue signal all ten times, the pixel is called “dead”. Before this test the *VthrComp* and *CalDel* **DACs** have to be properly adjusted as described in [16]. The fraction of dead pixels averaged over all modules amounts to  $2 \cdot 10^{-5}$ .

### 4.2.3 Address Decoding

An individual pixel address consists of five clock cycles in the analogue signal: two cycles encode the double-column index and three the index within a double-column [19]. Each clock cycle can take six different levels (c.f. Fig 3.4). To decode correctly the pixel address, these levels have to be well separated. To check this, the levels of all pixels in a **ROC** are measured and overlaid in a histogram as shown in Figure 4.2. In this histogram, a simple algorithm searches for separated peaks. If exactly six of them have been found, the decoding limits are placed in the centres between two

neighbouring peaks. These limits are used in the second part of the test, which records the analogue readout of each pixel and checks whether the pixel generates the address which corresponds to its physical position on the [ROC](#).

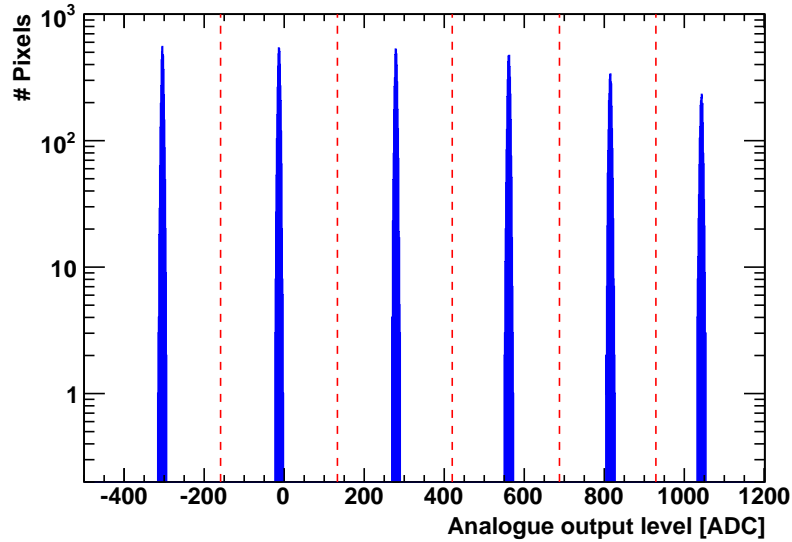


Figure 4.2: Address-levels of all pixels in a ROC. The dashed lines are the separation limits used for the decoding of the pixel addresses.

Before the address levels are measured, the sampling point of the analogue signal is adjusted. This is done by adding some delay to the module clock with respect to the [ADC](#) clock. The sampling point is set to the centre of the range, in which the pulse height is not more than 20 [ADC](#) units apart from the maximal value.

The occurrence of address decoding problems is restricted to some few [ROCs](#). In most cases they occur on [ROCs](#), which have other problems as well. One module was found, on which the addresses of eight otherwise good [ROCs](#) could not be decoded. After the subtraction of these cases, only 5 pixels with address decoding problems remain.

#### 4.2.4 Trim Bits Test

To adjust individually the thresholds of the pixels, each PUC stores four trim bits. By setting them appropriately the pixel threshold is lowered by an amount depending on the  $V_{trim}$  DAC value. In the default untrimmed state, all trim bits are enabled, the corresponding trim value is 15. Disabling single trim bits will lower the pixel threshold. To test whether all four bits work as expected, the threshold is first measured in the untrimmed state. Afterwards all trim bits are enabled one after another and each time it is checked, that the threshold has decreased with respect to the untrimmed threshold. The  $V_{trim}$  values used for the different trim bits are listed in Table 4.2. If the threshold difference is less than 2 DAC units, the trim bit is considered as defective. Figure 4.3 shows the threshold difference distributions for a ROC with no defects. For all pixels the threshold decreased by more than 10 DAC units.

Table 4.2:  $V_{trim}$  values used in the trim bit test.

Trim value	$V_{trim}$ DAC
15	0
14	250
13	200
11	150
7	100

Trim bit defects occur very rarely. Table 4.3 gives the number of defects found in a total of 50,252,800 pixels separated for the four different bits. The defects are equally distributed among the different trim bits.

## 4.3 Performance Tests

### 4.3.1 Noise Measurements

To identify noisy pixels, which potentially have to be masked, the noise of each single pixel is measured. The noise is determined by measuring the so called S-curve, which is the response efficiency of the pixel as a function of the amplitude of the calibration

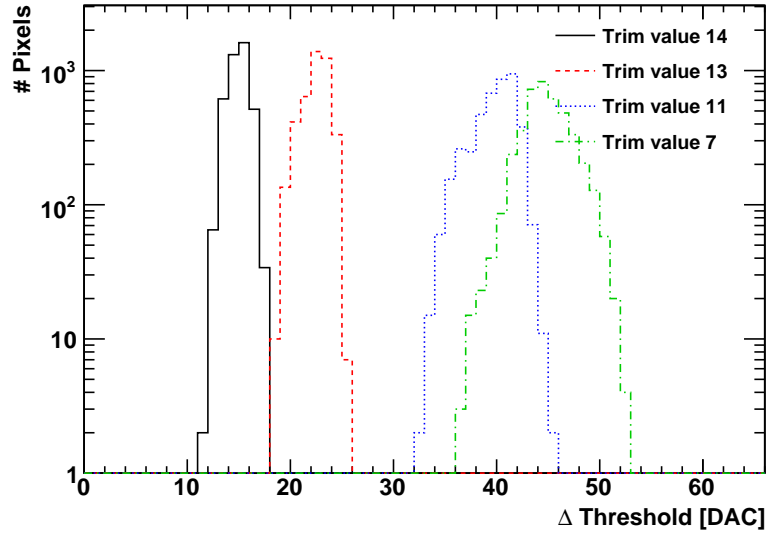


Figure 4.3: Distributions of the threshold difference between untrimmed and trimmed pixels. One trim bit was disabled for each of the curves.

Table 4.3: Number of trim bit defects for the four different bits.

Trim value	# defective pixels
14	10
13	10
11	10
7	11

signal. For an ideal pixel without any noise, this would be a simple step-function: zero efficiency below the signal threshold and full efficiency above. The effect of the noise is to smear out this step function. If the noise is assumed to be Gaussian, the S-curve has the shape of an *error function*, with a width proportional to the noise. A fast threshold scan provides a rough value for the threshold. In a window around this value the S-curve is measured with high precision, i.e. 50 readouts per point.

The measurement is complicated by the fact, that the voltage of the calibration signal is not a monotonous function of  $V_{cal}$ . There are a few cases, where a higher

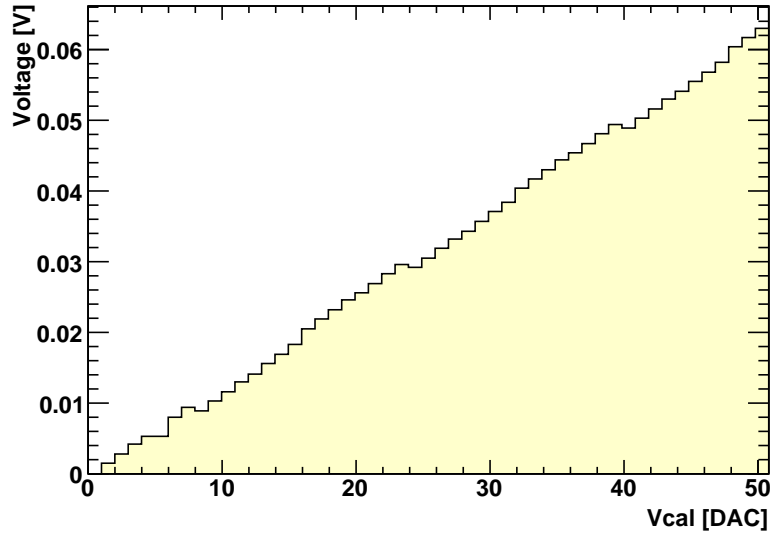


Figure 4.4: Part of the calibration curve of the  $V_{cal}$  DAC. For some DAC values a higher  $V_{cal}$  DAC value corresponds to a lower voltage.

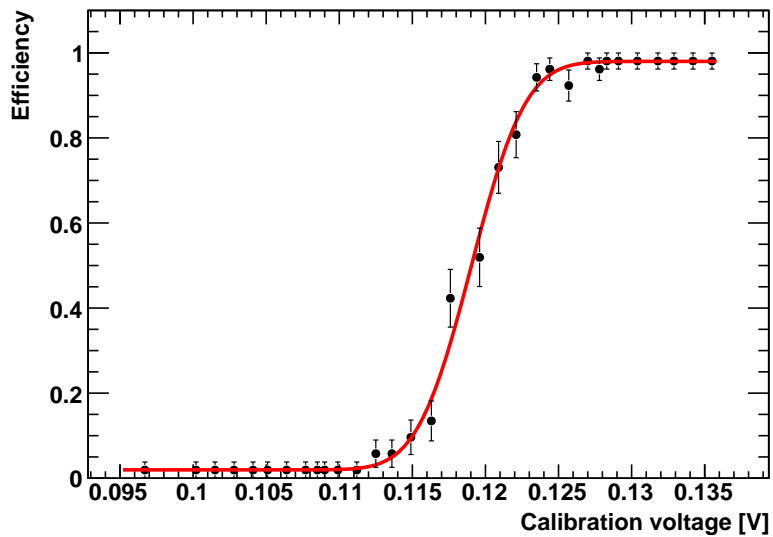


Figure 4.5: S-curve fit with an *error function* to determine the noise of a pixel.

$V_{cal}$  DAC value corresponds to a lower voltage. The calibration voltage was measured as a function of  $V_{cal}$  for one ROC, see Figure 4.4. This measurement is used to plot the efficiency directly as a function of the calibration voltage. These data points are then fit with an *error function* and the width and the position of the 50% point are extracted, see Figure 4.5. The width is first converted to  $V_{cal}$  DAC units (1  $V_{cal}$  DAC = 1.20 mV) and afterwards to electrons (1  $V_{cal}$  DAC =  $65 e^-$ ). With this procedure, the noise of a pixel can be determined with a precision of  $13 e^-$ .

As can be seen in Figure 4.6, the noise level depends on the size of the pixel. Edge pixels on the three inner sides of the ROC which are twice as large as the default pixels, exhibit a larger noise level. The two corner pixels on the inner side with their fourfold size are even noisier. The noise level of the default size pixels turns out to be of the order  $155 e^-$ , edge pixels have a noise level of about  $185 e^-$  and corner pixels of  $230 e^-$ .

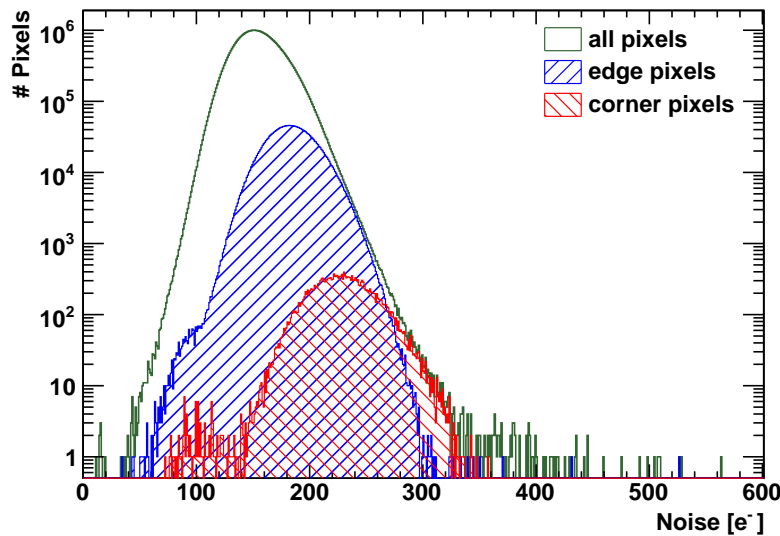


Figure 4.6: Noise levels determined from the width of the S-curve shown for all pixels, edge pixels and corner pixels.

Alternatively the noise can be determined from the pulse height measurement. For a fixed signal amplitude, the pulse height is measured 1000 times and the Root Mean Square (RMS) of the resulting distribution is computed. Since other sources like the

ADC, also contribute to the width of the distribution, the RMS of the black level distribution is measured and quadratically subtracted from the pulse height RMS. To compare the resulting number with the result from the S-curve method, it has to be converted into a charge. This is done with the help of the pulse height gain. Up to a mean offset of  $20 e^-$  a good agreement between the two methods is found, thereby confirming that the S-curve width originates from the noise. Figure 4.7 shows the result of both measurements for the same ROC.

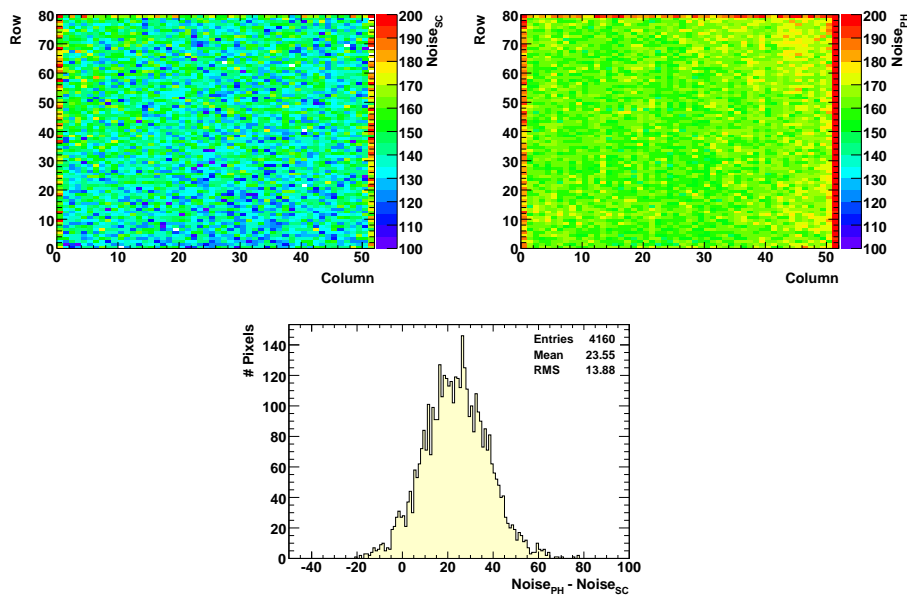


Figure 4.7: Pixel noise measured with two different methods: From the width of the S-curve (top left), from the pulse height scattering (top right), and the difference of the two methods (bottom).

### 4.3.2 Bump Bonding Test

An indium bump bonding process for silicon pixel detectors has been developed at PSI [12]. To test the bump bonding quality, a fast algorithm using the possibility to send a calibration signal through the sensor was devised [20]. The calibration signal can either be injected directly to the preamplifier (using switch 1 in Figure 4.8) or to a pad on the ROC surface (using switch 2 in Figure 4.8). Choosing the second option, the



calibration signal induces a charge in the sensor, which mimics a hit in the sensor pixel. Ideally, this hit is detected if the bump bond is present and not if the bump bond is missing. This ideal situation is deteriorated in two ways. Occasionally the bump bond is not completely missing but only has a poor connection to the sensor or the ROC. Furthermore, for large enough amplitudes of the calibration signal, a hit is triggered although the bump is missing. These hits are supposed to originate from cross-talk via a parasitic coupling between the calibration voltage line and the preamplifier.

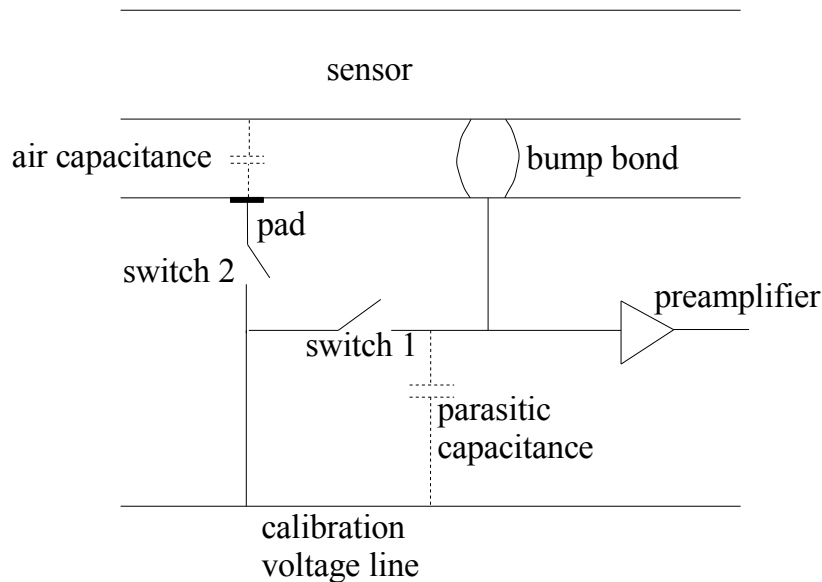


Figure 4.8: Sketch of the PUC components relevant for the bump bonding test.

Based on this experience, the following algorithm was developed, to check the bump bonding quality. First the  $V_{cal}$ -threshold for the signal injection through the sensor is determined. Second the threshold for the parasitic cross-talk is measured (i.e. with both switches open). The difference of the two thresholds (both measured in the high  $V_{cal}$  range) allows for a good discrimination between bonded and unbonded pixels. If the bump bond is missing, both thresholds are more or less equal, otherwise the difference amounts to  $-10$  to  $-20$  DAC units. It is found that the discrimination

between good and bad bump bonds is the better, the higher the threshold (i.e. the lower the  $VthrComp$  value). This is made use of by setting the  $VthrComp$  DAC to a value, which is as low as possible, but still large enough in order to detect the pixel response due to the cross-talk.

The procedure has been validated by applying it to several specially prepared ROCs with sensors, from which a few bumps were removed manually before the bump bonding process. Figure 4.9 shows an example of a threshold difference distribution from which all missing bump bonds can be successfully identified.

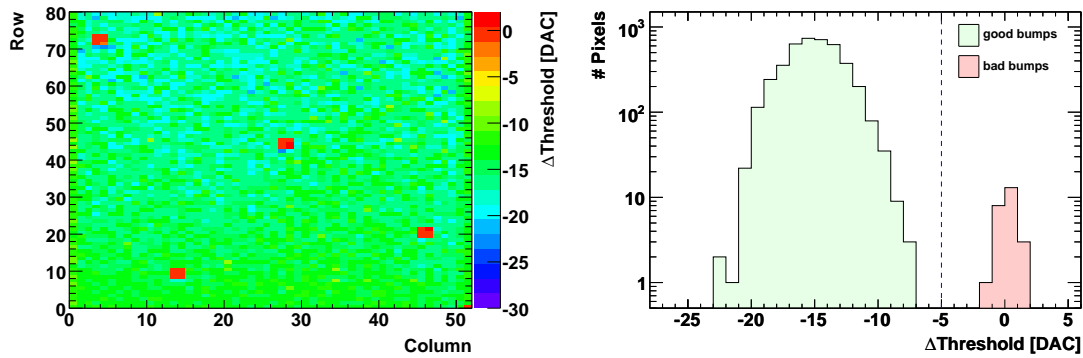


Figure 4.9: Result of the bump bonding test for a ROC with known bump bonding defects. The left figure shows a map of the threshold difference to check the correct identification of the bad bump bonds. The figure on the right shows the threshold difference distribution, pixels with defective bump bonds are shown in red, good bump bonds are plotted in green. All pixels with missing bumps could be identified.

The threshold difference distribution of all tested pixels is shown in Figure 4.10. The distribution shows two peaks, one at a threshold difference of about  $-30$  DAC values and one at vanishing threshold difference. The distribution has a minimum at  $-5$  DAC values, where the border between good and bad pixels was set. The fraction of pixels with bump bonding defects on grade A and B modules is  $1 \cdot 10^{-4}$ . With the help of this test, modules like the one shown in Figure 4.11 with many defects in the corners and along the ROC boundaries were successfully identified. In the course of the module testing, the bump bonding test was incorporated into the test of the bare modules, i.e. before the HDI has been mounted. In this way, badly bonded modules could be sorted out already at this stage, thereby saving a considerable amount of

HDI.s.

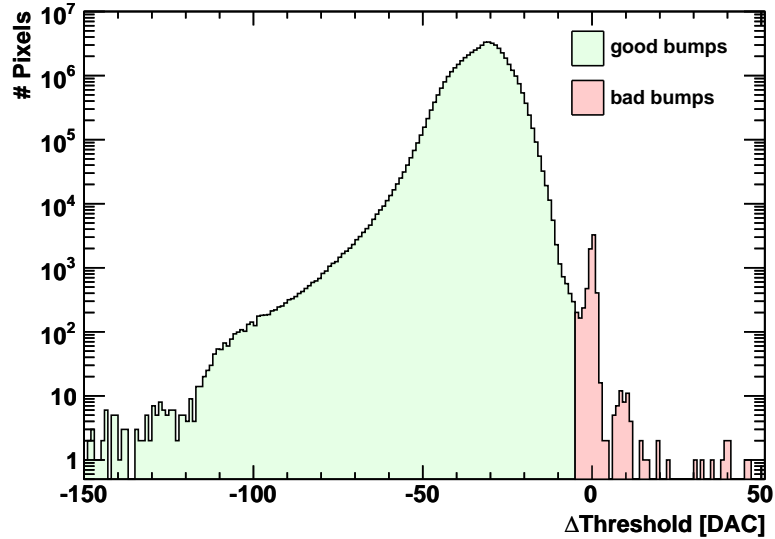


Figure 4.10: Threshold difference providing a measure for the bump bonding quality of each pixel (see text for details). Good connections are shown in green, bad in red.

### 4.3.3 Sensor IV-curve

Defects in the silicon sensor are most easily found by measuring its leaking current as a function of the applied bias voltage. Problems with scratches or spikes would show up as breakdown at voltages below 100 V [21]. Since the sensor will be operated at voltages up to 600 V, the high-voltage is varied from 0 V to 600 V in steps of 5 V. The measurement of the leakage current is performed 5 s after the voltage has been set. The error on the current measurement estimated from repeated measurements of the same module is  $2.1 \cdot 10^{-3} \mu\text{A}$ . The algorithm stops, if the voltage is either at 600 V or the leakage current exceeds  $100 \mu\text{A}$ . The latter happens for many modules, but this is not considered as a problem if the breakdown voltage is above 200 V, since the behaviour of the sensor is expected to improve with irradiation. A typical sensor IV-curve of a good module is shown in Figure 4.12.

Figure 4.13 shows the measured leakage current for all grade A and B modules at

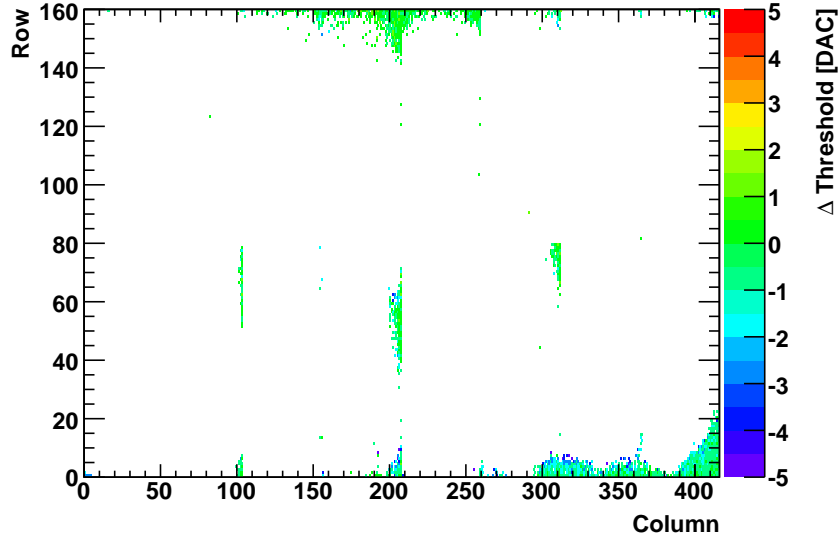


Figure 4.11: Bump bonding map of the module M0086 with many defects in the corners and along the ROC boundaries. The coloured points represent pixels with bad bump bond connections.

a temperature of  $T = -10^{\circ}\text{C}$ . A too large sensor leakage current is by far the most common reason why fully assembled modules are not used for the detector.

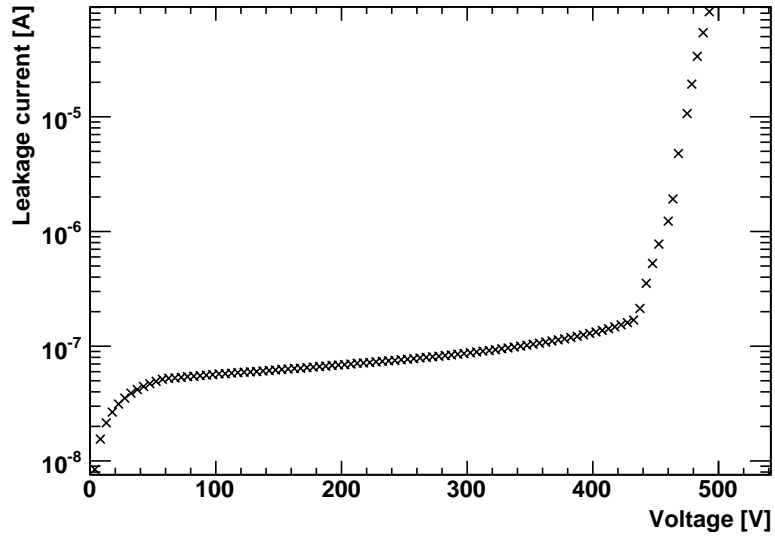
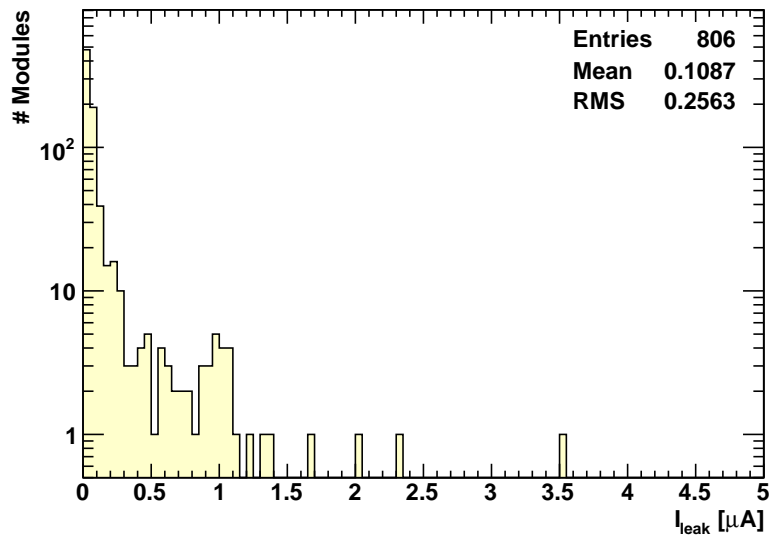
## 4.4 Calibration Tests

### 4.4.1 Trimming

#### 4.4.1.1 The Trim Algorithm

Due to variations in the electronic components, each pixel has a slightly different threshold. To achieve a uniform threshold for all pixels, the trim bits of each pixel have to be programmed to a suitable value. To do this, the trimming algorithm described below was developed.

The only input parameter to the trim algorithm is the threshold (in  $V_{cal}$  units) to which the response of all pixels should be unified to. The three degrees of freedom which have to be properly adjusted are the  $V_{thrComp}$  DAC, the  $V_{trim}$  DAC, and the

Figure 4.12: Sensor IV-curve of a typical module at  $-10^{\circ}\text{C}$ .Figure 4.13: Measured leakage current for all grade A and B modules at a temperature of  $T = -10^{\circ}\text{C}$ .

trim bit value of each pixel.  $VthrComp$  sets the global threshold for the ROC and  $Vtrim$  determines, how much the trim bits lower this threshold. The influence of  $VthrComp$  and  $Vtrim$  on the threshold can be inferred from Figure 4.14.

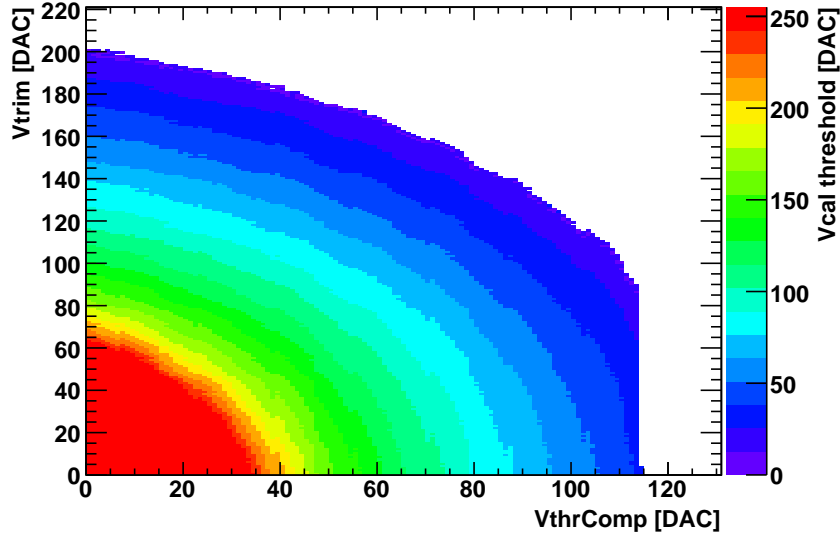


Figure 4.14:  $Vcal$  threshold of a pixel with all trim bits disabled as a function of  $VthrComp$  and  $Vtrim$ . Within the white area no threshold could be determined.

The first step is to find the value of the  $VthrComp$  DAC which corresponds to the chosen threshold in  $Vcal$  units. This is done by measuring for each pixel its  $VthrComp$ -threshold. As for all other threshold measurements of the trim algorithm, the timing independent absolute threshold is measured. Since the thresholds can only be lowered afterwards, the minimum value of this distribution determines the global  $VthrComp$  value (a low  $VthrComp$  value corresponds to a high threshold). This value is used during the rest of the algorithm. As can be seen from Figure 4.14 there is a maximal  $VthrComp$  value above which the ROC is not functional any longer. It turns out, that this limit has almost the same value for all pixels. In order to operate not too close to this limit, it is ensured, that the chosen  $VthrComp$  value is at least 10 DAC values apart from this upper limit.

The second step of the trim algorithm is to determine an appropriate  $Vtrim$  value. To find this, the  $Vcal$  thresholds of all pixels are measured. The pixel which has the

highest threshold is used to determine the necessary  $V_{trim}$  value. For this pixel the trim value is set to zero and  $V_{trim}$  is increased, until the threshold of the pixel is at the same level as the target threshold.

The third step of the trim algorithm consists in setting the trim bits for all pixels. This is done by a binary search for the trim value, which gives a threshold as close as possible to the target threshold. The search starts with a trim value of 7 and comprises four iterations. At the end, all thresholds are measured once again to validate the procedure.

#### 4.4.1.2 Test Results

The trim algorithm was run for all ROCs for a target threshold of  $V_{cal}$  equal to 60. The threshold distributions before and after setting the trim bits are shown in Figure 4.15. The spread of the distribution could be reduced by a factor of 3.8.

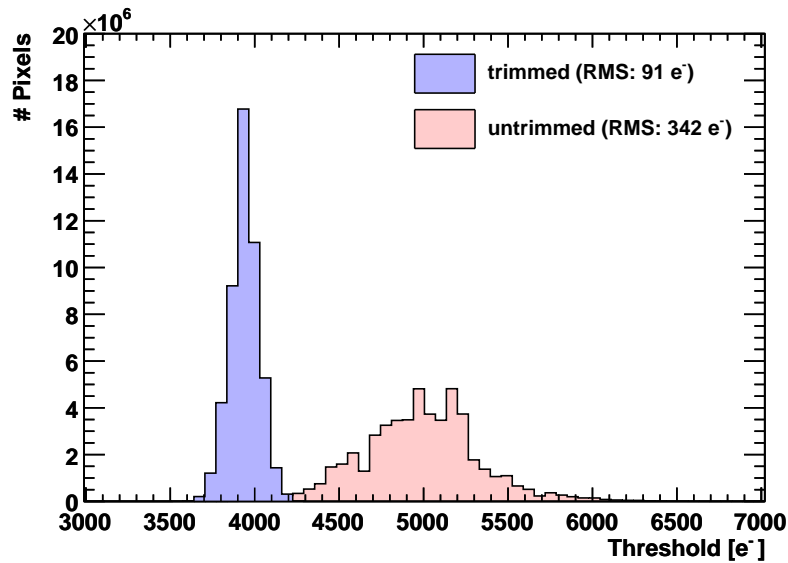


Figure 4.15: Threshold distribution of all pixels before and after setting the trim bits.

#### 4.4.1.3 Trimming for Very Low Thresholds

For a not too low target threshold, the trim values fill the whole range from 0 (maximally trimmed) up to 15 (not trimmed). The presence of the upper  $VthrComp$  limit poses a problem, when trimming for very low thresholds is aimed for. In this case, the  $VthrComp$  DAC can not be set as high as desired in step one. This is compensated by a higher  $Vtrim$  value in step two, but at the price of a trim value distribution, which does not make use of the full available range. The trim value distributions after the trimming to thresholds equal to  $Vcal$  20 and 60 are shown in Figure 4.16. For the former threshold the trim values fill only the range from 0 to 12, thereby rendering the threshold distribution more coarse.

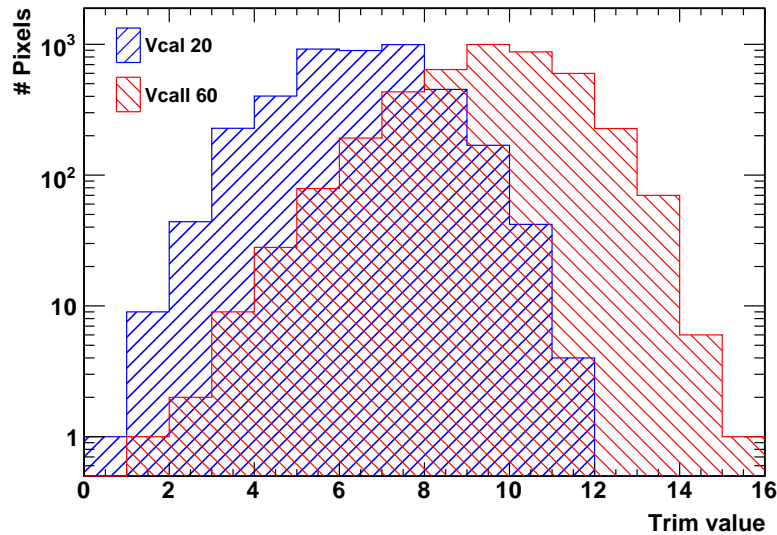


Figure 4.16: Trim value distribution after trimming to thresholds corresponding to  $Vcal$  20 and 60. In the former case the trim values do not cover the full range, due to the upper  $VthrComp$  limit.

#### 4.4.1.4 Parametrised Trimming

With the final system it is not possible to run highly interactive algorithms as the trim algorithms described above, because the detector control and readout systems



(the Front End Controller (**FEC**) and Front End Driver (**FED**)) are separated. A solution to this problem is to use the trim parameters measured during the module qualification in the laboratory. During this procedure each **ROC** is trimmed to a threshold corresponding to 60 *Vcal* DAC units. It turns out that it is possible to extrapolate these trim parameters to any other threshold by parametrising them as a function of the threshold [22]. To obtain these parametrisations the trim algorithm was run for different thresholds. It is found, that *VthrComp* and *Vtrim* depend linearly on the threshold. The trim bits do not change significantly with the threshold. From the average of 16 **ROCs** the following parametrisation was deduced:

$$\begin{aligned} VthrComp(thr) &= VthrComp(60) - 0.65 \cdot (thr - 60) \\ Vtrim(thr) &= Vtrim(60) - 0.45 \cdot (thr - 60) \\ trim\ bits(thr) &= trim\ bits(60) \end{aligned}$$

To validate the procedure, this parametrisation was applied to a **ROC** and the resulting thresholds were measured, see Figure 4.17. The measured thresholds deviate only little from the target thresholds. The widths of the threshold distributions are only slightly larger than those obtained by the full trim algorithm.

#### 4.4.2 Pulse Height Calibration

The spatial hit resolution of a pixel detector can be improved by using an analogue instead of a binary readout. This is also made use of by the **CMS** pixel detector, by measuring the pulse height of the induced signal. To profit from the analogue readout, it is very important to know exactly to what ionisation charge a measured pulse height corresponds to. A first step is to calibrate the pulse height with the internal calibration mechanism in terms of the *Vcal* DAC. *Vcal* itself can only be calibrated with an external source (see below).

A typical pulse height calibration curve is shown in Figure 4.18. There is usually a large region with a linear dependency, for large amplitudes the pulse height saturates, while for very small amplitudes there might be some nonlinearity too. Since the variations between pixels can be quite large, this calibration is ideally done for each pixel separately. One pixel after another is enabled, calibration signals with various amplitudes are injected and the pulse heights are measured. The *Vcal* DAC values for

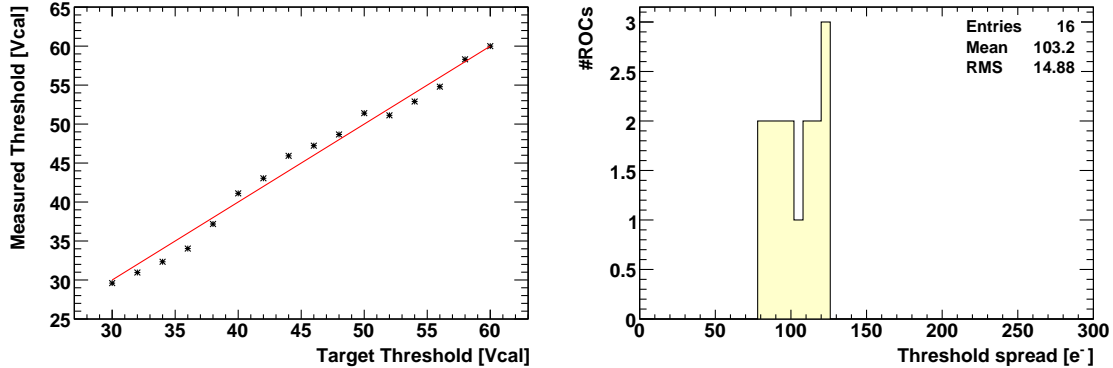


Figure 4.17: Validation of the parametrised trimming. The trim settings were extrapolated from the results of the trim algorithm for a threshold corresponding to a  $Vcal$  value equal to 60 to a variable target threshold using the parametrisation described in the text. The plot on the left shows the measured threshold versus the target threshold, while the plot on the right shows the measured threshold spread.

which the pulse heights are measured are the following: 50, 100, 150, 200, 250 in the low  $Vcal$  range and 30, 50, 70, 90, 200 in the high  $Vcal$  range. In order to measure the pulse height for the low  $Vcal$  values, the threshold and the timing of the injected signal have to be adjusted. This is done as described in [16]. To increase the accuracy, each pulse height measurement is an average over 10 readouts.

In the offline part of the algorithm the points are fit with two different functions. First the central points (the 10 points without the highest and the two lowest points) are fit with a straight line. The slope of this curve determines the gain and the  $Vcal$  value, which corresponds to zero pulse height, the pedestal. These values are measured with an accuracy of  $1.5 \cdot 10^{-2}$  ADC/DAC for the gain and  $2.7 \cdot 10^2 e^-$  for the pedestal. Second the whole curve is fit with a hyperbolic tangent function to quantify the nonlinearity for very low pulses. The fit function is

$$y = p_3 + p_2 \cdot \tanh(p_0 \cdot x - p_1). \quad (4.1)$$

To achieve the optimal hit resolution the nonlinearity given by  $p_1$  should be as small as possible (for details see [16]).

The gain and pedestal distributions of the linear part of the pulse height calibration

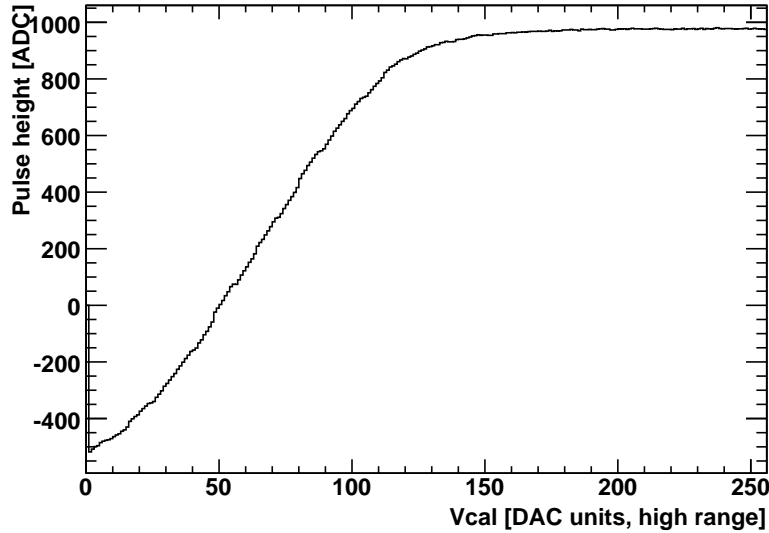


Figure 4.18: The sampled pulse height as a function of the amplitude of the injected signal. For the lowest bin, the pulse height could not be measured because the signal was below the threshold.

curves are shown in Figure 4.19. The average RMS of the gain distributions per ROC amounts to  $9.7 \cdot 10^{-2}$  ADC/DAC, that of the pedestal distributions to  $1.6 \cdot 10^3 e^-$ . The corresponding numbers for the distributions per double-column are  $6.1 \cdot 10^{-2}$  ADC/DAC for the gain and  $9.5 \cdot 10^2 e^-$  for the pedestal. These numbers are important for the question, whether the calibration constants will be applied per ROC, per double-column or per pixel. Since the pedestal variations influence the hit resolution more than the gain variations, it was decided to use the pedestals for each pixel but only an average gain per double-column. In this way, the amount of calibration constants is reduced by almost a factor of two without deteriorating the position resolution significantly.

### 4.4.3 Temperature Calibration

The ROC has a built-in temperature sensor [19]. The temperature is measured by comparing a temperature dependent voltage to a temperature independent reference voltage. The amplified voltage difference is sent to the “last DAC” signal of the analogue output. To extract the voltage difference from the measured ADC value of the

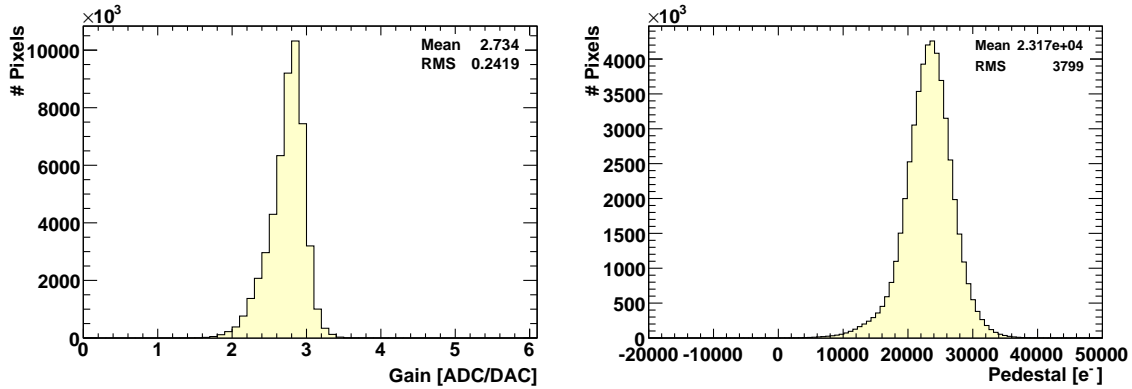


Figure 4.19: Gain (left plot) and pedestal (right plot) of the linear part of the pulse height calibration curves.

“last DAC”, the output signal has to be calibrated. This can be done by using the ROC ability to send a known voltage difference to the “last DAC”. Having measured the voltage difference at two different temperatures and assuming a linear dependency, an absolute temperature measurement is possible.

The sensor is designed to measure temperatures in the range from  $-30^\circ\text{C}$  to  $+70^\circ\text{C}$ . To get a better accuracy of the measurement, the reference voltage (to which the temperature dependent voltage is compared to) can be programmed to be one of eight predefined voltages in the range 399.5 mV to 564 mV. The voltage difference used for the “last DAC” calibration can also be chosen among eight different values from  $-94$  mV to  $+70.5$  mV. The calibration algorithm measures all 16 numbers, although not all of them will be used for the calibration. An example measurement of these quantities is shown in Figure 4.20.

To compute the sensor voltage, a reference voltage has to be chosen for which the voltage difference is not negative and the “last DAC” does not saturate at high values. Concretely, the measured ADC value is required to be larger than 150 ADC units and smaller than the absolute value of the UBL. Having selected a good measurement, the voltage difference for the measured “last DAC” level has to be found. To do this, the points of the “last DAC” calibration measurements which deviate from the black level are fitted with a straight line. This fit is used to determine the measured voltage difference, which is finally added to the known reference voltage. From

repeated measurements of the same ROC at constant temperature, it was found that the temperature sensor voltage can be measured with an accuracy of 0.56 mV.

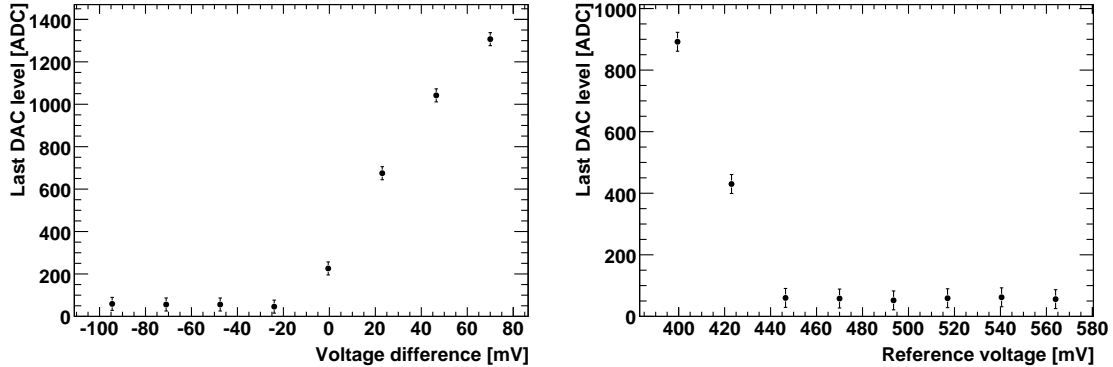


Figure 4.20: Calibration of the temperature sensor. The left plot shows the level of the “last DAC” for the eight known voltage differences in the range from  $-94$  mV to  $+70.5$  mV. The right plot shows the level of the “last DAC” for the voltage difference between the temperature sensor and the eight reference voltages. For the points with an ADC value around 50, the voltage difference was negative and the “last DAC” is around the black level.

To calibrate the temperature sensor of each ROC, the sensor voltage  $V$  was measured at  $T = -10^\circ\text{C}$  and  $T = +17^\circ\text{C}$ . The resulting distributions are shown in Figure 4.21. Averaged over all ROCs, the temperature can be parametrised as a function of the sensor voltage as  $T[^\circ\text{C}] = -4.5 \cdot 10^2 + 0.996 \cdot V[\text{mV}]$ .

#### 4.4.4 Vcal Calibration

In 2005 the first barrel modules underwent a beam-test at PSI (Villigen) with a 300 MeV pion beam [23]. The results indicated, that the same  $Vcal$  value might correspond to different injected ionisation charges for different ROCs. If the beam hits the module e.g. at a right angle, the particles traverse  $285 \mu\text{m}$  of silicon and the ionisation charge distribution is well described by a Landau distribution with a most probable value of  $21,680 e^-$  [24]. It was observed, that the position of this Landau peak in terms of  $Vcal$  DAC units varied between ROCs. From runs at different angles, the ionisation charge can be extracted as a function of the  $Vcal$  DAC. Figure 4.22 shows that the

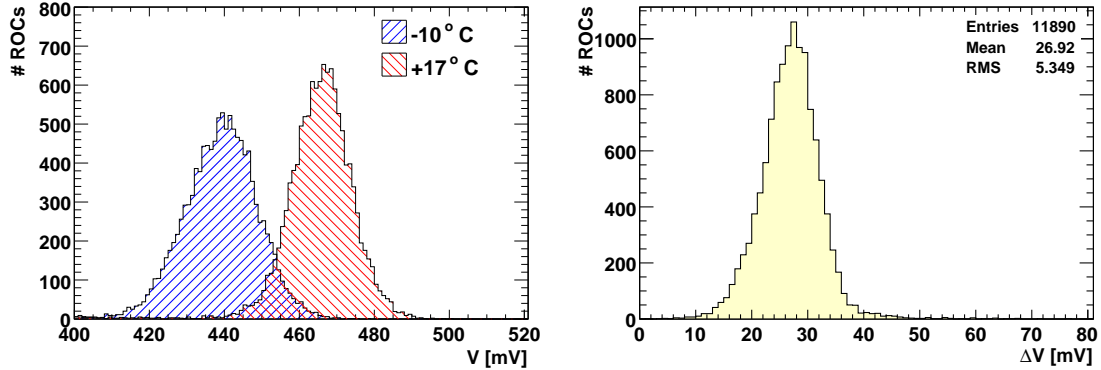


Figure 4.21: The left figure shows the voltage of the temperature sensor for  $T = -10^\circ\text{C}$  and  $T = +17^\circ\text{C}$ , the right figure the voltage difference between these two temperatures for all ROCs.

ionisation charge depends linearly on the  $V_{cal}$  DAC. Astonishingly  $V_{cal}$  equal to 0 does not correspond to zero charge. The mean slope of the 13 ROCs shown in Figure 4.22 is  $61.1 \text{ e}^-/\text{DAC}$  with a RMS of  $5.5 \text{ e}^-/\text{DAC}$ .

The  $V_{cal}$  calibration was repeated in the laboratory with the help of a variable energy X-ray source. The test setup is shown in Figure 4.23. The hit rate is highest for the central ROCs (zone 2) and lowest for the ROCs on both ends of the module (zone 0). The used source consists of a primary Americium-241 source, which excites characteristic X-rays from one of six possible targets (Cu, Rb, Mo, Ag, Ba, Tb). The targets used for the calibration are barium, silver, and molybdenum, which produce between five and nine thousand electron-hole pairs in silicon (see Table 4.4).

Table 4.4: Targets used to produce secondary X-rays of a specific energy. Listed are the X-ray energy, the number of produced electron-hole pairs in silicon as well as the photon yield.

Target	Energy [keV]	Ion. charge in Si [ $\text{e}^-$ ]	Photon yield [ $\text{s}^{-1}\text{sr}^{-1}$ ]
Mo	17.44	4844	$2.43 \cdot 10^4$
Ag	22.10	6139	$3.85 \cdot 10^4$
Ba	32.06	8906	$4.65 \cdot 10^4$

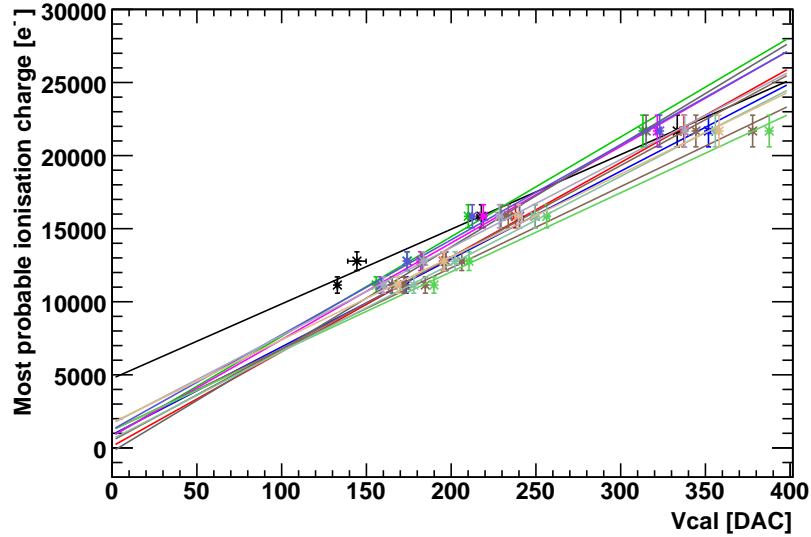


Figure 4.22: Ionisation charge as a function of the  $Vcal$  DAC for 13 ROCs. The points have been extracted from the position of the Landau peak in the 2005 test-beam data.

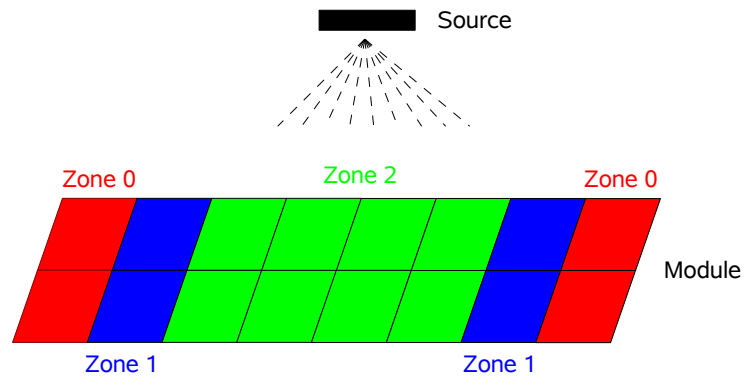


Figure 4.23: Setup of the X-ray test.

The  $Vcal$  value, to which these charges correspond to, is determined in the following way. First, for each ROC the threshold curve is measured by varying  $VthrComp$ . For

each value, the fully enabled module is randomly read out several thousand times and the number of hits in each ROC is determined. To increase the probability to find a hit, the corresponding bunch crossing is artificially stretched by stopping the clock sent to the module. The resulting threshold curve is fit with an *error function* and the 50% point gives the  $VthrComp$  value of the corresponding line. The  $VthrComp$  DAC is set to this value, and for each pixel its  $Vcal$  threshold is measured. The mean of the resulting distribution gives the sought-after  $Vcal$  value. This procedure is repeated for the different targets and the resulting points in the ionisation charge vs.  $Vcal$  plane are fit with a straight line as shown in Figure 4.24.

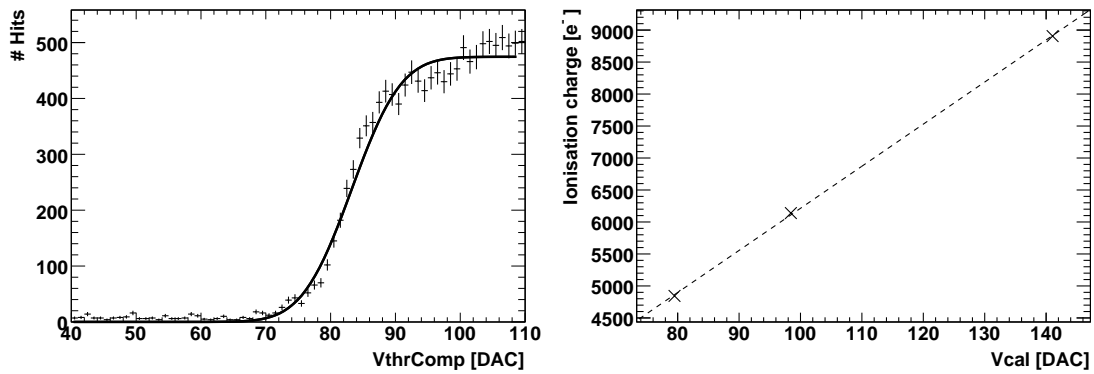


Figure 4.24: Left plot: Example of a threshold curve for the silver line. Right plot: Fit of the  $Vcal$  calibration curve for a measurement with 3 lines.

For most of the modules the calibration was done with only two lines (silver and molybdenum) due to the limited testing time available. A more precise calibration with three lines was performed for a small subset of all modules. Table 4.5 shows a comparison of the different parameters of the two test procedures.

The uncertainty of the measurements was estimated by repeated tests of one module. The precision of the measurements strongly depends on the ROC position on the module. Table 4.6 shows the precision with which the slope of the calibration curve can be determined.

The results of the  $Vcal$  calibration with the help of a variable energy X-ray source are shown in the Figure 4.25. The first figure shows the measured slopes of the calibration curves (ionisation charge vs.  $Vcal$ ) and the second figure their offset for zero  $Vcal$ . The mean slope is found to be  $66 e^-/DAC$ , the mean offset is  $-410 e^-$ . A  $Vcal$  DAC value of



Table 4.5: Comparison of the two-line and the three-line measurements.

	2 lines	3 lines
Measured lines	Mo, Ag	Mo, Ag, Ba
Tested modules	806	69
Test duration	15 min	1 h
Triggers per <i>VthrComp</i> step	30000	5000
Bunch crossing length	25 $\mu$ s	1.6 ms

Table 4.6: Uncertainty of the slope determination for the measurement with 2 and 3 lines.

RMS [ $e^-$ /DAC]	2 lines	3 lines
Zone 0	15.6	1.2
Zone 1	7.6	1.1
Zone 2	5.8	0.6

50 corresponds on average to  $2800 e^-$  (third figure). Therefore trimming to a threshold with  $V_{cal}$  equal to 50 yields a mean threshold below the aimed for  $3000 e^-$  for most of the ROCs.

As shown in Table 4.7 the RMS of the slope distributions after subtraction of the measurement uncertainty is of the order of  $5 e^-$ /DAC. This variation might originate from production variations of the ROC-wafers. An indication for this is the fact that ROCs from the same wafer have similar calibration constants. The measurements with 3 lines in zone 2 gives an average slope RMS within wafers of only  $2.8 e^-$ /DAC. Since most modules are built with ROCs from the same wafer, the average slope RMS within modules is also lower, the corresponding value is  $2.9 e^-$ /DAC. Considering all these results, the following use of the calibration constants is suggested: If available, the calibration from the three-line measurement should be used. If no results from a three-line measurement is available, calibration constants averaged over modules (or wafers) should be used.

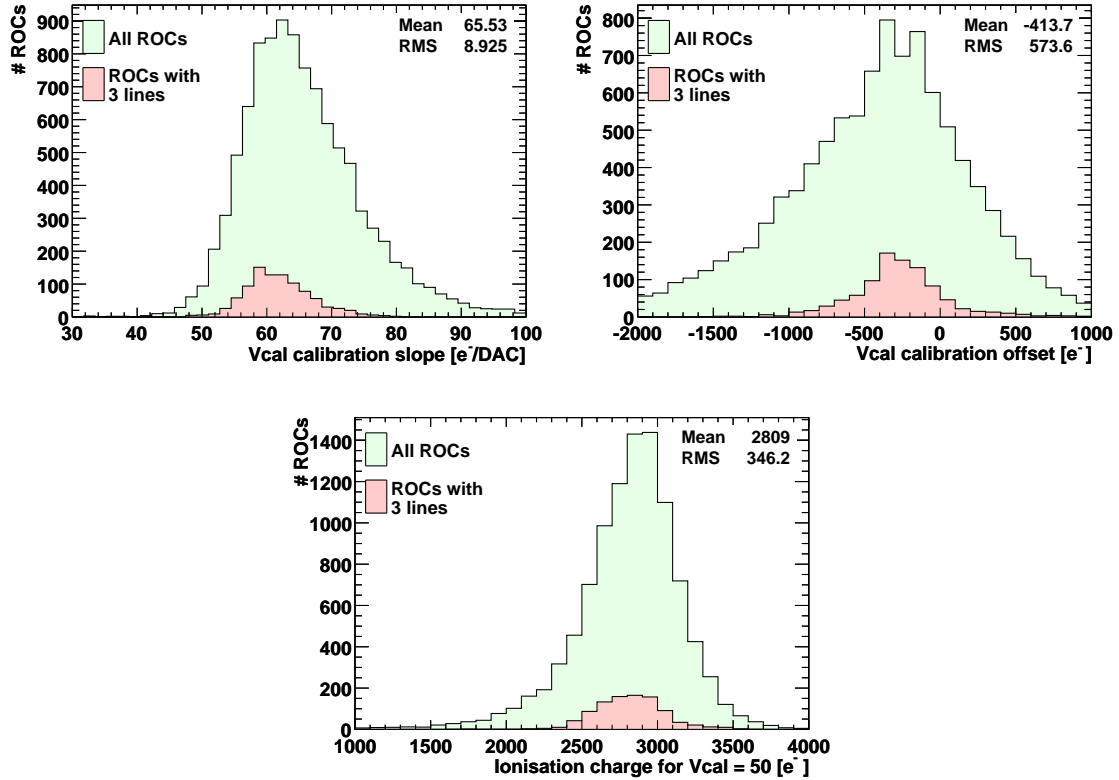


Figure 4.25: Slope (top left) and offset (top right) of the calibration curve  $V_{\text{cal}}$  versus ionisation charge. Also shown is the ionisation charge, which corresponds to a  $V_{\text{cal}}$  value of 50 (bottom). Shown are the results of all ROCs (green histogram) and of those ROCs, which were calibrated with 3 lines (red histogram).

## 4.5 Summary

Many test algorithms have been developed to qualify the detector modules as comprehensively as possible. A lot of time has been invested in the development of the bump bonding test and the trim algorithm. These tests had to be developed from scratch, while for others previous experience could be made use of. Based on the test results, the modules were qualified as described in [17]. Out of 981 assembled modules 806 have passed all the tests, which corresponds to a yield of 82%. After the end of the module tests in March 2008 the detector was assembled and integrated into CMS in July 2008.

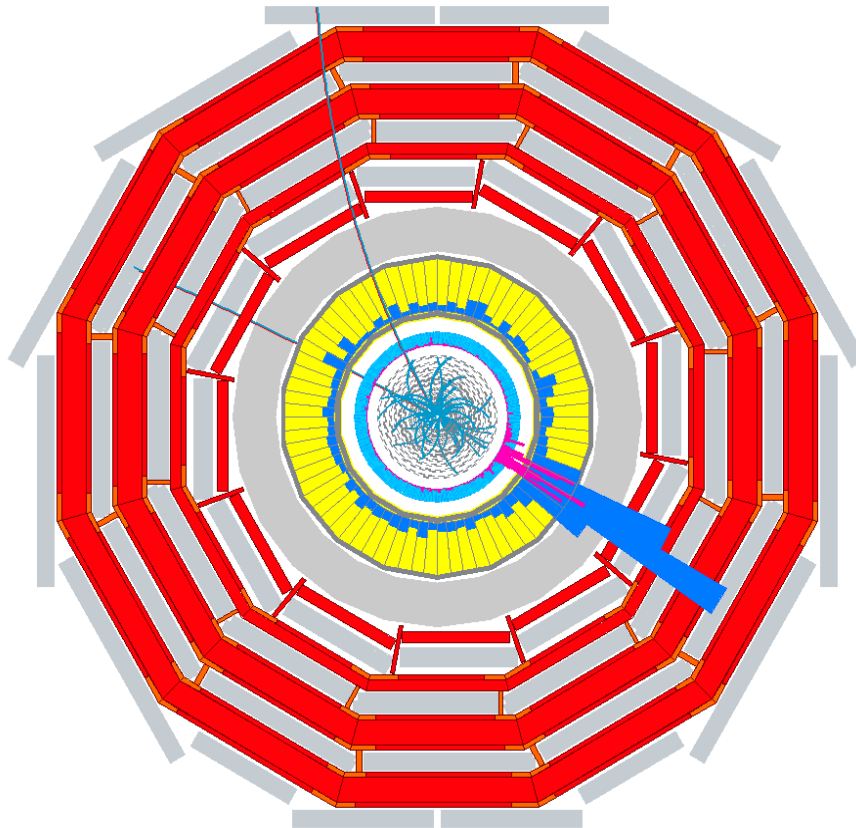
Table 4.7: RMS of the slope distributions for the measurements with 2 lines and 3 lines, after quadratically subtraction of the RMS of the measurement uncertainty. For the measurement with 2 lines in Zone 0, the RMS of the measurement uncertainty was larger than that of the measured distribution.

RMS [ $e^-$ /DAC]	2 lines	3 lines
Zone 0	--	5.1
Zone 1	8.0	5.3
Zone 2	5.6	4.7



# Monte-Carlo Study of a Higgs Search in the Decay

$$H \rightarrow \tau^+ \tau^- \rightarrow \ell^+ \ell^- \cancel{E}_T$$



# Chapter 5

## Higgs Physics

### 5.1 The Higgs Mechanism

Interpreting the massive  $W$  and  $Z$  particles as the gauge bosons of the electroweak  $SU(2)_L \otimes U(1)_Y$  symmetry poses a problem, since gauge bosons in unbroken gauge theories have to be massless. It was found by Peter Higgs and others in 1964 [25, 26, 27, 28, 29] that the combination of the concepts of spontaneous symmetry breaking of a scalar field and nonabelian gauge theories allows for massive gauge bosons. The mechanism, by which this is achieved, is called the Higgs mechanism. In the [SM](#), the electroweak symmetry is broken by an isospin Higgs doublet, which has four degrees of freedom. Three degrees of freedom are absorbed into the longitudinal modes of the  $W$  and  $Z$  bosons, which results in a non vanishing mass for these particles. The elementary particle which is related to the remaining degree of freedom is called the Higgs particle. As a scalar field it has spin zero and its mass is of the order of the electroweak symmetry breaking scale. Theories beyond the [SM](#) may require the introduction of more than one Higgs doublet, which results in more than one observable Higgs particle. Independent of the number of physical Higgs particles, the Higgs mechanism predicts, that the coupling of all elementary particles to the Higgs fields is proportional to their mass. In other words, all elementary particles obtain their mass by their coupling to the Higgs fields.

## 5.2 The Higgs Particle in the Standard Model

### 5.2.1 Properties of the Higgs Boson

#### 5.2.1.1 The Higgs Mass

The only unknown parameter in the Standard Model Higgs sector is the mass of the Higgs boson. Several results from theoretical and experimental side constrain the allowed range for the Higgs mass.

There are two main constraints from the experimental side. First, the searches at [LEP](#) exclude a Higgs mass below 114.4 GeV [3]. Second, a global fit to the electroweak precision data favours a light Higgs boson [30], providing an upper limit on the Higgs mass of 160 GeV at 95% confidence level.

From theoretical side, several effects restrict the Higgs mass (for references see [31], for a collection of predictions and limits for the Higgs mass in various models see [32]). An upper bound results from the requirement, that the cross sections of processes involving longitudinal W and Z bosons, do not violate unitarity. This condition yields  $m_H < 710$  GeV. The requirement, that the quartic Higgs self coupling remains finite, also puts an upper limit on the Higgs mass of 640 GeV. A lower limit of 70 GeV follows from the requirement that the Higgs vacuum is stable.

#### 5.2.1.2 Production Mechanisms

At the LHC there are four dominant production mechanisms for the Higgs particle (see [Figure 5.1](#)). The biggest contribution comes from the gluon fusion mechanism. The coupling of the Higgs particle to the gluons is mediated by a heavy quark loop, with the main contribution from the top quark loop. Another important production mechanism is the Vector Boson Fusion ([VBF](#)) process, where the Higgs particle is produced in association with two light quarks, which fragment into two very forward jets at the opposite ends of the detector. This special event signature is used in many analyses (e.g. [33]) to suppress various background processes. Furthermore, the Higgs particle can be produced together with two heavy quarks, called associated production, or a Z boson, called Higgs bremsstrahlung. [Figure 5.2](#) shows the next-to-leading order ([NLO](#)) production cross sections of these processes at the [LHC](#) as a function of the Higgs mass. For a light Higgs particle the gluon fusion process dominates, followed by [VBF](#). The exact numbers for four Higgs masses between 120 and 135 GeV are given in [Table 5.1](#).

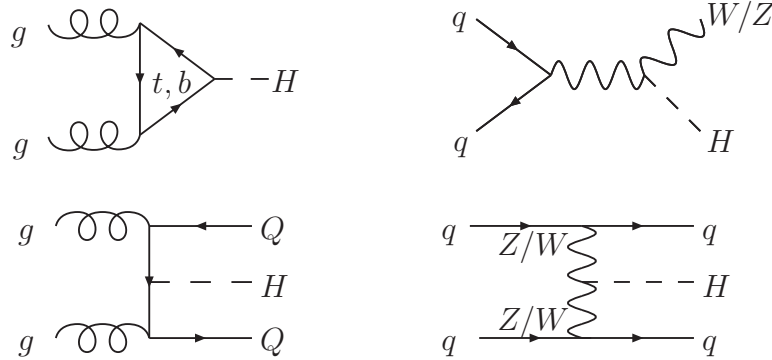


Figure 5.1: The main Higgs production mechanisms at the LHC: gluon fusion (top left), Higgs bremsstrahlung (top right), associated production (bottom left), and vector boson fusion (bottom right).

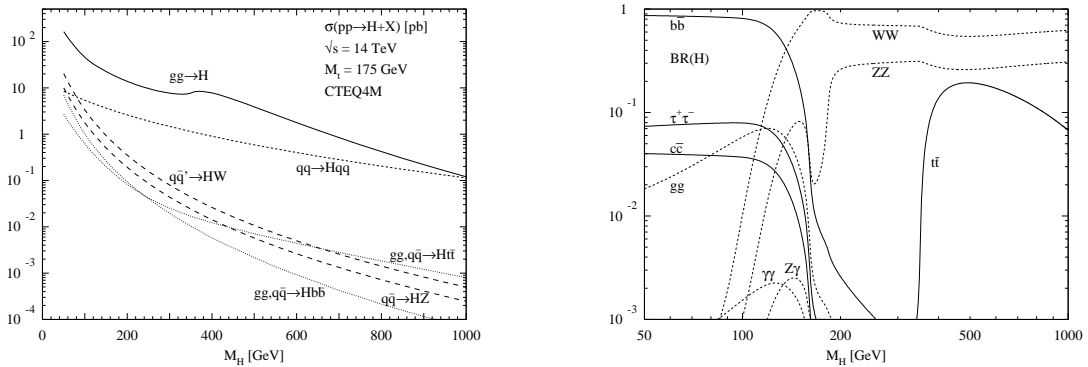


Figure 5.2: SM Higgs production cross sections (left figure) and branching ratios (right figure) at the LHC [34].

### 5.2.1.3 Decay Channels

A light Higgs particle with a mass below 135 GeV decays mainly into beauty quark and tau lepton pairs, as shown in Figure 5.2. Above 100 GeV the decay into two photons opens up too, but only with a very small branching ratio. Above the threshold for  $Z$  and  $W$  pair production, these decays completely dominate all other decay channels. Their dominance is only little diminished by the  $t\bar{t}$  decays above 350 GeV.



Table 5.1: Production cross sections of a SM Higgs boson at the LHC for gluon and vector boson fusion as well as the branching ratio into a tau lepton pair. The numbers have been computed with the programs HIGLU [35], VV2H (which uses the formulae of [36]), and HDECAY [37]. The top mass was set to 172.5 GeV (PDG value 2008).

$m_H$ [GeV]	$\sigma_{\text{gluon}}$ [pb]	$\sigma_{\text{VBF}}$ [pb]	$\mathcal{B}(H \rightarrow \tau^+\tau^-)$
120	36.7	4.43	0.069
125	34.2	4.28	0.063
130	31.9	4.15	0.054
135	29.9	3.96	0.045

### 5.2.2 Higgs Search Strategies at the LHC

The strategies for SM Higgs searches at the LHC strongly depend on the considered Higgs mass range. The decays  $qqH \rightarrow \tau^+\tau^-$  and  $H \rightarrow \gamma\gamma$  are considered the most promising decay channels for an observation of a SM Higgs boson lighter than 135 GeV. The observation of the decay of a Higgs into beauty quarks seems very unlikely, due to the huge QCD background. If the Higgs boson is heavy enough to decay into a  $Z$  boson pair, the observation of four leptons allows for an early discovery. In the intermediate mass range  $m_H \approx 160$  GeV the decay  $H \rightarrow W^+W^- \rightarrow 2\ell 2\nu$  is important. Figure 5.3 shows the discovery potential of the different Higgs searches in the CMS experiment.

## 5.3 The Higgs particles in the Minimal Supersymmetric Standard Model

### 5.3.1 The Higgs Sector in the MSSM

In supersymmetric models, which postulate a symmetry between fermionic and bosonic degrees of freedom [39], at least two isospin Higgs doublets have to be introduced. In the Minimal Supersymmetric Standard Model (MSSM) five physical Higgs bosons remain after electroweak symmetry breaking: two  $CP$ -even neutral, scalar particles  $h$  and  $H$ , one  $CP$ -odd neutral, pseudoscalar particle  $A$  and two charged Higgs bosons  $H^\pm$ . At leading order the MSSM Higgs sector is determined by two parameters, conventionally

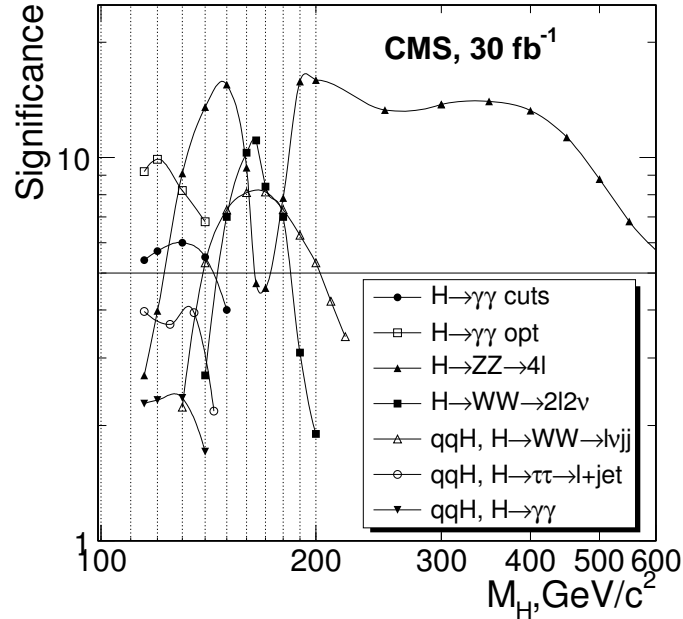


Figure 5.3: SM Higgs discovery potential of the CMS experiment [38].

the pseudoscalar Higgs mass  $m_A$  and  $\tan\beta = v_2/v_1$ , the ratio of the two vacuum expectation values.

### 5.3.2 The Hierarchy Problem

Supersymmetry is able to solve the Hierarchy Problem [40], which occurs if the SM is embedded in Grand Unified Theories (GUT). In these models a light Higgs particle as preferred by the electroweak precision data requires very precise fine tuning, since radiative corrections to the Higgs self-energy push the Higgs mass to the GUT scale of the order  $10^{16}$  GeV. The contributions of the supersymmetric partners to the Higgs self-energy cancel the quadratic divergences of the SM particles, allowing for a Higgs particle with a mass of the electroweak scale.

### 5.3.3 Properties of the Higgs Boson

After including radiative corrections, the upper bound on the light, scalar Higgs particle mass is  $m_h \lesssim 140$  GeV [41]. Like the SM Higgs particle it dominantly decays into beauty

and tau pairs. The closer its mass to the upper bound, the more similar its overall properties to those of the SM Higgs particle. The branching ratio of the heavy, scalar Higgs particle depends strongly on  $\tan\beta$ . For large values, the main decay channels are again those to beauty and tau pairs, while for low values various decay channels are important, depending on the particle's mass. The pseudoscalar Higgs particle  $A$  decays mainly into heavy quark or tau lepton pairs. The relative contributions of the production mechanism also depend on the value of  $\tan\beta$ .

For low values gluon fusion is the dominant production mechanism, while for large values the neutral Higgs particles are mainly produced in association with two beauty quarks, due to the enhanced couplings of the Higgs particle to down-type quarks. The production cross section and branching ratios for the light scalar Higgs boson are shown in Figure 5.4 for some exemplary values of  $\tan\beta$ .

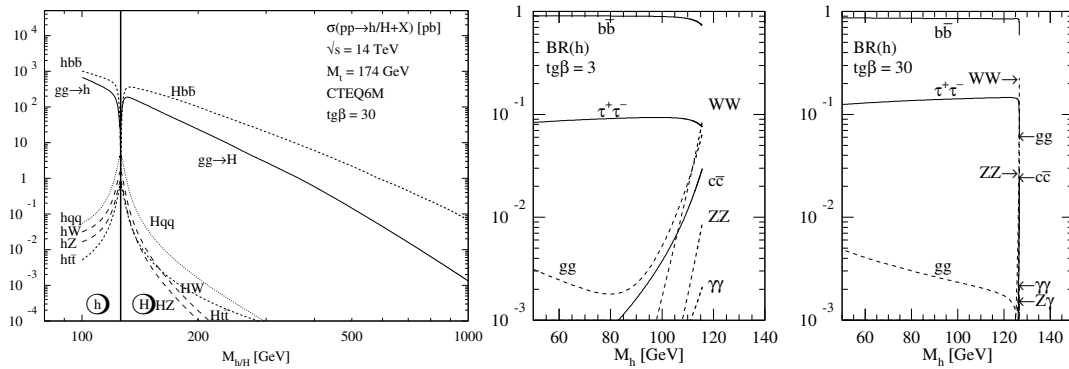


Figure 5.4: Left figure: Production cross sections of the  $CP$ -even MSSM Higgs particles  $h$  and  $H$  for  $\tan\beta = 30$ . Also shown are the branching ratios of the light MSSM Higgs particle  $h$  for  $\tan\beta = 3$  (second figure) and  $\tan\beta = 30$  (third figure) [34].

That which is crooked cannot be made straight: and that which is wanting cannot be numbered.

---

*Ecclesiastes 1, 15*

## Chapter 6

# Search for $H \rightarrow \tau^+ \tau^- \rightarrow \ell^+ \ell^- \cancel{E}_T$

### 6.1 Introduction

The search for a light Higgs boson which decays to a tau lepton pair is intensely investigated in [CMS](#). Based on the different tau decays (see [Table 6.1](#)), different search strategies are possible. In the context of the [SM](#) the decays  $\tau\tau \rightarrow e\mu$  [[42](#)] and  $\tau\tau \rightarrow \ell j$  [[43](#)] are considered ( $j$  stands for a hadronic jet and  $\ell$  for an electron or muon). For a [MSSM](#) Higgs also the decay  $\tau\tau \rightarrow jj$  [[44](#)] is searched for. All these analyses use the two very forward jets present in the [VBF](#) production mechanism to suppress the various backgrounds. This allows for an improved signal-to-background ratio, but also leads to a low signal yield. Based on the work of Ellis et al. [[45](#)], an alternative strategy was elaborated by Mellado et al. [[46](#)]. This chapter presents a detailed study of this approach for the [CMS](#) experiment. The basic idea is to make use of the much larger gluon fusion cross section. Instead of asking for two very forward jets, a balancing high transverse momentum jet is required. A cut on the invariant mass of the reconstructed Higgs particle and this jet is used to suppress the various backgrounds. This approach does not rely on the reconstruction or even  $b$ -tagging of very forward jets, which are non-trivial tasks and might require some time to be well understood.

### 6.2 Backgrounds

The following background processes, which contribute to the final state, are considered:

- $pp \rightarrow Z^0/\gamma^* + X$  with  $Z^0/\gamma^* \rightarrow \mu^+\mu^-/e^+e^-$ . The [PYTHIA](#) [[47](#)] cross section

Table 6.1: Decays of the tau lepton.

Decay	Branching Ratio
$\tau \rightarrow \text{hadrons}$	0.652
$\tau \rightarrow \mu\nu_\mu\nu_\tau$	0.174
$\tau \rightarrow e\nu_e\nu_\tau$	0.174

of this process for  $10 \text{ GeV} < m_{Z^0/\gamma^*} < 80 \text{ GeV}$  is 12.3 nb (c.f. [48, 49]). This background can be heavily reduced by requesting substantial  $\cancel{E}_T$  in the event.

- $pp \rightarrow Z^0/\gamma^* + X$  with  $Z^0/\gamma^* \rightarrow \tau^+\tau^-$  and  $\tau \rightarrow \ell\nu_\ell\nu_\tau$ . This background is irreducible and very difficult to suppress. Its PYTHIA cross section for  $m_{Z^0/\gamma^*} > 50 \text{ GeV}$  is 0.206 nb. It can be reduced most effectively by requiring a large invariant mass of the tau lepton pair and the leading jet.
- $pp \rightarrow t\bar{t} + X$  with  $t \rightarrow Wb$  and  $W \rightarrow e\nu_e, \mu\nu_\mu, \tau\nu_\tau$ . The NLO cross section of this process (including the branching ratio  $W \rightarrow \ell\nu_\ell$ ) is about 85 pb [50, 51]. This background can be suppressed by requiring that there are no  $b$ -tagged jets in the event and by an upper limit on the number of high transverse momentum jets in the central region.
- $pp \rightarrow W^+W^- + X$  with  $W \rightarrow e\nu_e, \mu\nu_\mu, \tau\nu_\tau$ . The NLO cross section of this process (including the branching ratio  $W \rightarrow \ell\nu_\ell$ ) is about 12.3 pb [52]. This process contributes only little compared to the other backgrounds.

## 6.3 Simulation

All steps of the Monte-Carlo (MC) study (event generation, detector simulation, digitisation, reconstruction) are done within the official CMS software framework (CMSSW) versions CMSSW\_1\_6\_7 and CMSSW\_1\_6\_12. The MC event generation is done with PYTHIA, version 6.409 [53]. A Higgs mass of 120 GeV was chosen. No pile-up is added to the generated events. The number of generated events as well as the PYTHIA physics processes and cross sections are shown in Table 6.2. To save CPU time and disk storage, the simulation was not performed for all generated events but only for those which

contain a lepton pair with the leptons not being back-to-back in the transverse plane. In addition to these preselected, high-statistics event samples, smaller samples without any preselection were used, e.g. to determine the efficiencies of the preselection or mass cuts (see below).

Table 6.2: PYTHIA processes (MSUB), cross sections  $\sigma$ , and number of generated events of the different signal and background channels ( $\ell = e/\mu$ , neutrinos omitted). The Higgs mass was set to 120 GeV.

Channel	PYTHIA process	$\sigma$ [pb]	Generated events
$H \rightarrow \tau^+\tau^- \rightarrow \ell^+\ell^-$	120	0.36	138600
$qqH \rightarrow \tau^+\tau^- \rightarrow \ell^+\ell^-$	123, 124	0.043	75400
$t\bar{t} (W \rightarrow \tau/\mu/e)$	81, 82	85	2208000
$Z^0/\gamma^* \rightarrow \ell^+\ell^-$	1	12300	38940000
$Z^0/\gamma^* \rightarrow \tau^+\tau^- \rightarrow \ell^+\ell^-$	1	206	4244000
$W^+W^- (W \rightarrow \tau/\mu/e)$	25	12.3	498000

The interactions of the generated particles with the detector are simulated using a GEANT4 [54] description of the full detector [11]. Afterwards the digitisation step simulates the detector response to the deposited energy in the detector.

## 6.4 Event Reconstruction

Most physics objects are reconstructed using the default CMSSW reconstruction algorithms as described in [11].

### 6.4.1 Muons

In CMS muons are reconstructed in three stages. In a first step, muons are reconstructed locally by matching hits within the muon chambers to form track segments. In the next step, the segments of the different muon systems are combined and fit to get a first estimate of the muon track. Such a “stand alone muon” is finally matched with tracks in the silicon tracker to get the final “global muon” track [11]. The performance

of this global muon reconstruction is shown in Figure 6.1. The charge-misidentification probability lies below 0.1% for muons with transverse momentum below 100 GeV.

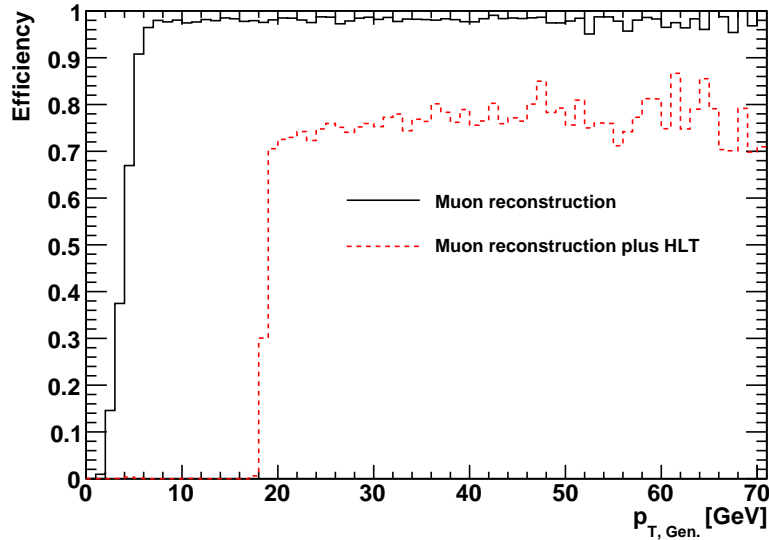


Figure 6.1: Muon reconstruction and HLT efficiencies for the signal events  $H \rightarrow \tau^+\tau^- \rightarrow \mu^+\mu^-$ . The solid line shows the probability of a muon to be reconstructed as a global muon. The dashed line shows the efficiency with the additional requirement, that this muon also triggers the single, isolated muon HLT path.

### 6.4.2 Electrons

The reconstruction of electrons is significantly more difficult than for muons. Electrons traversing the silicon tracker radiate bremsstrahlung photons, which in turn may convert into electron-positron pairs. The reconstruction algorithm has to be able to cope with these effects. The standard electron reconstruction starts with a supercluster in the ECAL [55]. Its position is used to predict the electron hits in the pixel detector, at a place where the electron has not yet lost a lot of its energy by radiation. The matched pixel hits then seed the track finding in the whole tracker to find the electron track. To reduce the number of fake electrons from light quark jets, an additional step called electron identification [11] is applied. This step improves the purity of the

reconstructed electrons based on several variables. In the used [CMSSW](#) version, the user can choose between “tight” and “loose” cuts. In this analysis the “loose” electron identification is used, in order to keep as many signal events as possible. The two sets of cuts use the same cut variables like the shape of the supercluster and the matching between the reconstructed electron track and the cluster in the [ECAL](#). Compared to the “loose” cuts, the “tight” selection uses tighter cut values to decrease the electron fake rate at the cost of a lower efficiency. Figure 6.2 shows the electron reconstruction efficiency with and without “loose” electron identification.

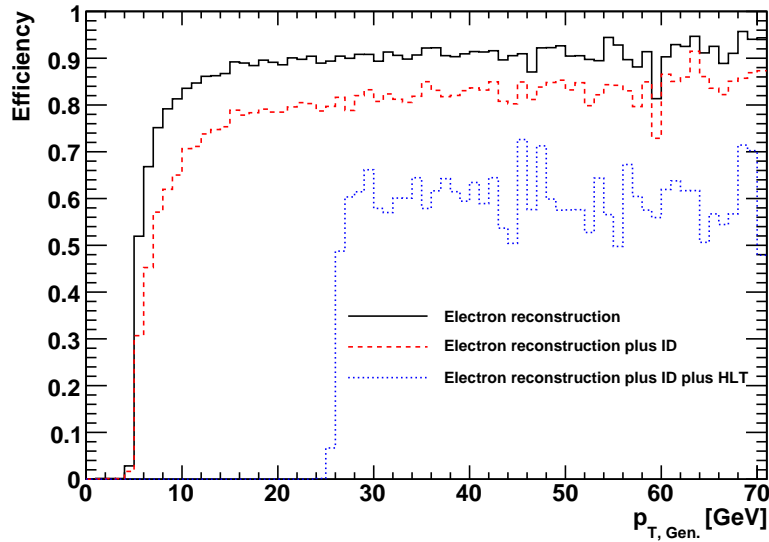


Figure 6.2: Electron reconstruction efficiency, with (dashed line) and without electron identification (solid line), for the signal events  $H \rightarrow \tau^+\tau^- \rightarrow e^+e^-$ . The dotted line also includes the requirement, that the electron triggers the isolated, single electron HLT path.

### 6.4.3 Jets

Jets are reconstructed using the iterative cone jet algorithm with a cone size of  $R = 0.5$  [56]. This algorithm iteratively reconstructs jets from the calorimeter clusters within the cone size  $R$ . In the first iteration the algorithm is seeded by the calorimeter



cluster with the highest transverse energy, later on by the jets reconstructed in the previous iteration. The reconstruction of a jet stops if its energy is stable within 1% and its direction within  $\Delta R < 0.01$ . After the reconstruction an  $\eta$  and  $E_T$  dependent jet energy calibration is applied to the reconstructed jets to restore the correct particle-level energy. The necessary calibration constants are obtained from MC samples. The jet energy resolution after this correction is shown in Figure 6.3. The resolution is still around 18% for central jets with  $E_T = 50$  GeV.

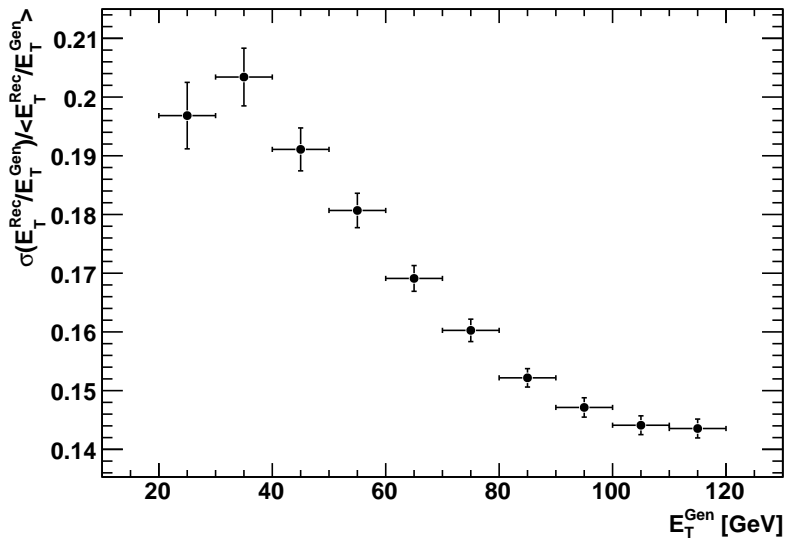


Figure 6.3: The jet transverse energy resolution for the iterative cone algorithm after Monte-Carlo jet energy calibration for  $t\bar{t}$  events.

#### 6.4.4 $b$ -Tagging

Several  $b$ -tagging algorithms are exploited in CMS. In CMSSW\_1.6.7, the Jet Probability algorithm [57] gives the best performance and is therefore used in this analysis. In a first step, for each of the  $N$  tracks the probability of originating from the primary vertex is computed. In a second step, it is calculated how likely it is, that  $N$  tracks from the primary vertex would produce the observed, or any less likely values of the track probabilities. If this probability is low, the jet is likely to be a  $b$ -jet.

### 6.4.5 The Collinear Approximation

The Higgs momentum can be reconstructed from the measured lepton<sup>1</sup> momenta and the missing transverse energy if it is assumed that the flight direction of the leptons is parallel to that of their mother tau particles [45], i.e.

$$\vec{p}_{\ell,i} = x_i \cdot \vec{p}_{\tau,i} \quad (0 < x_i < 1, i = 1, 2). \quad (6.1)$$

In the relativistic limit ( $m_{\tau,i} \ll |\vec{p}_{\tau,i}|$  and  $m_{\ell,i} \ll |\vec{p}_{\ell,i}|$ ), it follows that

$$p_{\ell,i} = x_i \cdot p_{\tau,i}, \quad (6.2)$$

which gives the following formula for the Higgs mass

$$m_H^2 = m_{\tau\tau}^2 = \left( \frac{p_{\ell,1}}{x_1} + \frac{p_{\ell,2}}{x_2} \right)^2, \quad (6.3)$$

where  $m_{\tau\tau}$  is the invariant mass of the tau leptons<sup>2</sup>. The scale factors  $x_i$  can be computed from the momenta in the transverse plane (see Figure 6.4):

$$p_T(H) = p_T(\tau_1) + p_T(\tau_2) = \frac{p_T(\ell_1)}{x_1} + \frac{p_T(\ell_2)}{x_2} \quad (6.4)$$

$$= p_T(\ell_1) + p_T(\ell_2) + \cancel{E}_T, \quad (6.5)$$

since  $\cancel{E}_T = \cancel{p}_T$  for massless neutrinos. This can be solved for the  $x_i$

$$x_1 = \frac{\Delta}{p_x(H)p_y(\ell_2) - p_x(\ell_2)p_y(H)} \quad (6.6)$$

$$x_2 = \frac{\Delta}{p_y(H)p_x(\ell_1) - p_y(\ell_1)p_x(H)}, \quad (6.7)$$

<sup>1</sup>To simplify the language, the electron or muons originating from the tau decays are often summarised as “the leptons”. If the tau particles or the neutrinos should be referred to, this will be clear from the context.

<sup>2</sup>Assuming  $m_{\ell,i} \equiv 0$ , the formula simplifies to  $m_H = m_{\ell\ell}/\sqrt{x_1x_2}$ , with  $m_{\ell\ell}$  the invariant mass of the two leptons.

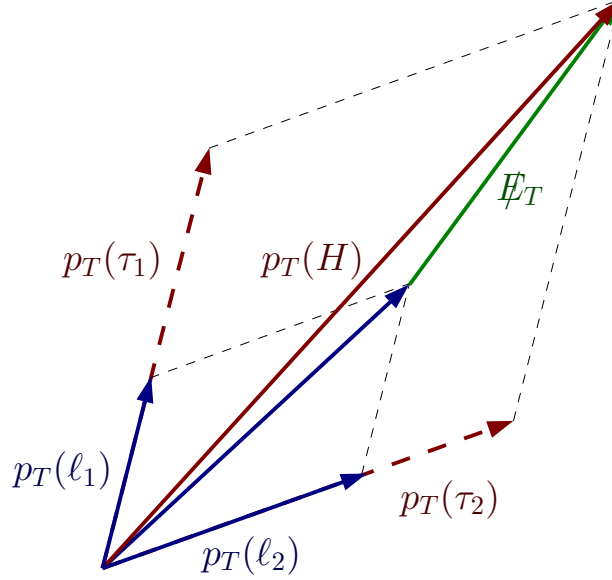


Figure 6.4: Reconstruction of the Higgs momentum.

where

$$\Delta = p_x(\ell_1)p_y(\ell_2) - p_y(\ell_1)p_x(\ell_2) \quad (6.8)$$

$$p_{x,y}(H) = p_{x,y}(\ell_1) + p_{x,y}(\ell_2) + p_{x,y}(\cancel{E}_T). \quad (6.9)$$

The described method breaks down if the two leptons are back-to-back in the transverse plane. In this case, the Higgs transverse momentum cannot be split between the two tau particles in an unique way. For angles  $\Delta\phi_{\ell\ell}$  close to  $\pi$ , a small error in the  $\cancel{E}_T$  determination results in a large error of the tau momenta and therefore of the Higgs mass. The error of the reconstructed Higgs mass due to the collinear approximation (6.1) is very small for Higgs particles produced with large transverse momentum. The Higgs mass resolution is completely dominated by the imprecision of the  $\cancel{E}_T$  measurement as shown in Figure 6.5. The figure shows the Higgs mass distributions after the preselection cuts (see below) computed from reconstructed objects only, from reconstructed objects but with the tau directions from generator level, and from reconstructed objects

but with the  $\cancel{E}_T$  taken from generator level.

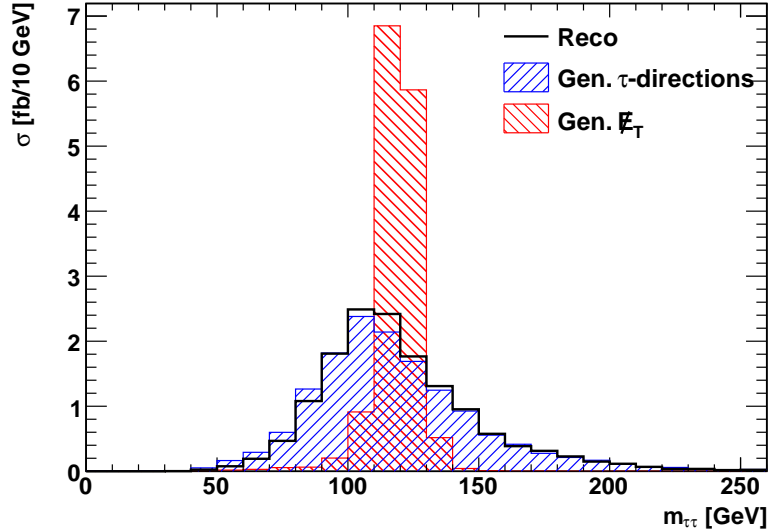


Figure 6.5: Test of the collinear approximation. The black line shows the Higgs mass distribution after the preselection cuts computed from reconstructed objects only. The blue, right hatched distribution shows the Higgs mass distribution with the tau directions taken from generator level, the red, left hatched one with the  $\cancel{E}_T$  from generator level.

### 6.4.6 Missing Transverse Energy

**CMS** was designed to cover as much as solid angle as possible with calorimetry, to determine precisely the transverse energy balance. For events without muons and neutrinos, the summed transverse energy measured by an ideal detector would be zero. In reality there will always be some missing transverse energy due to several effects. In **CMS** these are for example the finite pseudorapidity coverage of the calorimeter or the strong magnetic field which prevents charged, low transverse momentum particles to reach the calorimeter. The dominant contribution is supposed to come from the calorimeter resolution.

The reconstruction of the missing transverse energy is the crucial point for the success of this analysis, since its (im-)precision determines the width of the observed

Higgs signal peak. The worse the  $\cancel{E}_T$ -resolution, the broader the Higgs peak and the smaller its significance. The situation is even worse, because the high mass tail of the  $Z^0$ -peak constitutes the main background in the Higgs signal region. Therefore, a poor  $\cancel{E}_T$ -resolution not only increases the width of the Higgs mass peak, but also adds additional background to this region by broadening the  $Z^0$ -peak.

The  $\cancel{E}_T$ -reconstruction usually starts from the vectorial sum of the transverse energy of all calorimeter towers [58]. This sum is called raw or uncorrected  $\cancel{E}_T$ . Several corrections are applied to this value. First of all, the sum has to be corrected for the transverse energy of the muons. Muons deposit on average 2 GeV of energy in the calorimeter as shown in Figure 6.6. This energy is determined by summing up the energy of the calorimeter cells, which were crossed by the muon. Up to this small energy deposition, the muon energy is missing in the calculation of the missing transverse energy. Therefore, the measured transverse muon energy reduced by the energy deposition in the calorimeter has to be subtracted from the raw  $\cancel{E}_T$ . The  $\cancel{E}_T$  value after this correction is called Type-0  $\cancel{E}_T$ .

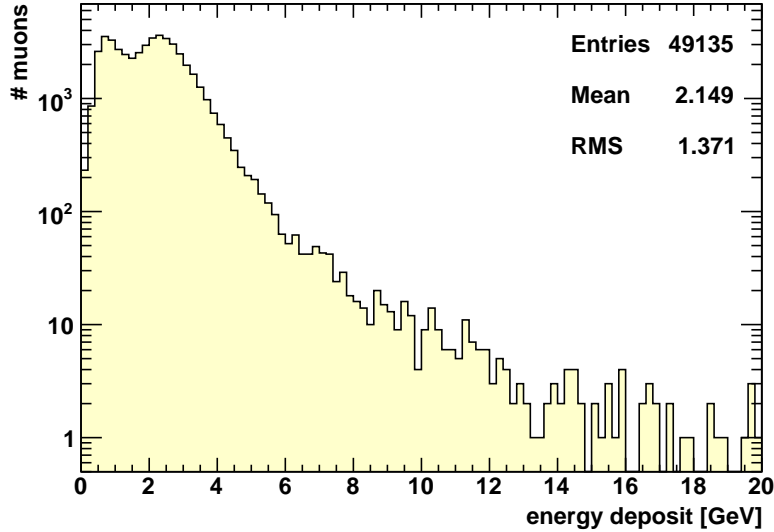


Figure 6.6: Energy deposit of all muons in  $H \rightarrow \tau^+\tau^- \rightarrow \ell^+\ell^-$  events in the calorimeter. The first peak originates from the muons traversing the barrel calorimeters, the second peak from the muons traversing the endcap calorimeters.

Another correctable error of the  $\cancel{E}_T$  determination comes from the mismeasurement of the jet energies. Due to detector effects, the measured jet energy tends to be smaller than its actual value. On average, the correct jet energy can be restored with the help of MC corrections. For each group of calorimeter towers forming a jet, the measured transverse energy is replaced with the corrected jet energy. The  $\cancel{E}_T$  value obtained in this way is called Type-1  $\cancel{E}_T$ . Figure 6.7 shows a comparison of the  $\cancel{E}_T$  resolution of Type-0 and Type-1  $\cancel{E}_T$  for  $t\bar{t}$  events. The Type-1  $\cancel{E}_T$  restores the missing transverse energy scale and tends to have slightly better resolution.

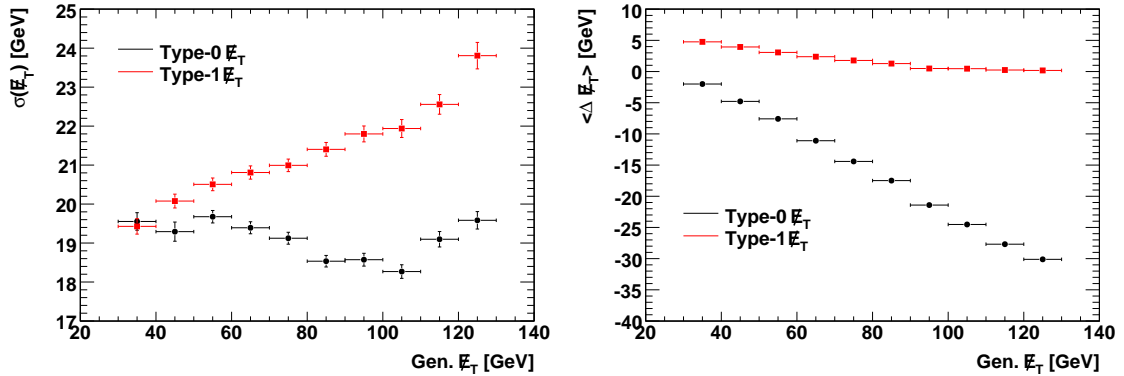


Figure 6.7: Missing transverse energy resolution (left figure) and scale error (right figure) of the  $t\bar{t}$  sample.

This method to correct the Type-0  $\cancel{E}_T$  has the disadvantage to rely on the correct simulation of the jet interaction with the calorimeter. A better and more reliable way to extract a  $\cancel{E}_T$  calibration from data is to use decays of the  $Z^0$  boson into two leptons. This has the advantages, that there is no dependency on a correct detector simulation and that the calibration can be obtained for the specific event topology under investigation. The  $Z^0/\gamma^* \rightarrow \ell^+\ell^-$  events are identical to  $Z^0/\gamma^* \rightarrow \tau^+\tau^- \rightarrow \ell^+\ell^-$  events up to the fact, that the former do not have intrinsic  $\cancel{E}_T$  from neutrinos and that the lepton energies are higher. The absence of any physical  $\cancel{E}_T$  allows to determine the  $\cancel{E}_T$  originating from detector effects. From this knowledge a correction can be extracted which can be applied to  $Z^0/\gamma^* \rightarrow \tau^+\tau^-$  events.

As stated above, a large part of the  $\cancel{E}_T$  correction comes from the mismeasurement of the jet energies. Therefore the natural choice for the variable, as a function of which

the  $\cancel{E}_T$  correction is extracted, is the transverse energy of the leading jet in the event. To include the information about the direction of the  $\cancel{E}_T$  correction, not the absolute value of the Type-0  $\cancel{E}_T$ , but its projection onto the leading jet direction is considered. It is found that the calibration curve strongly depends on the pseudorapidity of the leading jet. Therefore, the calibration is determined for different pseudorapidity regions. For each region the Type-0  $\cancel{E}_T$  projection onto the leading jet direction is fitted with a polynomial of second degree. Figure 6.8 shows the calibration curves obtained from  $Z^0/\gamma^* \rightarrow e^+e^-$  and  $Z^0/\gamma^* \rightarrow \mu^+\mu^-$  events. The corrected  $\cancel{E}_T$  value is then given by

$$\vec{\cancel{E}}_{T,Corr} = \vec{\cancel{E}}_{T,0} - f_{\ell\ell}(E_{T,LJ}, \eta_{LJ}) \frac{\vec{p}_{T,LJ}}{|\vec{p}_{T,LJ}|} \quad (6.10)$$

where  $f_{\ell\ell}(E_{T,LJ}, \eta_{LJ})$  is the  $\cancel{E}_T$  correction obtained from Figure 6.8, depending on the transverse energy and the pseudorapidity of the leading jet, as well as on the flavour of the two leptons ( $\ell = e/\mu$ ). If the leptons are of different flavour, the  $\cancel{E}_T$  correction is obtained by averaging the corrections from  $Z^0/\gamma^* \rightarrow e^+e^-$  and  $Z^0/\gamma^* \rightarrow \mu^+\mu^-$  events:  $f_{e\mu} = 0.5 \cdot (f_{ee} + f_{\mu\mu})$ .

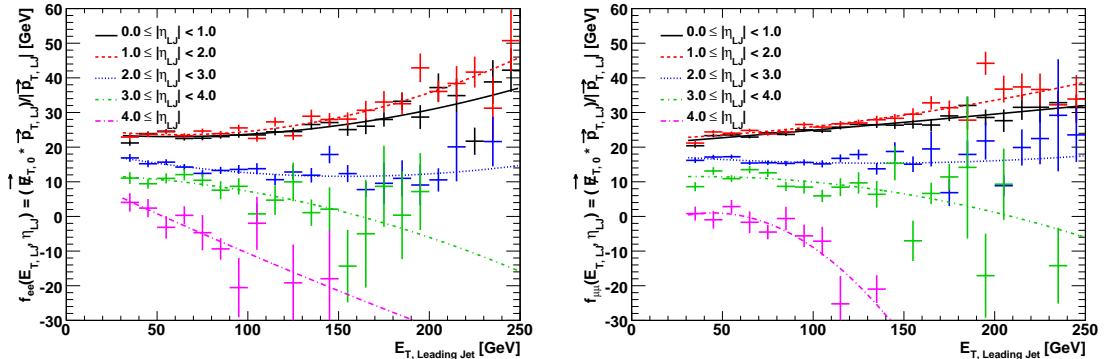


Figure 6.8: Calibration curves for the  $\cancel{E}_T$  correction extracted from  $Z^0/\gamma^* \rightarrow e^+e^-$  (left figure) and  $Z^0/\gamma^* \rightarrow \mu^+\mu^-$  events (right figure). Shown is the projection of the Type-0  $\cancel{E}_T$  onto the leading jet direction in the transverse plane as a function of transverse energy of the leading jet. The calibration is measured for five different pseudorapidity regions.

To check whether the  $\cancel{E}_T$  calibration can be used for  $H$  decays too, these events are compared to  $Z^0/\gamma^* \rightarrow \tau^+\tau^-$  events in Figure 6.9. The required  $\cancel{E}_T$  correction

determined from generator level information is plotted as a function of the transverse energy and the pseudorapidity of the leading jet. The agreement between  $Z^0$  and  $H$  decays is good over the whole range of the leading jet transverse energy averaged over the leading jet pseudorapidity. But it is found, that the Higgs decays would require a somewhat larger correction if the leading jet is very central. This is due to the fact, that the jets in these events originate mainly from gluons, while the jets in  $Z^0/\gamma^*$  events are mainly light quark jets. Since these events will not be used anyway, this is not a severe problem.

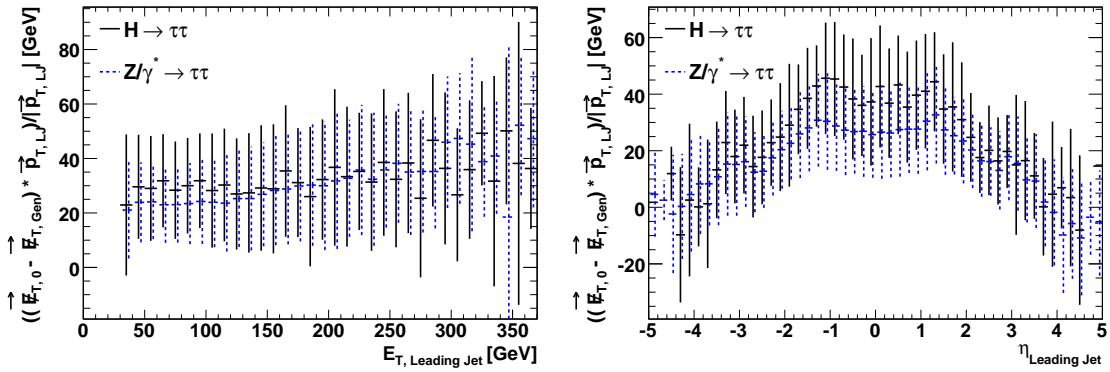


Figure 6.9: Comparison of the required  $\cancel{E}_T$  correction for  $Z^0/\gamma^*$  and  $H$  decays. The profiles show the mean and RMS (indicated by the size of the error bars) of the required  $\cancel{E}_T$  correction as a function of the transverse energy (left figure) and the pseudorapidity (right figure) of the leading jet. The profiles of the  $Z^0/\gamma^*$ -channel were plotted with a small offset to make the error bars visible.

The data driven  $\cancel{E}_T$  correction is compared to the Type-1  $\cancel{E}_T$  correction in Figure 6.10. The  $\cancel{E}_T$  correction from  $Z^0 \rightarrow \ell^+\ell^-$  events performs better in terms of the  $\cancel{E}_T$  resolution as well as in terms of the Higgs mass resolution. The  $\cancel{E}_T$  correction from data provides a narrower mass peak and recovers the correct  $Z^0$  mass.



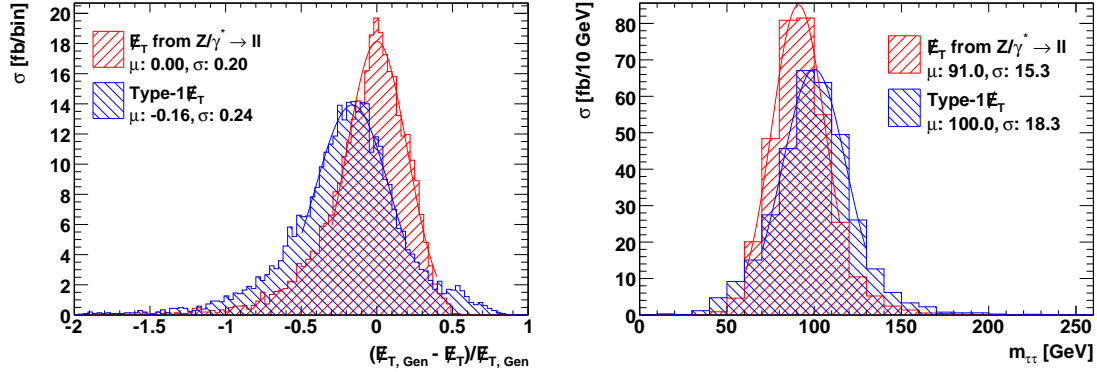


Figure 6.10: Comparison of the Type-1  $\cancel{E}_T$  with the  $\cancel{E}_T$  correction extracted from  $Z^0/\gamma^* \rightarrow \ell^+\ell^-$  events. The left plot compares the  $\cancel{E}_T$ -resolution, the right plot the invariant  $\tau^+\tau^-$  mass resolution for the decays  $Z^0/\gamma^* \rightarrow \tau^+\tau^- \rightarrow \ell^+\ell^-$ . In the legend,  $\mu$  is the mean and  $\sigma$  the width of a fitted Gaussian function.

## 6.5 Event Selection

### 6.5.1 Online Selection

At the [HLT](#) the events of interest are most effectively triggered by the isolated electron and muon paths. The transverse momentum thresholds of the four paths used in this analysis are shown in Table 6.3. Table 6.4 shows the trigger efficiencies for the two signal channels separated for the four trigger paths. At the time, when the trigger menu for an instantaneous luminosity of  $2 \cdot 10^{33} \text{ cm}^{-2}\text{s}^{-1}$  was compiled, no electron plus muon or lepton plus jet triggers were foreseen. In the meantime such triggers have been implemented, but their thresholds for the mentioned luminosity are not yet known. This analysis will certainly benefit from the inclusion of these trigger channels.

### 6.5.2 Offline Selection

#### 6.5.2.1 Lepton Selection

Out of all reconstructed muons and electrons, only those which pass some quality criteria are considered. The criteria on the muons are the following

- $|\eta_\mu| < 2.5$

Table 6.3: Trigger thresholds of the isolated lepton paths for an instantaneous luminosity of  $2 \cdot 10^{33} \text{ cm}^{-2}\text{s}^{-1}$ .

HLT path	$p_T$ threshold [ GeV ]
$\mu$	19
$\mu\mu$	7
$e$	26
$ee$	12

Table 6.4: HLT efficiencies for the signal samples  $(qq)H \rightarrow \tau^+\tau^- \rightarrow \ell^+\ell^- (\ell = e/\mu)$  separated for the four isolated lepton paths. The total efficiency does not correspond to the sum of the four HLT paths, since some events are triggered by more than one trigger path.

	$\mu$	$\mu\mu$	$e$	$ee$	total
$H$	0.22	$7.5 \cdot 10^{-2}$	0.14	$3.8 \cdot 10^{-2}$	0.38
$qqH$	0.26	$8.0 \cdot 10^{-2}$	0.18	$4.3 \cdot 10^{-2}$	0.45

- Good fit of the global muon track ( $\chi^2/NDF < 3$ )
- Isolation:  $\frac{\Sigma_{tracks} p_T}{p_{T,\mu}} < 0.4$  for all tracks with  $p_T > 1.5 \text{ GeV}$  in a cone  $0.015 < \Delta R < 0.5$  around the muon

The selection criteria are the same for the electrons, except for a looser cut on the electron track quality ( $\chi^2/NDF < 10$ ) and the requirement that the electron passes the “loose” electron identification [11]. This additional step is necessary to reduce the number of fake electrons, especially in  $t\bar{t}$  events. Together with the higher HLT thresholds, this causes the selection efficiency for electron decays to be smaller than for muon decays.

An event is accepted if two leptons of opposite charge satisfying all these criteria are found. If more than two leptons remain, for each sign of the charge the lepton with the highest transverse momentum is selected. For the gluon fusion Higgs production the correct leptons (i.e. those originating from the taus of the Higgs decay) were selected

in 27786 out of 27940 events. For the vector boson fusion 17237 out of 17408 events have the correct leptons selected.

### 6.5.2.2 Preselection Cuts

In this step a first group of selection criteria is applied on the events which have passed the [HLT](#). The first obvious requirement is the presence of a lepton pair as described above. A successful reconstruction of the tau momenta requires that the scale factors  $x_i$  meet the condition  $0 < x_i < 1, i = 1, 2$ . Furthermore, the event is required to have a jet with a transverse energy exceeding 30 GeV. The  $Z^0/\gamma^* \rightarrow \ell^+\ell^-$  background can be efficiently suppressed by the following cuts. Events are required to have a missing transverse energy larger than 30 GeV, a  $\cancel{E}_T$ -significance<sup>1</sup> above  $2.5\sqrt{\text{GeV}}$ , and an invariant lepton mass in the range  $18 \text{ GeV} < m_{\ell\ell} < 75 \text{ GeV}$ . Since the Higgs mass resolution is very poor if the leptons are back-to-back in the transverse plane, only events with  $\Delta\phi_{\ell\ell} < 2.7$  are kept. To reduce the  $t\bar{t}$  background a  $b$ -jet veto is applied. The  $b$ -tagging discriminator is set to 0.50, which efficiently removes the  $t\bar{t}$  background without losing too many signal events. Table [6.5](#) gives an overview of the different cuts and their efficiencies. The distributions of the corresponding quantities before the cuts are applied, are shown in [A.1](#).

---

<sup>1</sup>Since the  $\cancel{E}_T$  resolution scales as  $\sqrt{\Sigma E_T}$ , the  $\cancel{E}_T$ -significance of an event is defined as  $\cancel{E}_T/\sqrt{\Sigma E_T}$ .  $\Sigma E_T$  is the scalar sum of the transverse energy of all calorimeter hits and muons.

Table 6.5: Efficiencies of the preselection cuts.

	$H$	$qqH$	$Z^0/\gamma^* \rightarrow \tau^+\tau^-$	$Z^0/\gamma^* \rightarrow \ell^+\ell^-$	$t\bar{t}$	$W^+W^-$
HLT	0.38	0.45	0.11	0.15	0.48	0.47
Good lepton pair	0.53	0.52	0.50	0.68	0.41	0.37
$0 < x_i < 1$	0.65	0.76	0.59	0.37	0.23	0.14
$E_{T,LJ} > 30 \text{ GeV}$	0.62	0.97	0.44	0.24	0.99	0.58
$\cancel{E}_T > 30 \text{ GeV}$	0.69	0.81	0.56	0.13	0.82	0.66
$\cancel{E}_T/\sqrt{\Sigma E_T} > 2.5\sqrt{\text{GeV}}$	0.76	0.79	0.73	0.46	0.74	0.73
$18 \text{ GeV} < m_{\ell\ell} < 75 \text{ GeV}$	0.95	0.95	0.96	0.88	0.37	0.44
$\Delta\phi_{\ell\ell} < 2.7$	0.81	0.91	0.75	0.50	0.76	0.67
No $b$ -jets	0.88	0.90	0.90	1.0	0.34	0.91
Total	$2.9 \cdot 10^{-2}$	$8.5 \cdot 10^{-2}$	$3.9 \cdot 10^{-3}$	$2.4 \cdot 10^{-4}$	$2.5 \cdot 10^{-3}$	$1.9 \cdot 10^{-3}$

Table 6.6: Efficiencies of the significance cuts.

	$H$	$qqH$	$Z^0/\gamma^* \rightarrow \tau^+\tau^-$	$Z^0/\gamma^* \rightarrow \ell^+\ell^-$	$t\bar{t}$	$W^+W^-$
$p_{T,H} > 100 \text{ GeV}$	0.75	0.82	0.47	0.13	0.79	0.80
$E_{T,LJ} > 60 \text{ GeV}$	0.99	0.99	0.99	0.90	0.98	0.99
$ \eta_{LJ}  > 1.6$	0.43	0.64	0.25	0.44	0.33	0.25
$m_{H,LJ} > 500 \text{ GeV}$	0.63	0.70	0.26	0.25	0.58	0.52
Only one central jet	0.74	0.78	0.70	1.0	0.23	0.32
Total	0.15	0.28	$2.1 \cdot 10^{-2}$	$1.3 \cdot 10^{-2}$	$3.4 \cdot 10^{-2}$	$3.3 \cdot 10^{-2}$

### 6.5.2.3 Mass Resolution Cuts

After the preselection cuts the Higgs mass resolution is still large, but can be improved by another set of cuts. The most effective way to do this, is to tighten the cut on  $\Delta\phi$  between the two leptons. Furthermore, cuts on the minimal transverse momentum of the two leptons, the product of the scale factors  $x_i$ , and the pseudorapidity difference of the two leptons slightly improve the mass resolution. The effect of these cuts on the mass peak is shown in Figure 6.11. Their efficiencies for the different channels are given in Table 6.7. To determine the efficiencies of these cuts, the small statistics samples without any preselection were used. This explains why some efficiencies are identical to one.

Table 6.7: Efficiencies of the mass resolution cuts.

	$H$	$qqH$	$Z^0/\gamma^* \rightarrow \tau^+\tau^-$	$Z^0/\gamma^* \rightarrow \ell^+\ell^-$	$t\bar{t}$	$W^+W^-$
$p_{T,\ell 2} > 7 \text{ GeV}$	0.89	0.90	0.86	1.0	0.90	0.85
$\Delta\phi_{\ell\ell} < 2.0$	0.58	0.73	0.46	0.29	0.50	0.49
$\Delta\eta_{\ell\ell} < 1.6$	0.90	0.93	0.91	1.0	0.98	0.85
$x_1x_2 > 0.03$	0.99	0.98	1.0	1.0	0.93	0.91
Total	0.46	0.60	0.36	0.29	0.41	0.32

### 6.5.2.4 Significance Cuts

To increase the significance of the signal, additional cuts are applied. Since the background from  $Z^0/\gamma^* \rightarrow \tau^+\tau^-$  events is very similar to the signal, it is very difficult to reduce this background without losing too many signal events. First the transverse momentum of the reconstructed Higgs boson is required to lie above 100 GeV. Furthermore the leading jet is required to have substantial transverse energy and must not be very central. The most important cut requires that the invariant mass of the Higgs particle and the leading jet is larger than 500 GeV. The  $t\bar{t}$  background can be further reduced by an upper limit on the number of jets with  $E_T > 30 \text{ GeV}$  in the central region ( $|\eta| < 2.6$ ). The cut efficiencies are given in Table 6.6. The final invariant  $\tau^+\tau^-$  mass distribution is shown in Figure 6.12 and the cross sections after all cuts are listed in Table 6.8. Furthermore, Table 6.9 shows the contributions of the different final states

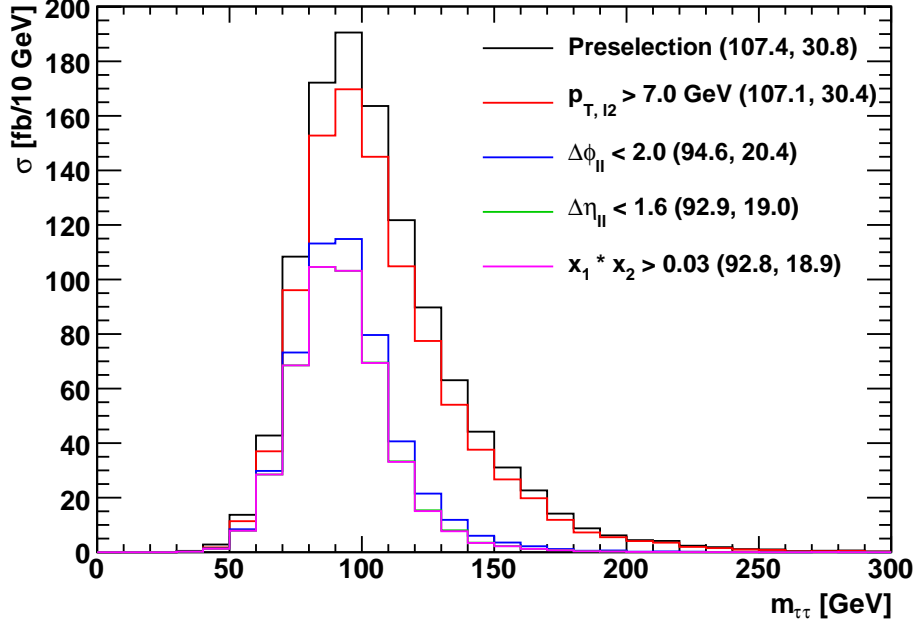


Figure 6.11: Effect of the mass resolution cuts on the  $Z^0$ -peak. The numbers in parentheses are the mean and the RMS of the distributions.

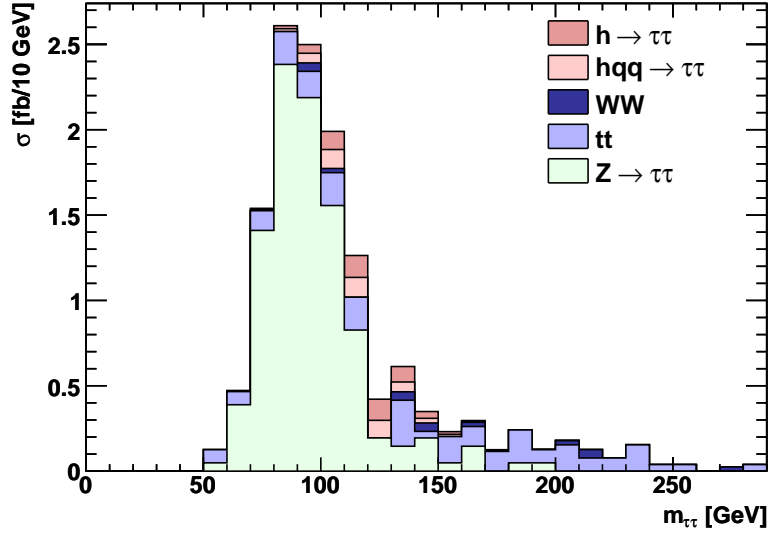
to the gluon fusion signal cross section.

Table 6.8: Cross sections of the different channels after all cuts.

	$H$	$qqH$	$Z^0/\gamma^* \rightarrow \tau^+\tau^-$	$Z^0/\gamma^* \rightarrow \ell^+\ell^-$	$t\bar{t}$	$W^+W^-$
$\sigma$ [fb]	0.600	0.524	9.63	0.316	2.54	0.296

Table 6.9: Contributions of the different final states to the gluon fusion signal cross section after all cuts.

	$\mu\mu$	$e\mu$	$ee$
$\sigma$ [fb]	0.190	0.281	0.128

Figure 6.12: Final distribution of the invariant  $\tau^+\tau^-$  mass.

### 6.5.2.5 Cut Optimisation

Each cut was optimised by determining the signal significance after all cuts as a function of the cut value, while keeping the other cut values fixed. The signal significance was computed with the two methods as described in section 6.7. The cut values were set to a value, for which both methods yield a good signal significance. Regions with large fluctuations of the significance (e.g. due to small statistics) were avoided. The results of the optimisation are shown in the appendix, see A.2.

## 6.6 Fitting of the Invariant $\tau^+\tau^-$ Mass Distribution

### 6.6.1 The Signal Distribution

After adding up the two signal contributions, the invariant  $\tau^+\tau^-$  mass is fitted with a Gaussian function. The fit reproduces the distribution quite well up to a small tail at high masses as shown in Figure 6.13. To keep the fit procedure simple, this small correction is neglected. It turns out that the reconstructed Higgs mass value is too small. This deviation originates from the imprecision of the  $\cancel{E}_T$  measurement (using

the  $\cancel{E}_T$  reconstructed at generator level restores the Higgs mass to its input value). The two main reasons for the too small reconstructed Higgs mass are the whole series of event selection cuts, which favours events with underestimated missing energy, and the  $\cancel{E}_T$  calibration which does not account for the differences between  $Z^0$  and  $H$  decays as discussed above.

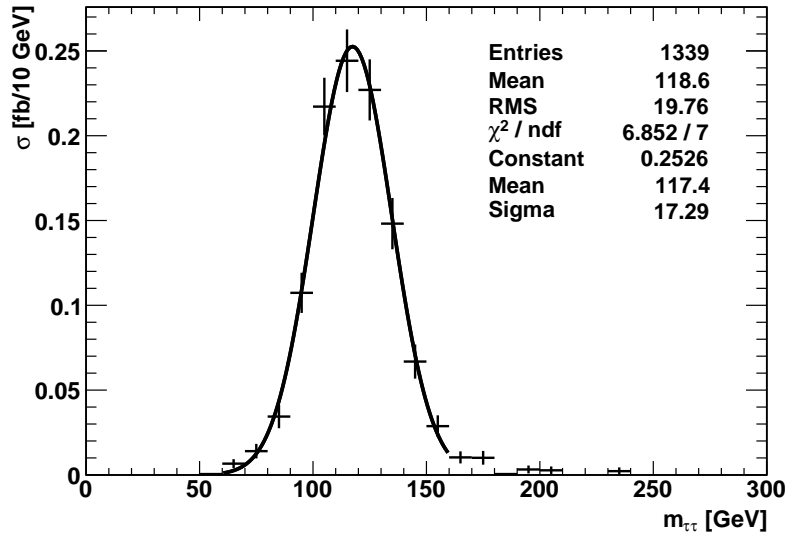


Figure 6.13: Gaussian fit to the signal invariant  $\tau^+\tau^-$  mass distribution after all cuts.

## 6.6.2 The $Z^0/\gamma^* \rightarrow \tau^+\tau^-$ Background

### 6.6.2.1 Measuring the Invariant Mass Shape of $Z^0/\gamma^* \rightarrow \tau^+\tau^-$ from $Z^0/\gamma^* \rightarrow \ell^+\ell^-$ Data

An exact knowledge of the  $Z^0/\gamma^*$  mass distribution is crucial for the successful extraction of the signal contribution. Once again, the availability of a pure  $Z^0/\gamma^* \rightarrow \ell^+\ell^-$  sample proves to be very useful. After a simple conversion of the leptons into tau particles, it reproduces very well the  $Z^0/\gamma^* \rightarrow \tau^+\tau^-$  background and can be used to determine the shape of the  $Z^0/\gamma^*$  peak from data.

The conversion of the leptons into taus is performed as follows. First, the distribution of the lepton momentum fraction  $x$  is determined with the help of Monte-Carlo



$Z^0/\gamma^* \rightarrow \tau^+\tau^- \rightarrow \ell^+\ell^-$  events without applying any cuts. This distribution fitted with a polynomial of third degree is shown in Figure 6.14. For both leptons of each  $Z^0/\gamma^* \rightarrow \ell^+\ell^-$  event, a random number according to this distribution is computed and the lepton momentum is scaled accordingly. The corresponding neutrino energies are added to the missing transverse energy. Out of all converted events, only those which would pass the HLT, are kept. Figure 6.15 shows a comparison of a converted  $Z^0/\gamma^* \rightarrow \mu^+\mu^-$  sample with real  $Z^0/\gamma^* \rightarrow \tau^+\tau^- \rightarrow \mu^+\mu^-$  events after a cut of 10 GeV on the transverse momentum of the lower transverse momentum muon. This cut is necessary because the CMS muon reconstruction only reaches its full efficiency above this value (see Figure 6.1), for electrons the corresponding value is about 14 GeV. As shown in Figure 6.15 the converted  $Z^0/\gamma^* \rightarrow \mu^+\mu^-$  sample reproduces the  $Z^0/\gamma^* \rightarrow \tau^+\tau^- \rightarrow \mu^+\mu^-$  background with good precision. The largest discrepancy between the two samples in the low transverse momentum distributions of the leptons will be treated as systematic error. An alternative approach, which uses the lepton momentum fraction  $x$  after the online selection, was also investigated. Using this distribution for rescaling the tau momenta results in a much worse agreement between the two samples. This is due to correlations between the scaling factors and the tau momenta after the online selection. To correctly take into account these effect a much more complicated procedure with tau momentum and decay channel dependent scaling factor distributions would be required.

### 6.6.2.2 Fitting of the $Z^0/\gamma^* \rightarrow \tau^+\tau^-$ Background

In contrast to the signal distribution, it is important to correctly take into account the tails of the invariant  $\tau^+\tau^-$  mass distribution of the  $Z^0/\gamma^* \rightarrow \tau^+\tau^-$  background. These tails constitute to a large degree the background in the Higgs mass region. Therefore two Gaussian functions are used to fit the  $Z^0$ -peak. Figure 6.16 shows the fit of the  $Z^0$ -peak, using the converted  $Z^0/\gamma^* \rightarrow \ell^+\ell^-$  sample. In order to have sufficient statistics in the tails of the distribution, the cut on the invariant mass of the Higgs particle and the leading jet was relaxed to 400 GeV. Also shown is a fit to the invariant  $\tau^+\tau^-$  mass distribution of the  $Z^0/\gamma^* \rightarrow \tau^+\tau^-$  sample after all cuts with the shape obtained from the  $Z^0/\gamma^* \rightarrow \ell^+\ell^-$  sample.

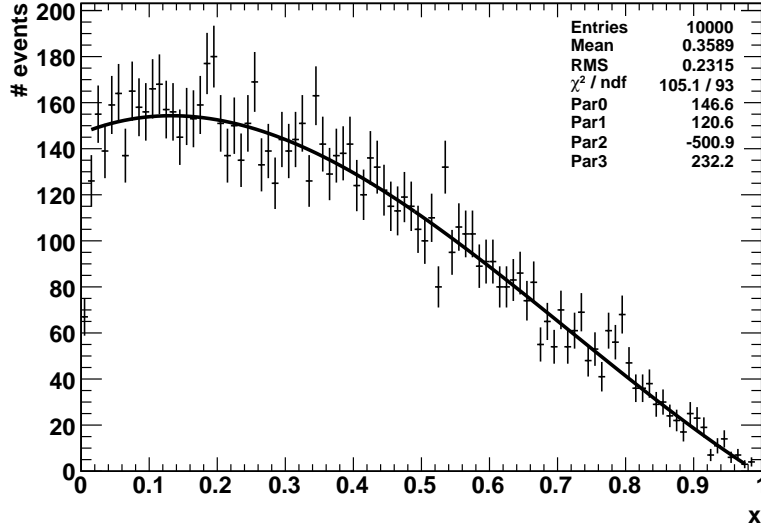


Figure 6.14: Distribution of the lepton momentum fraction  $x$  determined from a MC sample of  $Z^0/\gamma^* \rightarrow \mu^+\mu^-$  events fitted with a polynomial of third degree.

### 6.6.3 The $Z^0/\gamma^* \rightarrow \ell^+\ell^-$ Background

After all cuts only one event, corresponding to a cross section of 0.316 fb is left, which is small compared to the other backgrounds, see Table 6.8. Therefore this background is neglected in the fit procedure.

### 6.6.4 The $t\bar{t}$ and $W^+W^-$ Backgrounds

With the help of the converted  $Z^0/\gamma^* \rightarrow \ell^+\ell^-$  sample it is possible to determine the shape of these backgrounds from data too. In order to have a sample dominated by  $Z^0/\gamma^* \rightarrow \tau^+\tau^-$  and  $t\bar{t}$  events, all analysis cuts are applied with the exception of the b-jet veto and the cut on the number of central jets. The invariant  $\tau^+\tau^-$  mass distribution can be fitted with two Gaussian functions for the  $Z^0/\gamma^*$  contribution and a polynomial of 3rd degree for the  $t\bar{t}$  and the  $W^+W^-$  contributions. Since the  $Z^0/\gamma^*$  shape is known from the  $Z^0/\gamma^* \rightarrow \ell^+\ell^-$  sample, only the number of  $Z^0/\gamma^*$  events and the polynomial are allowed to vary. From the performed fit, the known  $Z^0/\gamma^*$  contribution is subtracted and the  $t\bar{t}$  and  $W^+W^-$  contributions remain. Figure 6.17

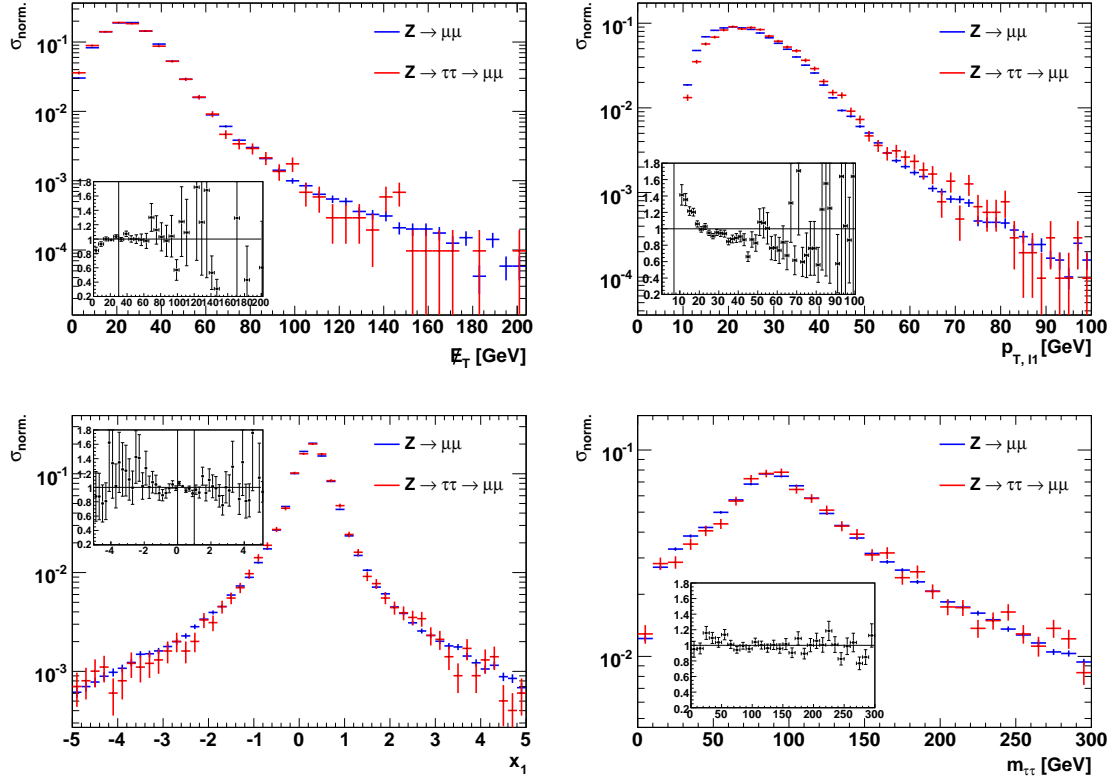


Figure 6.15: Validation of the conversion of  $Z^0/\gamma^* \rightarrow \mu^+\mu^-$  events into  $Z^0/\gamma^* \rightarrow \tau^+\tau^- \rightarrow \mu^+\mu^-$  events. Shown are the normalised distributions of the missing transverse energy (top left), the transverse momentum of the highest  $p_T$  muon (top right), the reconstructed lepton energy fraction  $x_1$  (bottom left), and the invariant  $\tau^+\tau^-$  mass (bottom right) for the converted sample as well as the actual  $Z^0 \rightarrow \tau^+\tau^-$  sample. The insets show the ratio between the two samples.

illustrates this procedure. It shows the invariant  $\tau^+\tau^-$  mass distribution after all cuts except the b-jet veto and the cut on the number of central jets (black histogram) and the fit to this distribution (black line). The red, dashed line shows the fit after subtraction of the  $Z^0/\gamma^*$  contribution, the red histogram the actual  $t\bar{t}$  and  $W^+W^-$  distribution. To test, whether this procedure works, the  $t\bar{t}$  and  $W^+W^-$  shape after all cuts is fitted with the shape obtained in this way. The corresponding fit with the number of events as free parameter works well, with a  $\chi^2/NDF$  of 11.7/20.

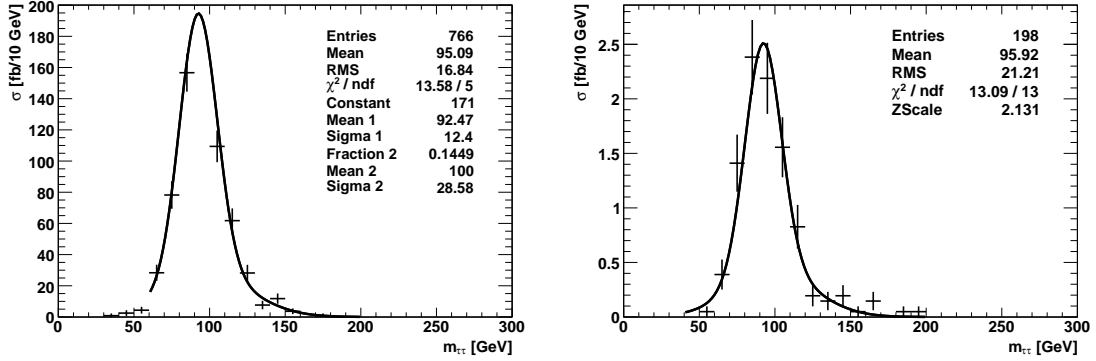


Figure 6.16: Determination of the invariant  $\tau^+\tau^-$  mass distribution of the  $Z^0/\gamma^*$  background. Left figure: Fit of two Gaussian functions to the invariant  $\tau^+\tau^-$  mass distribution of the converted  $Z^0/\gamma^* \rightarrow \ell^+\ell^-$  sample. Right figure: Fit of the invariant  $\tau^+\tau^-$  mass distribution of the  $Z^0/\gamma^* \rightarrow \tau^+\tau^- \rightarrow \ell^+\ell^-$  sample after all cuts with the same shape.

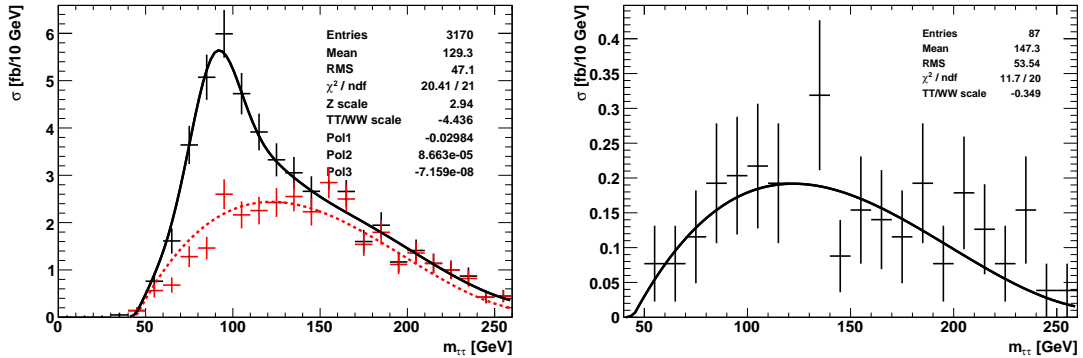


Figure 6.17: Determination of the invariant  $\tau^+\tau^-$  mass distribution of the  $t\bar{t}$  and  $W^+W^-$  backgrounds. Left figure: Fit of the invariant  $\tau^+\tau^-$  mass distribution with relaxed cuts (black histogram). Shown are the actual fit (black line) as well as the fit after subtraction of the  $Z^0/\gamma^*$ -contribution (red, dashed line), reproducing well the  $t\bar{t}$  and  $W^+W^-$  contribution (red histogram). Right figure: Fit of the invariant  $\tau^+\tau^-$  mass distribution of the  $t\bar{t}$  and  $W^+W^-$  backgrounds after all cuts with the same shape.

### 6.6.5 The Combined Fit

The final invariant  $\tau^+\tau^-$  mass distribution is fitted with the sum of the functions described above. These are a Gaussian for the signal, two Gaussians for the  $Z^0/\gamma^* \rightarrow \tau^+\tau^-$  background and a polynomial of 3rd degree for the  $t\bar{t}$  and  $W^+W^-$  backgrounds with a total of 13 parameters. In order to successfully determine all parameters, their values have to be properly initialised and their allowed ranges have to be restricted. The corresponding values are shown in Table 6.10. An example of the combined fit to a toy-experiment for an integrated luminosity of  $30 \text{ fb}^{-1}$  is shown in Figure 6.18.

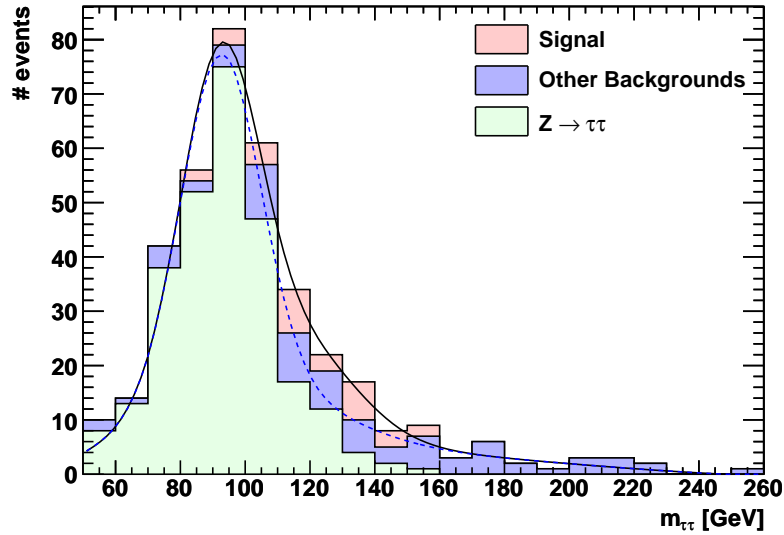


Figure 6.18: Combined fit to the invariant  $\tau^+\tau^-$  mass distribution of a toy-experiment for an integrated luminosity of  $30 \text{ fb}^{-1}$ . The solid line shows the actual fit, while the dashed line shows the background distribution as extracted from the fit.

The  $Z^0/\gamma^*$  shape is determined from the fit to the converted  $Z^0/\gamma^* \rightarrow \ell^+\ell^-$  sample. The accuracy with which this shape can be determined, is obtained by a fit to a toy-experiment with statistics corresponding to an integrated luminosity of  $30 \text{ fb}^{-1}$ . In the combined fit, the corresponding fit parameters are allowed to vary within these errors. The amount of  $Z^0/\gamma^* \rightarrow \tau^+\tau^-$  events can be estimated in the following way. By relaxing the cut on the invariant mass of the Higgs particle and the leading jet, a sample dominated by  $Z^0/\gamma^* \rightarrow \tau^+\tau^-$  is obtained, from which the number of  $Z^0/\gamma^* \rightarrow$

$\tau^+\tau^-$  events can be inferred. The efficiency of the last step is again determined with the help of the converted  $Z^0/\gamma^* \rightarrow \ell^+\ell^-$  sample. The statistical uncertainty of this procedure is about 5%. The shape of the  $t\bar{t}$  plus  $W^+W^-$  distribution is determined as described above. Again the shape uncertainty is obtained by a toy-experiment corresponding to an integrated luminosity of  $30 \text{ fb}^{-1}$ . The scale of this background can be determined from the high invariant  $\tau^+\tau^-$  mass tail and is allowed to vary within 20% in the fit. The Higgs mass is allowed to vary between 105 GeV and 135 GeV. The signal width is assumed to be known from Monte-Carlo studies or from the width of the  $Z^0$  peak and is restricted to 14.0 GeV up to 18.0 GeV. The signal scale is restricted to twice the expected SM cross section.

Table 6.10: Initial values and limits for the 13 parameters of the combined fit.

	initial value	lower limit	upper limit
Signal Scale	7.58	0.0	15.2
Signal Mean	117	105	135
Signal Sigma	17.3	14.0	18.0
$Z^0/\gamma^*$ Scale	63.9	60.7	67
$Z^0/\gamma^*$ Mean 1	92.3	92.1	92.4
$Z^0/\gamma^*$ Sigma 1	12.0	11.7	12.2
$Z^0/\gamma^*$ Fraction 2	0.185	0.168	0.202
$Z^0/\gamma^*$ Mean 2	98.7	97.3	100
$Z^0/\gamma^*$ Sigma 2	27.4	26.8	28.1
$t\bar{t}/W^+W^-$ Scale	-10.5	-12.6	-8.38
$t\bar{t}/W^+W^-$ Pol1	$-2.98 \cdot 10^{-2}$	$-3.01 \cdot 10^{-2}$	$-2.95 \cdot 10^{-2}$
$t\bar{t}/W^+W^-$ Pol2	$8.82 \cdot 10^{-5}$	$8.66 \cdot 10^{-5}$	$8.98 \cdot 10^{-5}$
$t\bar{t}/W^+W^-$ Pol3	$-7.42 \cdot 10^{-8}$	$-7.63 \cdot 10^{-8}$	$-7.22 \cdot 10^{-8}$

## 6.7 Significance Estimation

### 6.7.1 Event Counting

The significance  $\sigma$  of an observed signal can be estimated from the number of signal ( $s$ ) and background ( $b$ ) events by means of  $\sigma_{\text{est}} = s/\sqrt{s+b}$ . The numbers of signal and background events are extracted from the combined fit in the signal region  $[\mu-\sigma, \mu+2\sigma]$ , where  $\mu$  is the mean of the signal Gaussian and  $\sigma$  its width (the signal region was fixed based on the optimisation shown in Figure 6.19).  $10^4$  toy-experiments have been generated and for each its significance  $\sigma_{\text{est}}$  was computed. This was done for two cases: the null-hypothesis with no signal contribution present and the signal-hypothesis with a contribution of a SM Higgs boson of 120 GeV mass. The results are shown in Figure 6.20. To avoid any bias from the fit procedure on the significance estimator  $\sigma_{\text{est}}$ , the expected significance  $\sigma_{\text{exp}}$  is calculated from  $N_b$ , the number of background only toy-experiments with an estimated significance above the mean  $\sigma_{\text{est}}$  value of the signal toy-experiments:

$$\sigma_{\text{exp}} = \sqrt{2} \cdot \text{erf}^{-1}(N_b), \quad (6.11)$$

where  $\text{erf}^{-1}$  is the *inverse error function*. The expected significance for an observed signal are given in Table 6.11 for four different Higgs masses.

### 6.7.2 Likelihood-Ratio Estimation

An alternative way to test the hypothesis of the presence of a SM Higgs boson contribution is the use of the Likelihood-Ratio technique as used for the Higgs searches at LEP [3]. This technique checks the compatibility of an observed invariant mass distribution with the expected distributions for the signal- and the null-hypothesis. The Likelihood-Ratio is given by

$$Q = \frac{\prod_{i=1}^n f_s(x_i)}{\prod_{i=1}^n f_b(x_i)} \quad (6.12)$$

where  $n$  is the number of events and  $f_s(x)$  and  $f_b(x)$  are the normalised invariant mass distributions for the signal- and the null-hypothesis. Figure 6.21 shows the distribution of the estimator  $-2\ln(Q)$  for  $10^4$  toy-experiments, again for the cases with and

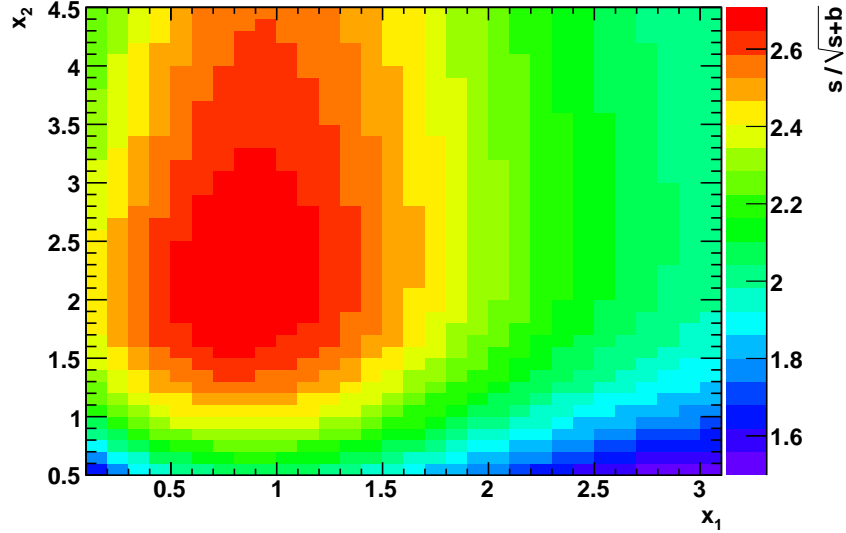


Figure 6.19: Optimisation of the signal region  $[\mu - x_1\sigma, \mu + x_2\sigma]$  used to determine the number of signal and background events ( $\mu$  is the mean of the signal Gaussian and  $\sigma$  its width). The plot shows the average signal significance  $\sigma_{\text{est}} = s/\sqrt{s+b}$  of 1000 toy-experiments.

without a signal contribution. The expected significance  $\sigma$  is given by the separation of the two distributions. Concretely

$$\sigma = \frac{\mu_{bkg} - \mu_{sig}}{\sigma_{bkg}} \quad (6.13)$$

where  $\mu_{bkg}(\mu_{sig})$  is the mean of the background only (background plus signal) distribution and  $\sigma_{bkg}$  the standard deviation of the background only distribution. All these quantities are determined by fitting a Gaussian function to the corresponding distributions. Table 6.11 shows the expected significance for four different Higgs masses.

The Likelihood-Ratio technique as described above requires the knowledge of the Higgs mass. Since this is not a priori known, the significance for a signal has to be determined for different mass hypotheses. The significance will have its maximum near the Higgs mass as shown in Figure 6.22.



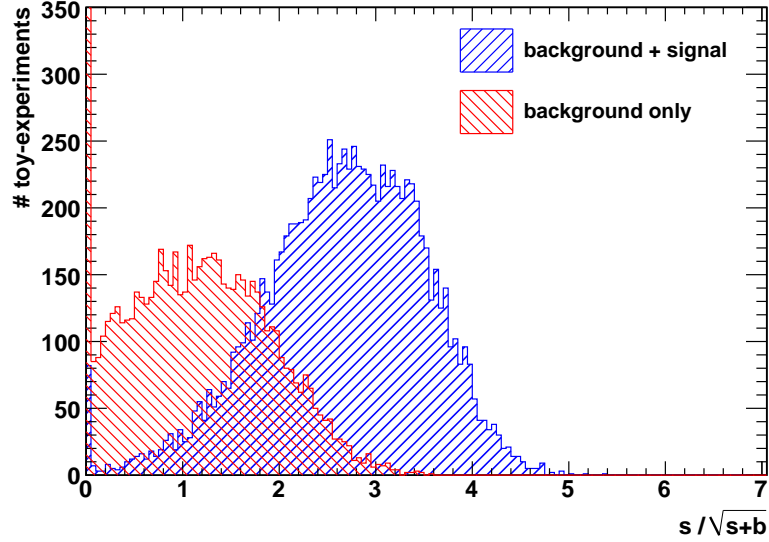


Figure 6.20: Distributions of the significance of  $10^4$  toy-experiments. In one case no signal component was present in the invariant  $\tau^+\tau^-$  mass distribution, in the other case the signal of a 120 GeV Higgs boson was added to the background distribution.

Table 6.11: Expected significance of a SM Higgs boson signal for four different Higgs masses.  $\sigma_{ec}$  is the significance estimated from the event counting method,  $\sigma_{lh}$  the one estimated from the Likelihood-Ratio.

$m_H$ [GeV]	$\sigma_{ec}$	$\sigma_{lh}$
120	2.4	2.2
125	2.4	2.3
130	2.2	2.2
135	1.9	2.0

## 6.8 Systematics

According to [38] two kinds of systematic errors have to be distinguished. The first group of uncertainties are those, which influence the ability to predict the average expected significance, but whose effects can be determined from data. The following

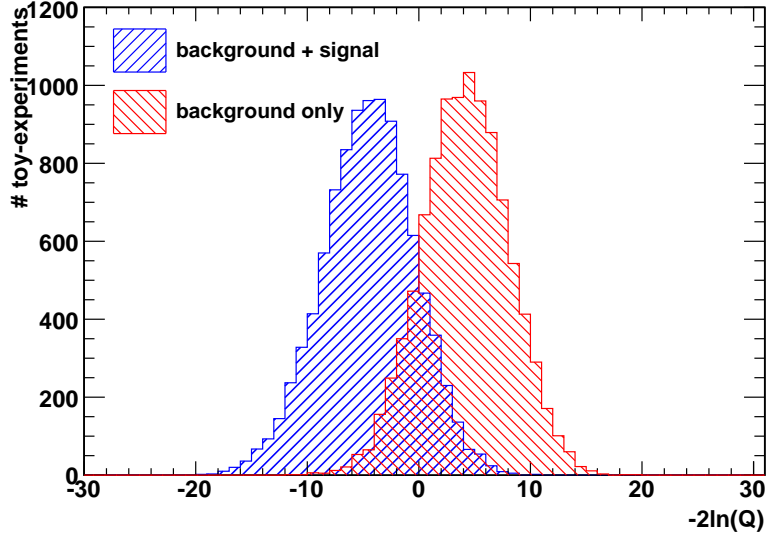


Figure 6.21: Distributions of the Likelihood-Ratio estimator for  $10^4$  toy-experiments. In one case no signal component was present in the invariant  $\tau^+\tau^-$  mass distribution, in the other case the signal of a 120 GeV Higgs boson was added to the background distribution.

uncertainties fall into this category.

The sensitivity of the analysis to variations of the overall  $\cancel{E}_T$  scale is reduced due to the  $\cancel{E}_T$  calibration from data. A variation of the  $\cancel{E}_T$  scale by  $\pm 10\%$  results in a variation of the signal significance of 0.17.

The analysis is robust against a possibly higher fraction of fake leptons, since they contribute only very little to the total number of events. Their contribution was estimated from the  $t\bar{t}$  sample, which also includes hadronically decaying taus, which might be misidentified as electrons. After having applied the preselection cuts, only 9‰ of the events include fake electrons and 2‰ of the events include fake muons. Compared to other systematic uncertainties like the uncertainty of the  $b$ -tagging efficiency, this effect is negligibly small.

A misaligned detector will increase the number of  $t\bar{t}$  events by deteriorating the  $b$ -tagging efficiency. According to [11], the  $b$ -tagging efficiency of 0.42 could decrease to 0.37 for a misaligned detector at a constant mistagging rate for non  $b$ -jets. In

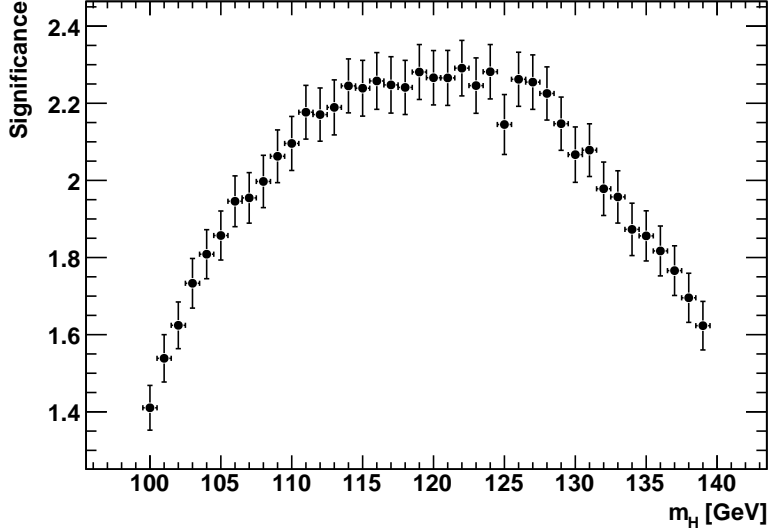


Figure 6.22: Likelihood-Ratio significance for the presence of a Higgs boson for different mass hypotheses. The significance peaks around the reconstructed Higgs mass of 117 GeV. The error bars show the statistical uncertainty from 1000 toy-experiments.

consequence of this, the number of  $t\bar{t}$  events would increase by 15%.

The factorisation and renormalisation scale uncertainties of the signal cross sections are very different for the two considered production mechanism. For gluon fusion the uncertainty is around 25%, while for the VBF it is only 2%. PDF uncertainties are around 4% for both production mechanism. The theoretical uncertainty of the branching ratio  $H \rightarrow \tau^+\tau^-$  is about 5% [31].

The uncertainty of the  $Z^0/\gamma^*$  cross section at the LHC is of the order of 1% [59]. For the  $t\bar{t}$  background the scale and PDF uncertainty amount to 5.6% [60]. For the  $W^+W^-$  background, a PDF uncertainty of 6% is given in [52].

According to [11], the luminosity should be known within 3%. Since this affects signal and background in the same way, the effect on the signal significance will be negligible compared to the other uncertainties.

The second group of systematic errors will affect the signal significance in the real experiment, e.g. because they add additional uncertainty to the statistical uncertainty of the number of background events. Despite their different nature, their effect on the

expected signal significance is treated in the same way as the uncertainties of the first group of systematic errors, resulting in a rough estimate of how much the significance might decrease.

The uncertainty of the fit procedure was determined by varying the fit parameters of the combined fit according to their uncertainties. For the event counting method the uncertainty is found to be 0.08, the corresponding value for the Likelihood-Ratio method is 0.12.

The effect of the differences in the transverse momentum distributions of the leptons at low  $p_T$  for the converted  $Z^0/\gamma^* \rightarrow \ell^+\ell^-$  and the  $Z^0/\gamma^* \rightarrow \tau^+\tau^- \rightarrow \ell^+\ell^-$  sample (see Figure 6.15) was determined by downweighting events with low transverse momentum in the converted sample to get a good agreement of the two samples. By doing so, the signal significance increased by 0.06 for the event counting method and by 0.03 for the Likelihood-Ratio technique.

Table 6.12 summarises the main contributions to the systematic uncertainty of the signal significance.

Table 6.12: Summary of the main contributions to the systematic uncertainty of the signal significance for the event counting method ( $\Delta\sigma_{ec}$ ) and the Likelihood-Ratio technique ( $\Delta\sigma_{lh}$ ).

	$\Delta\sigma_{ec}$	$\Delta\sigma_{lh}$
$\cancel{E}_T$ scale	0.17	0.14
$b$ -tagging efficiency	0.08	0.10
$Z^0/\gamma^* \rightarrow \ell^+\ell^-$ conversion to $Z^0/\gamma^* \rightarrow \tau^+\tau^-$	0.06	0.03
Fit uncertainty	0.08	0.12
Signal cross section	0.35	0.32
$Z^0/\gamma^*$ cross section	0.07	0.02
$t\bar{t}/W^+W^-$ cross section	0.08	0.03
Total	0.42	0.39

## 6.9 Open Issues

For a successful analysis several points have to be further investigated. A critical point is the question, how much the signal significance will degrade due to the presence of pile-up events. For the design luminosity of  $2 \cdot 10^{33} \text{ cm}^{-2}\text{s}^{-1}$  on average 5 collisions are expected to take place in every bunch crossing. This additional activity in the detector will certainly degrade the  $\cancel{E}_T$  resolution and consequently broaden the  $Z^0$  and  $H$  peaks. On the other hand, the inclusion of the  $e + \mu$  and maybe the  $\ell + \text{Jet}$  trigger paths will increase the signal significance. Furthermore, better statistics of the samples used for the  $\cancel{E}_T$  calibration (the samples used correspond only to an integrated luminosity of about  $1 \text{ fb}^{-1}$ ), might result in an improved  $\cancel{E}_T$  resolution. Another question is how well PYTHIA simulates the different backgrounds. More specialised codes like TOPREX or ALPGEN should be used to cross-check the PYTHIA results. Finally it has to be shown that the extraction of the  $Z^0/\gamma^* \rightarrow \ell^+\ell^-$  control sample with the required purity is possible.

Let us hear the conclusion of the whole matter: Fear God, and keep his commandments: for this is the whole duty of man.

---

*Ecclesiastes 12, 13*

## Chapter 7

# Conclusions

The start-up of the [LHC](#) has been awaited for many years. It is hoped that its centre of mass energy, which is seven times higher than that of any previous collider, allows for the discovery of many new physical phenomena. One of the main physics goals is to understand the mechanism of the electroweak symmetry breaking. Within the [SM](#), the symmetry is broken by the vacuum expectation value of the Higgs field. If the Higgs mass is below 135 GeV, as preferred by the precision electroweak data, the discovery of the Higgs boson is very challenging. The strategies to find a light Higgs boson concentrate on the decay channels  $H \rightarrow \gamma\gamma$  and  $qqH \rightarrow \tau^+\tau^-$ .

In this work a complementary search strategy is presented, the study of the process  $H \rightarrow \tau^+\tau^- \rightarrow \ell^+\ell^-\cancel{E}_T$ . This ansatz tries to make use of the much higher cross section of the gluon fusion Higgs production. To suppress the irreducible background from  $Z^0/\gamma^* \rightarrow \tau^+\tau^-$  decays, an energetic balancing jet is required. The main observable to reduce the  $Z^0/\gamma^* \rightarrow \tau^+\tau^-$  background is the invariant mass of the reconstructed Higgs particle and the leading jet. The tau momenta are reconstructed with the help of the collinear approximation and the measurement of the missing transverse energy. The precision of the  $\cancel{E}_T$  measurement dominates the Higgs mass resolution and is therefore critical for the success of this analysis. To reduce the dependence on the detector simulation,  $Z^0/\gamma^* \rightarrow \ell^+\ell^-$  decays are used to extract a  $\cancel{E}_T$  calibration directly from the measured data. The  $Z^0/\gamma^* \rightarrow \ell^+\ell^-$  events are also used to determine the shape of the  $Z^0/\gamma^*$  background after all cuts. After all cuts, the significance of the observed signal is estimated by a fit procedure and a Likelihood-Ratio technique.

This analysis was developed to search for a [SM](#) Higgs boson. Nevertheless it is as

## 7. CONCLUSIONS

---

well applicable for the search for other particles decaying into a tau lepton pair, like the various [MSSM](#) Higgs bosons. For large values of  $\tan\beta$ , the total production cross sections of these particles might be significantly higher than that of the [SM](#) Higgs boson. Since the presented search strategy focuses on Higgs particles produced at large transverse momenta, it is important to keep in mind, that for large values of  $\tan\beta$  the transverse momentum spectrum can differ substantially from that of a [SM](#) Higgs boson [\[61\]](#).

In the hardware part, the various test and calibration algorithms for the CMS barrel pixel modules are presented. On one hand they are intended to test the correct hardware functionality, on the other hand to extract the calibration parameters necessary to successfully operate the pixel detector. The algorithms have been implemented in a test suite, which was used to qualify all the pixel barrel modules. Based on the test results, the best modules were chosen to be used for the final detector. Besides this, the algorithms were used by the forward pixel collaboration to test their plaquettes [\[62\]](#) and have been implemented in the data taking framework of CMS, to be used for the testing and calibration of the detector in the following years.

# Appendix A

Table A.1: Meaning of the symbols used in the following figures.

$x_i$	Lepton momentum fraction $ \vec{p}_{\ell,i} / \vec{p}_{\tau,i} , i = 1, 2$
$\cancel{E}_T$	Missing transverse energy
$\cancel{E}_T/\sqrt{\Sigma E_T}$	Significance of the missing transverse energy
$m_{\ell\ell}$	Invariant mass of the lepton pair
$\#b\text{-jets}$	Number of $b$ -tagged jets
$p_{T,\ell 2}$	Transverse momentum of the subleading lepton
$\Delta\phi_{\ell\ell}$	Difference in $\phi$ between the two leptons
$\Delta\eta_{\ell\ell}$	Difference in $\eta$ between the two leptons
$p_{T,H}$	Transverse momentum of the reconstructed Higgs boson
$E_{T,LJ}$	Transverse energy of the reconstructed Higgs boson
$\eta_{LJ}$	Pseudorapidity of the leading jet
$m_{H,LJ}$	Invariant mass of the Higgs boson and the leading jet
$\# \text{ central high-}E_T$	Number of central ( $ \eta  < 1.6$ ) jets with $E_T > 30 \text{ GeV}$



## A.1 Cut Variable Distributions

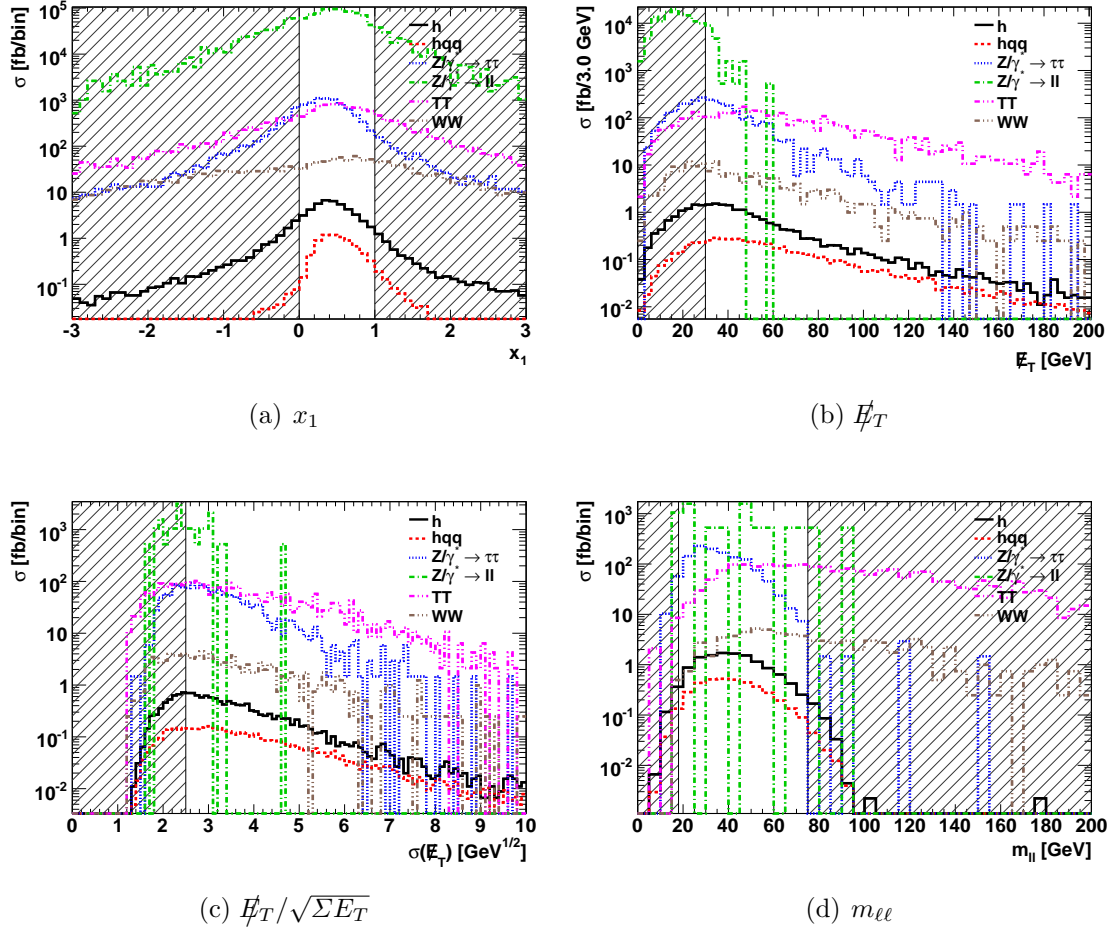


Figure A.1: Distributions of the cut variables before the application of the corresponding cuts. The events in the right-hatched regions are rejected.

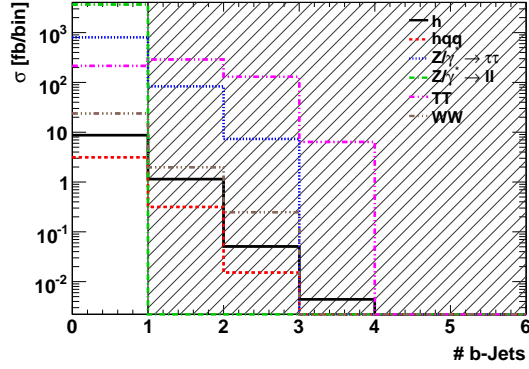
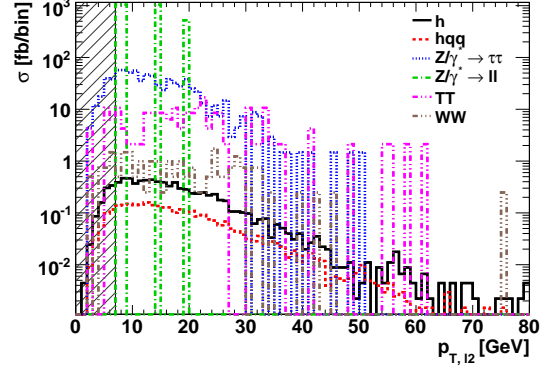
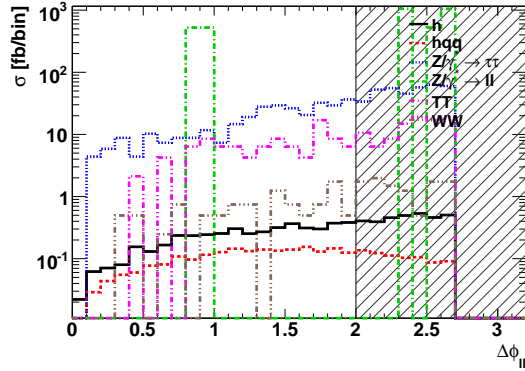
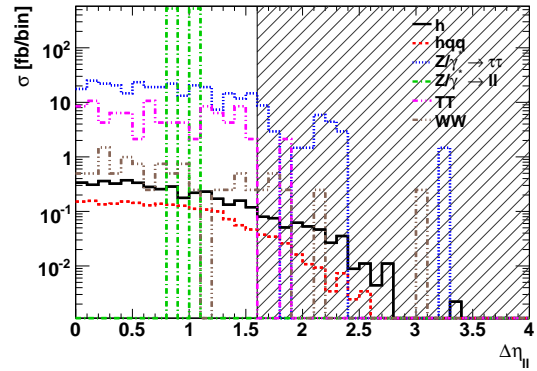
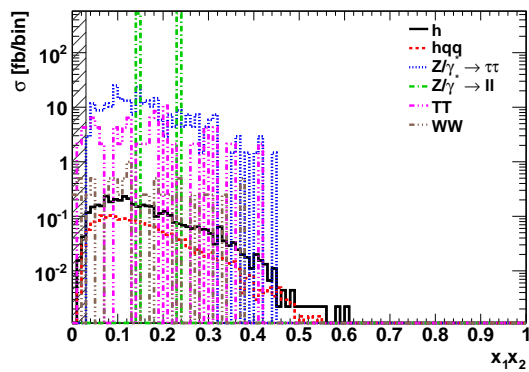
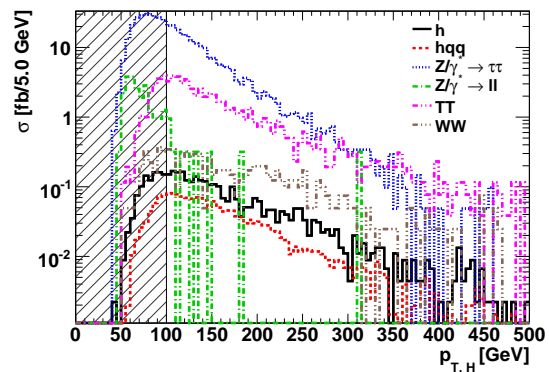
(a)  $\#b\text{-jets}$ (b)  $p_{T, \ell 2}$ (c)  $\Delta\phi_{\ell\ell}$ (d)  $\Delta\eta_{\ell\ell}$ (e)  $x_1 x_2$ (f)  $p_{T, H}$ 

Figure A.2: Distributions of the cut variables before the application of the corresponding cuts (continued). The events in the right-hatched regions are rejected.

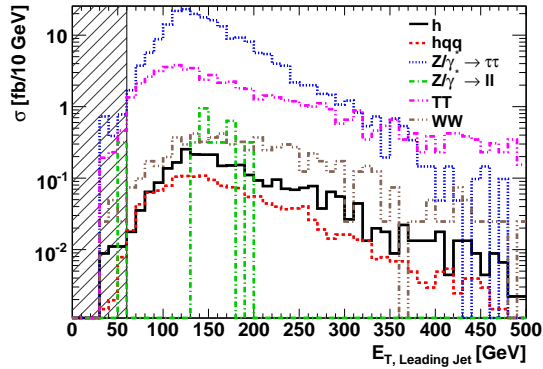
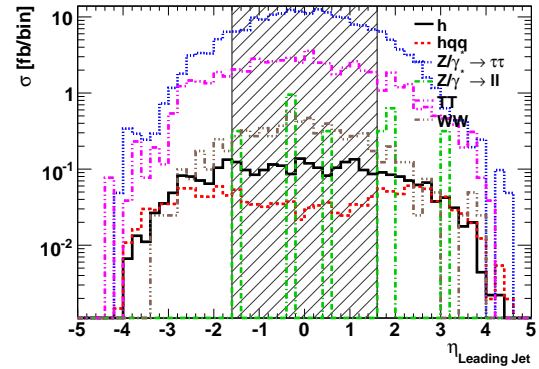
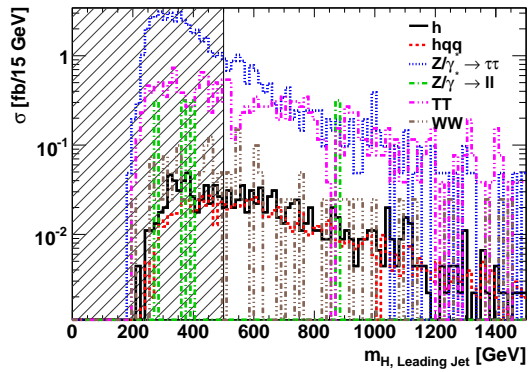
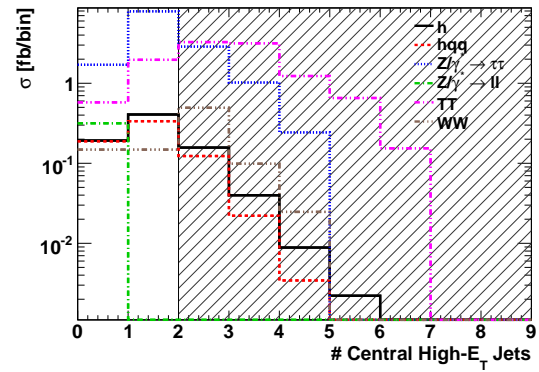
(a)  $E_{T,LJ}$ (b)  $\eta_{LJ}$ (c)  $m_{H,LJ}$ (d) # central high- $E_T$  jets

Figure A.3: Distributions of the cut variables before the application of the corresponding cuts (continued). The events in the right-hatched regions are rejected.

## A.2 Cut Optimisation

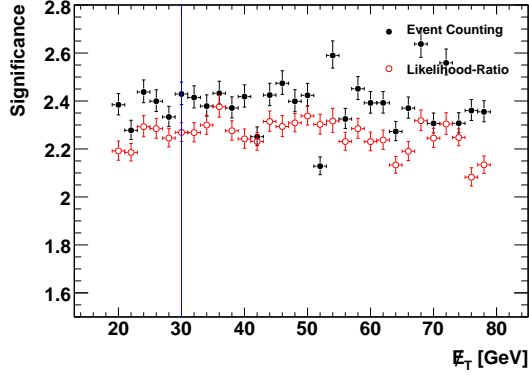
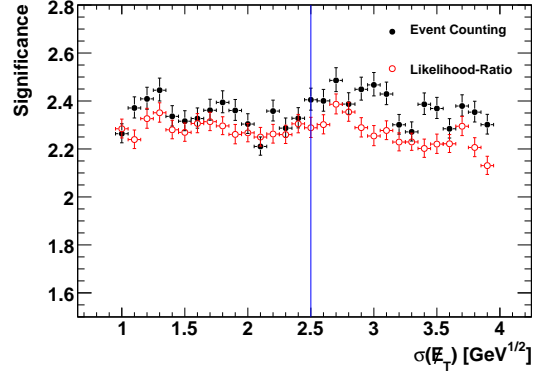
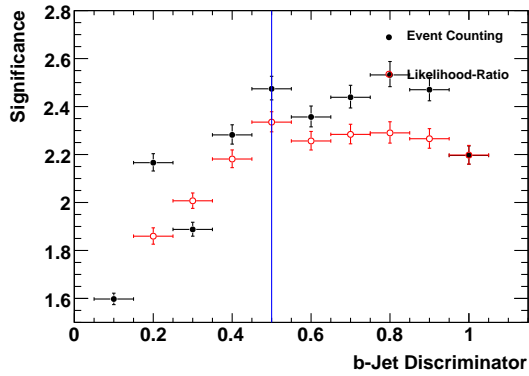
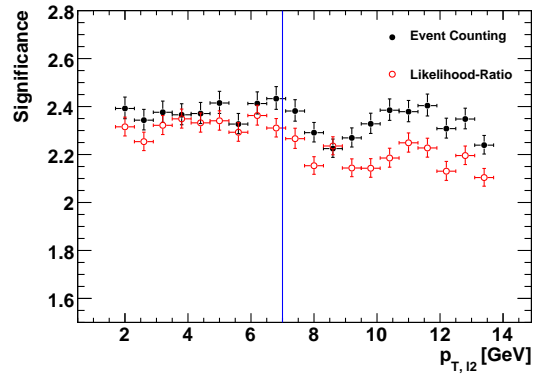
(a)  $\cancel{E}_T > 30 \text{ GeV}$ (b)  $\cancel{E}_T / \sqrt{\Sigma E_T} > 2.5 \sqrt{\text{GeV}}$ (c)  $b$ -jet discriminator(d)  $p_{T,\ell 2} < 7 \text{ GeV}$ 

Figure A.4: Optimisation of the different cuts applied. The error bars show the statistical uncertainty due to the limited number of toy-experiments.

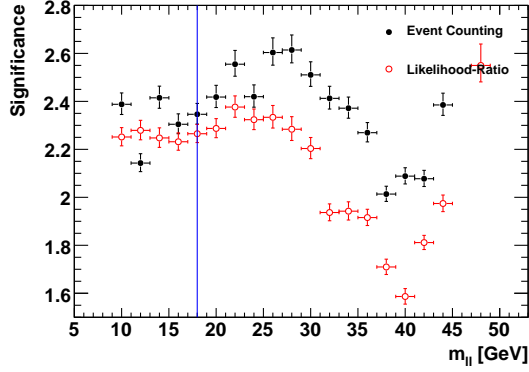
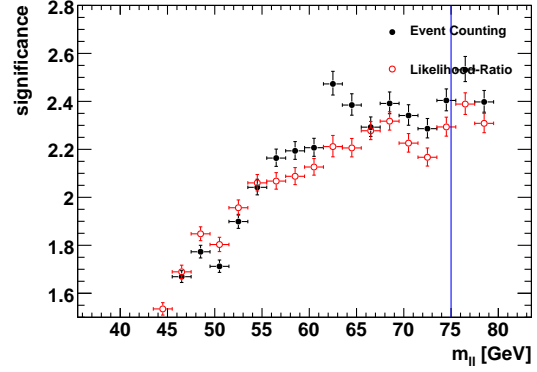
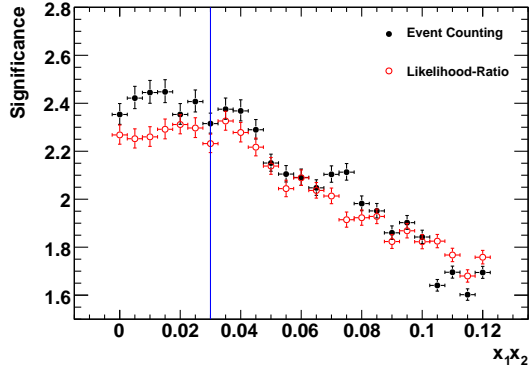
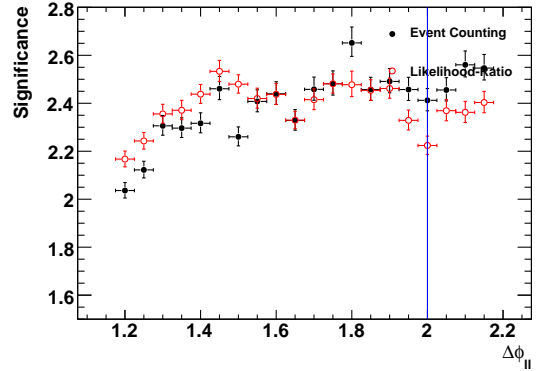
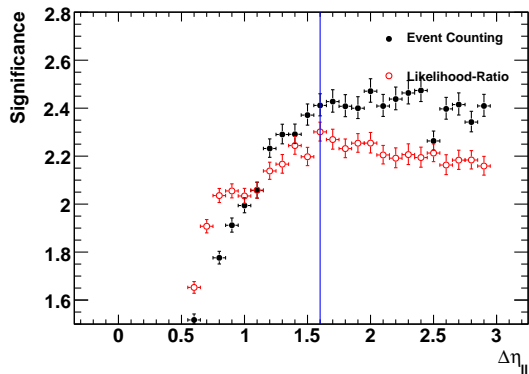
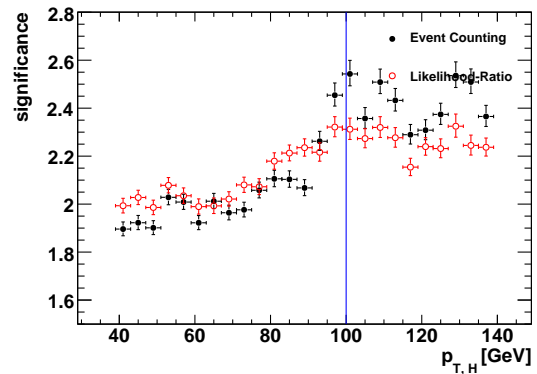

(a)  $m_{\ell\ell} > 18 \text{ GeV}$ 

(b)  $m_{\ell\ell} < 75 \text{ GeV}$ 

(c)  $x_1 x_2 > 0.03$ 

(d)  $\Delta\phi_{\ell\ell} < 2.0$ 

(e)  $\Delta\eta_{\ell\ell} < 1.6$ 

(f)  $p_{T,H} > 100 \text{ GeV}$ 

Figure A.5: Optimisation of the different cuts applied. The error bars show the statistical uncertainty due to the limited number of toy-experiments.

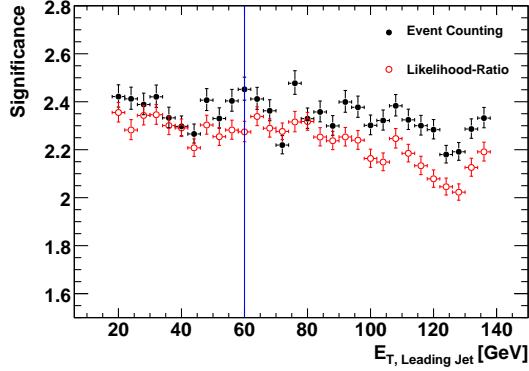
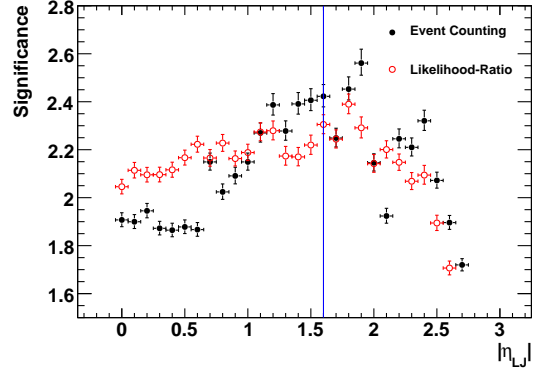
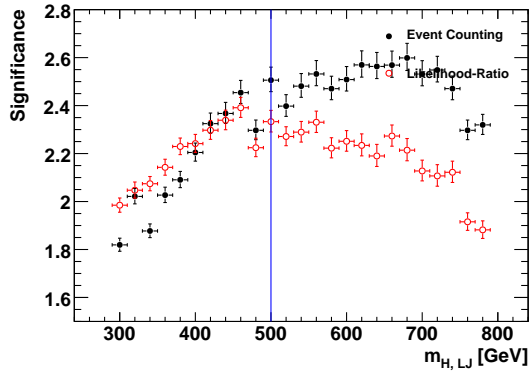
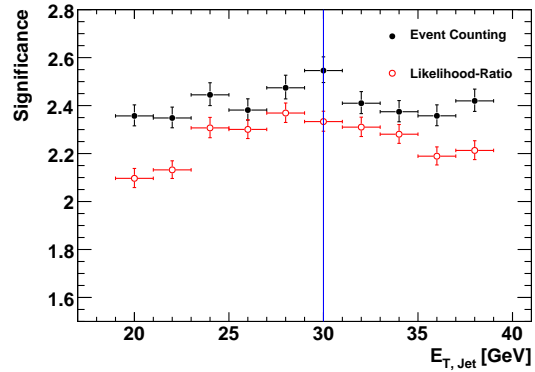
(a)  $E_{T,LJ} > 60$  GeV(b)  $|\eta_{LJ}| > 1.6$ (c)  $m_{H,LJ} > 500$  GeV(d)  $E_T$  threshold for the number of central high- $E_T$  jets

Figure A.6: Optimisation of the different cuts applied. The error bars show the statistical uncertainty due to the limited number of toy-experiments.

# List of Acronyms

<b>Notation</b>	<b>Description</b>
<b>ADC</b>	Analogue to Digital Converter, 22, 27, 31, 43–45
<b>CERN</b>	Conseil Européen pour la Recherche Nucléaire, 3, 4
<b>CMS</b>	Compact Muon Solenoid, 1–6, 8, 9, 12, 13, 16, 41, 49, 60, 65, 68
<b>CMSSW</b>	CMS software framework, 61–63
<b>DAC</b>	Digital to Analogue Converter, 17, 18, 23–27, 29, 33, 34, 36, 38–41, 43–46, 48
<b>ECAL</b>	Electromagnetic Calorimeter, 7, 63
<b>FEC</b>	Front End Controller, 40
<b>FED</b>	Front End Driver, 40
<b>FPGA</b>	Field-Programmable Gate Array, 22, 24
<b>HCAL</b>	Hadronic Calorimeter, 7
<b>HDI</b>	High Density Interconnect, 14–16, 26, 34
<b>HLT</b>	High Level Trigger, 9, 72, 74, 75, 80
<b>LEP</b>	Large Electron-Positron Collider, 1, 55
<b>LHC</b>	Large Hadron Collider, 1–3, 6, 17, 55, 94

---

<b>Notation</b>	<b>Description</b>
<b>MC</b>	Monte-Carlo, 61, 64, 69, 81
<b>MSSM</b>	Minimal Supersymmetric Standard Model, 57, 60, 94
<b>NDF</b>	Number of Degrees of Freedom, 73, 74, 82
<b>NLO</b>	Next-To-Leading Order, 55, 61
<b>PSI</b>	Paul Scherrer Institute, 1
<b>PUC</b>	Pixel Unit Cell, 14, 17, 19, 21, 26, 27, 33
<b>RMS</b>	Root Mean Square, 31, 42, 45, 72, 77
<b>ROC</b>	Readout Chip, 14–18, 21, 23–27, 29, 31, 32, 34–36, 38–46, 48, 49
<b>SM</b>	Standard Model, 1, 3, 54, 60, 85, 87, 94
<b>TBM</b>	Token Bit Manager, 14, 16, 17, 25, 26
<b>TeV</b>	Tera Electron Volt, 3
<b>UBL</b>	Ultra Black Level, 17, 44
<b>UML</b>	Unified Modelling Language, 22
<b>VBF</b>	Vector Boson Fusion, 55, 60, 91



# Bibliography

- [1] ALEPH Collaboration, P. Bock *et al.*, *Lower bound for the standard model Higgs boson mass from combining the results of the four LEP experiments*, *CERN-EP-98-046* (1998). [1](#)
- [2] ALEPH Collaboration, A. Heister *et al.*, *Final results of the searches for neutral Higgs bosons in  $e^+e^-$  collisions at  $s^{1/2}$  up to 209-GeV*, *Phys. Lett.* B526 (2002) 191–205, [[hep-ex/0201014](#)]. [1](#)
- [3] LEP Working Group for Higgs boson searches Collaboration, R. Barate *et al.*, *Search for the standard model higgs boson at LEP*, *Phys. Lett.* B565 (2003) 61–75, [[hep-ex/0306033](#)]. [1](#), [55](#), [87](#)
- [4] Tevatron New Phenomena Higgs Working Group Collaboration, G. Bernardi *et al.*, *Combined CDF and Dzero Upper Limits on Standard Model Higgs Boson Production at High Mass (155-200 GeV/c<sup>2</sup>) with 3 fb<sup>-1</sup> of data*, [0808.0534](#). [1](#)
- [5] R. I. Dzhelyadin *et al.*, *Search for rare decays of  $\eta$  and  $\eta'$  mesons and for light higgs particles*, *Phys. Lett.* B105 (1981) 239. [1](#)
- [6] E. . Bruning, O. *et al.*, *LHC design report. Vol. I: The LHC main ring*, *CERN-2004-003-V-1*. [3](#)
- [7] *ATLAS: Detector and physics performance technical design report. Volume 1*, *CERN-LHCC-99-14*. [3](#)
- [8] *CMS, the Compact Muon Solenoid: Technical proposal*, *CERN-LHCC-94-38*. [3](#)
- [9] LHCb Collaboration, S. Amato *et al.*, *LHCb technical proposal*, *CERN-LHCC-98-04*. [3](#)

- [10] *ALICE: Technical proposal for a large ion collider experiment at the CERN LHC*, CERN-LHCC-95-71. 3
- [11] CMS Collaboration, *CMS technical design report, volume I: Detector performance and software*, CERN-LHCC-2006-001 (2006). 4, 7, 8, 9, 62, 63, 74, 90, 91
- [12] C. Broennimann *et al.*, *Development of an indium bump bond process for silicon pixel detectors at PSI*, *Nucl. Instrum. Meth.* A565 (2006) 303–308, [[physics/0510021](#)]. 14, 32
- [13] Y. Allkofer *et al.*, *Design and performance of the silicon sensors for the CMS barrel pixel detector*, *Nucl. Instrum. Meth.* A584 (2008) 25–41, [[physics/0702092](#)]. 16
- [14] E. Bartz, *The 0.25- $\mu\text{m}$  token bit manager chip for the CMS pixel readout*, Prepared for 11th Workshop on Electronics for LHC and Future Experiments (LECC 2005), Heidelberg, Germany, 12-16 September 2005 (2005). 17
- [15] H. C. Kastli *et al.*, *Design and performance of the CMS pixel detector readout chip*, *Nucl. Instrum. Meth.* A565 (2006) 188–194, [[physics/0511166](#)]. 17
- [16] S. Dambach, *CMS pixel module optimization and B meson lifetime measurements, doctoral thesis* (2009). 18, 19, 26, 42
- [17] C. Eggel, *CMS pixel module qualification and search for  $B_s^0 \rightarrow \mu^+ \mu^-$* , doctoral thesis (2009). 22, 50
- [18] *ROOT: an object oriented data analysis framework*, <http://root.cern.ch/>. 22
- [19] K. Gabathuler, *PSI46 pixel chip - external specification, internal document of the CMS Barrel Pixel collaboration* (2004). 26, 43
- [20] A. Starodumov *et al.*, *Qualification procedures of the CMS pixel barrel modules*, *Nucl. Instrum. Meth.* A565 (2006) 67–72, [[physics/0510165](#)]. 32
- [21] L. Rossi, P. Fischer, T. Rohe, and N. Wermes, *Pixel detectors: From fundamentals to applications*, . Berlin, Germany: Springer (2006) 304 p. 35

- [22] M. Waser, *Trimming of the CMS Pixel Detector Modules, term paper* (2007). [41](#)
- [23] W. Erdmann *et al.*, *LHC-rate beam test of CMS pixel barrel modules*, *Nucl. Instrum. Meth. A*572 (2007) 57–58. [45](#)
- [24] H. Bichsel, *Stragglings in thin silicon detectors*, *Rev. Mod. Phys.* 60 (1988) 663–699. [45](#)
- [25] P. W. Higgs, *Broken symmetries, massless particles and gauge fields*, *Phys. Lett.* 12 (1964) 132–133. [54](#)
- [26] P. W. Higgs, *Broken symmetries and the masses of gauge bosons*, *Phys. Rev. Lett.* 13 (1964) 508–509. [54](#)
- [27] P. W. Higgs, *Spontaneous symmetry breakdown without massless bosons*, *Phys. Rev.* 145 (1966) 1156–1163. [54](#)
- [28] F. Englert and R. Brout, *Broken symmetry and the mass of gauge vector mesons*, *Phys. Rev. Lett.* 13 (1964) 321–322. [54](#)
- [29] G. S. Guralnik, C. R. Hagen, and T. W. B. Kibble, *Global conservation laws and massless particles*, *Phys. Rev. Lett.* 13 (1964) 585–587. [54](#)
- [30] LEP Electroweak Working Group Collaboration, J. Alcaraz *et al.*, *A combination of preliminary electroweak measurements and constraints on the standard model*, [hep-ex/0612034](#). [55](#)
- [31] A. Djouadi, *The anatomy of electro-weak symmetry breaking. I: The Higgs boson in the standard model*, *Phys. Rept.* 457 (2008) 1–216, [[hep-ph/0503172](#)]. [55](#), [91](#)
- [32] T. Schucker, *Higgs-mass predictions*, [arXiv:0708.3344](#). [55](#)
- [33] D. L. Rainwater, D. Zeppenfeld, and K. Hagiwara, *Searching for  $h \rightarrow \tau\tau$  in weak boson fusion at the LHC*, *Phys. Rev. D*59 (1999) 014037, [[hep-ph/9808468](#)]. [55](#)
- [34] M. Spira, *QCD effects in higgs physics*, *Fortsch. Phys.* 46 (1998) 203–284, [[hep-ph/9705337](#)]. [56](#), [59](#)

- [35] M. Spira, *HIGLU: A program for the calculation of the total higgs production cross section at hadron colliders via gluon fusion including QCD corrections*, [hep-ph/9510347](#). 57
- [36] T. Han, G. Valencia, and S. Willenbrock, *Structure function approach to vector boson scattering in pp collisions*, *Phys. Rev. Lett.* 69 (1992) 3274–3277, [[hep-ph/9206246](#)]. 57
- [37] A. Djouadi, J. Kalinowski, and M. Spira, *HDECAY: A program for higgs boson decays in the standard model and its supersymmetric extension*, *Comput. Phys. Commun.* 108 (1998) 56–74, [[hep-ph/9704448](#)]. 57
- [38] CMS Collaboration, *CMS technical design report, volume II: Physics performance*, *J. Phys.* G34 (2007) 995–1579. 58, 89
- [39] J. Wess and B. Zumino, *Supergauge transformations in four-dimensions*, *Nucl. Phys.* B70 (1974) 39–50. 57
- [40] E. Witten, *Mass hierarchies in supersymmetric theories*, *Phys. Lett.* B105 (1981) 267. 58
- [41] Y. Okada, M. Yamaguchi, and T. Yanagida, *Upper bound of the lightest higgs boson mass in the minimal supersymmetric standard model*, *Prog. Theor. Phys.* 85 (1991) 1–6. 58
- [42] U. Berzano and A. Nikitenko, *Standard model higgs boson search via  $h \rightarrow \tau\tau \rightarrow e\mu$  channel*, *CERN-CMS-NOTE-2006-082* (2006). 60
- [43] C. Foudas, A. Nikitenko, and M. Takahashi, *Observation of the standard model higgs boson via  $h \rightarrow \tau\tau \rightarrow \text{lepton} + \text{jet}$  channel*, *CMS AN 2006/038* (2006). 60
- [44] S. Gennai, A. Nikitenko, and L. Wendland, *Search for MSSM heavy neutral higgs boson in  $\tau\tau \rightarrow \text{two jet}$  decay mode*, *CMS AN 2006/048* (2006). 60
- [45] R. K. Ellis, I. Hinchliffe, M. Soldate, and J. J. van der Bij, *Higgs decay to  $\tau^+\tau^-$ : A possible signature of intermediate mass higgs bosons at the SSC*, *Nucl. Phys.* B297 (1988) 221. 60, 66

- [46] B. Mellado, W. Quayle, and S. L. Wu, *Prospects for the observation of a higgs boson with  $h \rightarrow \tau^+\tau^- \rightarrow \ell^+\ell^- \cancel{E}_T$  associated with one jet at the LHC*, *Phys. Lett. B* 611 (2005) 60–65, [[hep-ph/0406095](#)]. 60
- [47] T. Sjostrand, L. Lonnblad, and S. Mrenna, *PYTHIA 6.2: Physics and manual*, [hep-ph/0108264](#). 60
- [48] R. Hamberg, W. L. van Neerven, and T. Matsuura, *A complete calculation of the order  $\alpha_s^2$  correction to the Drell-Yan K factor*, *Nucl. Phys. B* 359 (1991) 343–405. 61
- [49] A. D. Martin, R. G. Roberts, W. J. Stirling, and R. S. Thorne, *Parton distributions and the LHC: W and Z production*, *Eur. Phys. J. C* 14 (2000) 133–145, [[hep-ph/9907231](#)]. 61
- [50] P. Nason, S. Dawson, and R. K. Ellis, *The total cross-section for the production of heavy quarks in hadronic collisions*, *Nucl. Phys. B* 303 (1988) 607. 61
- [51] N. Kidonakis and R. Vogt, *Next-to-next-to-leading order soft-gluon corrections in top quark hadroproduction*, *Phys. Rev. D* 68 (2003) 114014, [[hep-ph/0308222](#)]. 61
- [52] J. M. Campbell and R. K. Ellis, *An update on vector boson pair production at hadron colliders*, *Phys. Rev. D* 60 (1999) 113006, [[hep-ph/9905386](#)]. 61, 91
- [53] T. Sjostrand, S. Mrenna, and P. Skands, *PYTHIA 6.4 physics and manual*, *JHEP* 05 (2006) 026, [[hep-ph/0603175](#)]. 61
- [54] GEANT4 Collaboration, S. Agostinelli *et al.*, *GEANT4: A simulation toolkit*, *Nucl. Instrum. Meth. A* 506 (2003) 250–303. 62
- [55] S. Baffioni *et al.*, *Electron reconstruction in CMS*, *Eur. Phys. J. C* 49 (2007) 1099–1116. 63
- [56] A. Heister *et al.*, *Measurement of jets with the CMS detector at the LHC*, *CERN-CMS-NOTE-2006-036* (2006). 64
- [57] A. Rizzi, F. Palla, and G. Segneri, *Track impact parameter based b-tagging with CMS*, *CERN-CMS-NOTE-2006-019* (2006). 65

- 
- [58] S. Esen *et al.*,  $E_T$  performance in CMS, *CMS AN 2007/041* (2007). 69
- [59] S. Haywood *et al.*, *Electroweak physics*, [hep-ph/0003275](#). 91
- [60] D. Chakraborty, J. Konigsberg, and D. L. Rainwater, *Review of top quark physics*, *Ann. Rev. Nucl. Part. Sci.* 53 (2003) 301–351, [[hep-ph/0303092](#)]. 91
- [61] U. Langenegger, M. Spira, A. Starodumov, and P. Trueb, *SM and MSSM Higgs boson production: Spectra at large transverse momentum*, *JHEP* 06 (2006) 035, [[hep-ph/0604156](#)]. 95
- [62] D. Menasce, M. Turqueti, and L. Uplegger, *The Renaissance: A test-stand for the Forward CMS Pixel Tracker assembly*, *Nucl. Instrum. Meth.* A579 (2007) 1141–1149. 95

## Acknowledgements

First of all, I would like to thank Urs Langenegger for supervising and guiding this thesis. The regular discussions with him helped to deepen the substance of this work and provided many ideas to the hardware as well as to the analysis part of this work.

Felicitas Pauss, who supported already my diploma thesis, readily accepted to co-examine this work.

I owe a big thanks to Andrey Starodumov with whom I spent many hours of common work in the laboratory. With a lot of helpfulness and interest he always assisted this work during the four years. Together with the graduate students of our group, he contributed a lot to the work of the module testing.

I would also like to thank Roland Horisberger and his group for their friendly reception into the barrel pixel collaboration. I profited a lot from their explanations about the detector system and their help for the module qualification. Especially Beat Meier, who designed the electronics test-board and implemented the software to use it, was a big help.

Derek Feichtinger was a valuable help for any kind of problems with the LHC Grid.

Finally, I would like to thank my family, which provided me with the necessary support and environment, which made this work possible.

# Curriculum Vitae

## Personal Data

Name Peter Trüb  
Date of Birth July 23, 1979  
Place of Birth Schlieren (ZH)  
Nationality Swiss, from Zurich

## Education

1986 – 1991 Primary School in Gontenschwil  
1991 – 1995 Bezirksschule in Unterkulm  
1995 – 1999 Alte Kantonsschule in Aarau  
1999 Kantonale Matura, Typus C  
1999 – 2004 Study of physics at the Swiss Federal Institute  
of Technology, Zurich (ETHZ)  
2004 Diploma thesis at the Institute for Theoretical Physics  
at the University of Zurich: “Dark matter detection”  
Diploma in Theoretical Physics at ETHZ  
2005 Didactical Certificate at ETHZ in physics  
2004 – 2008 Graduate education in Experimental High Energy Physics  
at ETHZ and the Paul Scherrer Institute (PSI)



## Publications

1. **“CMS Barrel Pixel Module Qualification”**, S. Dambach *et al.*, (in preparation).
2. **“Standard Model Higgs Boson Search in the Decay  $H \rightarrow \tau^+\tau^- \rightarrow \ell^+\ell^-\cancel{E}_T$ ”**, U. Langenegger *et al.*, CMS AN-2008/053 (2008).
3. **“Search for the Standard Model Higgs Boson produced in Vector Boson Fusion and decaying into  $\tau\tau$  pair in CMS with  $1\text{ fb}^{-1}$ ”**, M. Vázquez Acosta *et al.*, CMS AN-2007/035 (2008).
4. **“CMS High Level Trigger”**, CMS Collaboration, CERN/LHCC 2007-021 (2007).
5. **“CMS Technical Design Report, Volume II: Physics Performance”**, G. L. Bayatian *et al.* [CMS Collaboration], J. Phys. G **34**, 995 (2007).
6. **“LHC-rate Beam Test of CMS Pixel Barrel Modules”**, W. Erdmann *et al.*, Nucl. Instrum. Meth. A **572**, 57 (2007).
7. **“CMS Physics Technical Design Report: Addendum on High Density QCD with Heavy Ions”**, D. G. d’Enterria *et al.* [CMS Collaboration], J. Phys. G **34**, 2307 (2007).
8. **“Test and Qualification Procedures of the CMS Pixel Barrel Modules”**, U. Langenegger *et al.*, CMS IN-2006/006 (2006).
9. **“CMS physics: Technical Design Report”**, G. L. Bayatian *et al.* [CMS Collaboration], CERN-LHCC-2006-001 (2006).
10. **“Qualification Procedures of the CMS Pixel Barrel Modules”**, A. Starodumov *et al.*, Nucl. Instrum. Meth. A **565**, 67 (2006) [arXiv:physics/0510165].
11. **“Dark Matter Detection”**, P. Trüb, Diploma Thesis (2004).

## Selected Talks

1. “ $\cancel{E}_T$  Calibration from  $Z^0 \rightarrow \ell^+\ell^-$  Events”, MET Working Group Meeting, CERN, August 2008.
2. “Standard Model Higgs Boson Search in the Decay  $H \rightarrow \tau^+\tau^- \rightarrow \ell^+\ell^-$ ”, Higgs Working Group Meeting, CERN, August 2008.
3. “Pixels Electronics Gain Calibration”, Joint Tracker - Physics Workshop, CERN, March 2008.
4. “Parametric Trimming”, General Pixel Meeting, CERN, July 2007.
5. “The Muon+Tau High Level Trigger”, Electroweak Meeting, CERN, June 2007.
6. “SM and MSSM Higgs Boson Production: Spectra at Large Transverse Momentum”, SPS Annual Meeting, UNIZH, February 2007.
7. “FPGA Processor Based Barrel Module Tests”, General Pixel Meeting, CERN, March 2006.
8. “Qualification Procedures of the CMS Pixel Barrel Modules”, SPS Annual Meeting, EPFL, February 2006.
9. “CMS Pixel Barrel Module Tests and Characterization”, Pixel Software Workshop, FNAL, October 2005.
10. “Generator Level Study of the Higgs Channel  $gg \rightarrow H \rightarrow b\bar{b}$ ”, Pixel Group Meeting, PSI, June 2005.
11. “Bump Bonding Test Procedures”, Pixel General Meeting, CERN, April 2005.
12. “Pixel Classes”, Pixel Software Meeting, CERN, March 2005.